

---

# **Electronic structure of selected aromatic hydrocarbon systems investigated with electron energy-loss spectroscopy**

Dissertation

zur Erlangung des akademischen Grades  
Doctor rerum naturalium  
(Dr. rer. nat.)

vorgelegt von

Dipl.-Phys. Friedrich Roth  
geboren am 26.01.1985 in Dresden

Institut für Festkörperphysik  
Fachrichtung Physik  
Fakultät für Mathematik und Naturwissenschaften  
der Technischen Universität Dresden  
2012

*“Der Fortgang der wissenschaftlichen Entwicklung ist im Endeffekt eine ständige Flucht vor dem Staunen.”*

Albert Einstein

1. Gutachter: Prof. Dr. Bernd Büchner
2. Gutachter: Prof. Dr. Martin Knupfer

Eingereicht am 19.09.2012

Verteidigt am 22.02.2013

# Contents

<b>List of Figures</b>	<b>6</b>
<b>1. Introduction And Motivation</b>	<b>7</b>
<b>2. Electron Energy-Loss Spectroscopy</b>	<b>11</b>
2.1. Introduction . . . . .	11
2.2. Working Principle . . . . .	12
2.2.1. Possible EELS Excitations . . . . .	13
2.2.2. Scattering Theory - The EELS Cross Section . . . . .	15
2.3. The Dielectric Function . . . . .	17
2.3.1. The Drude-Lorentz-Model . . . . .	23
2.4. Experimental Details . . . . .	27
2.4.1. The Spectrometer . . . . .	27
2.4.2. Sample Preparation . . . . .	28
<b>3. Polycyclic Aromatic Hydrocarbon Systems And Their Properties</b>	<b>33</b>
3.1. Introduction . . . . .	33
3.2. Features Of Aromatic Hydrocarbon Molecules . . . . .	35
3.2.1. Crystal Structure Of Nonpolar Molecules . . . . .	37
3.2.2. Electronic Properties: Optical Absorption And Excitons . . . . .	40
3.3. Superconductivity In Carbon-Based Materials . . . . .	41
3.3.1. A Short Overview . . . . .	41
3.3.2. The "New" Class Of Hydrocarbon Superconductors . . . . .	43
<b>4. Results Part I: EELS On Pristine Aromatic Hydrocarbon Systems</b>	<b>49</b>
4.1. Beam Damage Effects . . . . .	49
4.2. Electronic Properties Of Pristine Picene Thin Films . . . . .	51
4.2.1. Kramers-Kronig Analysis Of Undoped Picene . . . . .	56
4.2.2. Exciton Character In Picene Molecular Solids . . . . .	57
4.3. Electronic Properties Of Pristine Coronene Thin Films . . . . .	61
4.4. Comparison Between The Electronic Structure Of Selected Acenes And Phenacene . . . . .	64
4.5. Electronic Properties Of Pristine 1,2:8,9-dibenzopentacene . . . . .	69
<b>5. Results Part II: EELS On Potassium Doped Aromatic Hydrocarbon Systems</b>	<b>75</b>
5.1. Evidence For Phase Formation In K Intercalated 1,2;8,9-dibenzopentacene . . . . .	75
5.2. Electronic Structure Of Potassium Doped Picene . . . . .	80
5.3. Electronic Structure Of Potassium Doped Coronene . . . . .	89
5.4. Further Candidates For Hydrocarbon Superconductors . . . . .	92

<b>6. Summary And Outlook</b>	<b>97</b>
<b>A. Relativistic Calculation Of The Incoming Wave Vector</b>	<b>101</b>
<b>B. Structure And Aromaticity</b>	<b>103</b>
<b>C. Additional Information About Experimental And Theoretical Methods</b>	<b>107</b>
C.1. Photoemission . . . . .	107
C.2. Theory . . . . .	108
<b>Bibliography</b>	<b>109</b>
<b>List Of Publications</b>	<b>121</b>
<b>List Of Talks And Posters</b>	<b>123</b>
<b>Acknowledgements</b>	<b>125</b>

# List of Figures

2.1. EELS scattering geometry . . . . .	12
2.2. Possible EELS excitations . . . . .	14
2.3. Momentum transfer in the <i>ab</i> -plane of the sample . . . . .	14
2.4. Plasmon and single-particle excitation continuum . . . . .	20
2.5. The dielectric function in the Drude-Lorentz-model . . . . .	25
2.6. Schematic drawing of the electron energy-loss spectrometer . . . . .	27
2.7. The characteristics of the electron beam . . . . .	28
(a). Energy resolution . . . . .	28
(b). Momentum resolution . . . . .	28
2.8. Pentacene and tetracene single crystals . . . . .	29
2.9. Thermal evaporation unit . . . . .	30
2.10. Simplified view of the preparation process . . . . .	30
2.11. The EELS samples and their dimension . . . . .	31
(a). EELS sample on a TEM grid . . . . .	31
(b). Dimension of the samples under investigation . . . . .	31
2.12. Schematic drawing of the doping procedure . . . . .	31
3.1. Energy diagram of a double bond between two carbon atoms . . . . .	34
3.2. Various representations of the benzene molecule . . . . .	35
3.3. The Lennard-Jones potential . . . . .	37
3.4. The herringbone structure . . . . .	39
3.5. Transport Gap <i>vs.</i> Optical Gap / Onset energy in optical absorption of phenacenes and acenes . . . . .	41
3.6. Carbon network materials . . . . .	42
3.7. Physical appearance and crystal structure of doped picene . . . . .	44
3.8. Temperature dependence of the magnetization of $K_{3,3}$ picene . . . . .	45
3.9. Electronic structure of Buckminsterfullerene and Picene . . . . .	47
4.1. Beam damage effects of the Bragg spectrum and the loss function . . . . .	50
4.2. Aging of the loss function of chrysene at different temperatures . . . . .	51
4.3. Bragg spectra of solid picene for the two different orientated films . . . . .	52
4.4. Photoemission profil and C 1s core level spectra of undoped picene . . . . .	53
4.5. Loss function of solid picene . . . . .	54
4.6. Loss function spectra of picene single crystal . . . . .	55
4.7. Electron diffraction profiles of solid picene thin films . . . . .	57
4.8. Types of excitons . . . . .	58
4.9. Momentum dependence of the EELS spectra of solid picene . . . . .	59
4.10. Momentum dependence of the spectral weight of excitonic excitations . . . . .	61
4.11. C 1s core-level excitations of pristine coronene . . . . .	62

4.12. Loss function and Bragg spectra of pristine coronene . . . . .	63
4.13. Loss function of chrysene, tetracene, picene, and pentacene . . . . .	65
4.14. Exciton structure of tetracene and pentacene . . . . .	66
4.15. Momentum dependence of the EELS spectra of chrysene and picene . . . . .	67
4.16. Momentum dependence of the EELS spectra of tetracene and pentacene . . . . .	68
4.17. PES and EELS profiles of 1,2;8,9-dibenzopentacene and pentacene . . . . .	70
4.18. Orbital energies of pentacene and 1,2;8,9-dibenzopentacene . . . . .	71
5.1. C 1s and K 2p core level excitations of K doped 1,2;8,9-dibenzopentacene . . . . .	76
5.2. Evolution of the loss function upon K doping in 1,2;8,9-dibenzopentacene . . . . .	77
5.3. Phase diagram of $K_x(1,2;8,9\text{-dibenzopentacene})$ for $x$ up to 3 . . . . .	79
5.4. Bragg spectra and C 1s and K 2p core level excitations of K doped picene . . . . .	81
5.5. Comparison of the loss function of undoped und K doped picene . . . . .	82
5.6. Loss function, real and imaginary part of $\epsilon$ of K doped picene . . . . .	83
5.7. Optical conductivity of K doped picene . . . . .	85
5.8. Plasmon dispersion of K doped picene . . . . .	86
5.9. Calculated loss function of $K_3$ picene . . . . .	88
5.10. Absorption edge and loss function of K doped coronene . . . . .	89
5.11. Loss function, real and imaginary part of $\epsilon$ of K doped coronene . . . . .	90
5.12. Optical conductivity of K doped coronene . . . . .	91
5.13. C 1s and K 2p core level excitations of undoped and K doped chrysene . . . . .	93
5.14. Variation of the loss function upon doping and optical conductivity of chrysene . . . . .	94
5.15. Plasmon dispersion of K intercalated chrysene . . . . .	96
6.1. Comparison of $T_c$ of the hydrocarbon superconductors . . . . .	100
B.1. Clar structure of phenanthrene and anthracene . . . . .	104
B.2. Clar structures of different hydrocarbons . . . . .	105
C.1. Comparison between LDA and GW densities of valence states for picene . . . . .	108

*“Ich habe keine besondere Begabung,  
sondern bin nur leidenschaftlich  
neugierig.”*

Albert Einstein

# 1

## Introduction And Motivation

**M**ANKIND was driven for ages by the thoughts to explore the world, that is around us. During the period often called the ‘Age of Discovery’, which started in the early 15<sup>th</sup> century and continued into the early 17<sup>th</sup> century, the Europeans engaged in intensive exploration of the world, in order to establish direct contact with other continents and discover new resources. 100 years ago, Roald Amundsen and some members of his crew (and shortly afterwards also Robert Falcon Scott) being the first humans who reached the Geographic South Pole. And even in the middle of the last century and in the following decades some individuals were driven by the force to discover new and unknown places on this earth, e. g., Herman Buhl who made the first unaccompanied ascent of an eight-thousander peak without supplemental oxygen, or Edmund Hillary and Tenzing Norgay who became the first climbers confirmed at having reached the summit of Mount Everest in the year 1953. Interestingly, by focussing on scientific research, one can easily identify similarities between these two “different worlds”. The search for new materials with novel properties or the improvement of their attributes as well as the qualities of existing systems may considered to be some of the leading motives that promote scientists for their work. In other words, exploration—investigating unknown territory—can be used metaphorically relating to science, attempting to develop an initial, rough understanding of some new and exceptional phenomenon.

As one of this ground-breaking discoveries in the field of solid-state physics, one may decidedly attribute the results of Heike Kamerlingh-Onnes at the beginning of the 20<sup>th</sup> century. He was the first who liquefied helium and opened thereby a new door to a low temperature range, which was inaccessible before [1]. Subsequently, in the year 1911 he discovered one of the most fascinating and otherwise much discussed phenomenon in physics—superconductivity—which describes a vanishing electrical resistance and expulsion of magnetic fields occurring in certain materials when cooled below a characteristic critical transition temperature  $T_c$  [2]. Since that time researchers spend a lot of effort to increase the value of the transition temperature and furthermore to understand the mechanism behind this peculiar behavior. But it lasted more than 70 years until a new euphoria started with the report by Bednorz and Müller about high- $T_c$  superconductivity in a new

class of ceramics [3]. Over the past 25 years scientists have begun to discover various classes of 'high- $T_c$ ' superconductors, including the copper oxides and, most recently, the iron arsenides, whereas  $T_c$  could be increased up to 155 K in the former and 55 K in the latter case, respectively.

Organic materials, in particular carbon-based materials, are well-known prototypes of electrical insulators and semiconductors. But even before the discovery of graphene, which was awarded the Nobel Prize in Physics in 2010 opening exciting perspectives for fundamental and applied research [4], many other carbon-based systems, such as nanotubes, fullerenes and graphite have played an important role in several fields, including superconductivity. In particular, the superconducting (alkali-metal doped) fullerides have attracted much attention, and rather high transition temperatures could be realized (e. g.,  $T_c$  of 18 K in  $K_3C_{60}$  [5] or  $T_c = 38$  K in  $Cs_3C_{60}$  [6, 7]). Their novel and exceptional electronic properties are attributed to the delocalized  $\pi$ -electrons. Thus, doping of such materials with  $\pi$ -electron networks might bring out novel physical properties, such as superconductivity, as well in other compounds.

However, in the case of organic superconductors, no new systems with high  $T_c$ 's similar to those of the fullerides have been discovered in the past decade. But in 2010 the field was renewed with the discovery of superconductivity in alkali-doped picene (a hydrocarbon molecule with five benzene rings condensed in a zigzag manner) with a  $T_c$  up to 18 K in case of  $K_3$ picene. After that, superconductivity was also reported in other alkali-metal intercalated polycyclic aromatic hydrocarbons, such as phenanthrene ( $T_c = 5$  K), coronene ( $T_c = 15$  K), and 1,2;8,9-dibenzopentacene ( $T_c = 33$  K). Especially in the latter case,  $T_c$  is higher than in any other organic superconductor besides the alkali-metal doped fullerides. Therefore, these small-molecule-based materials open up new avenues for research into superconductivity and it becomes more and more evident, that organic materials serve as a fascinating field for materials science and solid state physics. In this context, it is reasonable to expect that, through carrier doping, higher  $T_c$  superconductivity can be realized in other aromatic hydrocarbon systems. Interestingly, hydrocarbons are essential to everyday life, for example, the saturated hydrocarbons known as alkanes are prime constituents of fuels and picene can be found occurring naturally in coal tar.

Anyhow, the nature and range of parameters for superconductivity in intercalated hydrocarbons are under lively debate at the moment. It is however clear that they are strongly related to two families of carbon-based superconductors. On the one hand graphite intercalation compounds, which are conventional BCS-like superconductors [8, 9] and on the other hand alkali-doped fullerenes, which are characterised by a non-trivial interplay between strong local electron-phonon and on-site Coulomb correlations [10].

The prerequisite for the understanding of physical properties of new materials is the knowledge of the electronic structure or electronic properties, both in the normal state as well as in the superconducting state. In this context, this work presents a summary of the investigations on the electronic structure of several aromatic hydrocarbon systems using electron energy-loss spectroscopy (EELS). EELS studies of other undoped and doped molecular materials in the past have provided useful insight into their electronic properties.



---

Furthermore, EELS allows momentum-dependent measurements of the loss function, i. e., the observation of nonvertical transitions within the band structure of a solid, the identification of dipole-forbidden excitations and the determination of the dispersion of excitons, interband transitions, or charge-carrier plasmons. Additionally, the comparison with theoretical data gives insight into the nature of observed spectral features and helps to understand the mechanism behind.

The necessary steps to reach the goal of a deeper understanding of this ‘new’ class of superconductors as well as possible ways of its interpretation are to be described in the subsequent chapters. In this thesis, the results are presented with regard to fundamental research. The outline of this work is as follows: *Ch. 2* describes the experimental method of choice, electron energy-loss spectroscopy, and gives a short overview over the sample manufacturing and preparation. Furthermore, some basics required for the later discussion, especially from the theoretical point of view, are introduced. *Ch. 3* starts with some general remarks on carbon based materials. The focus is on the selected materials, in particular the crystal structure of the investigated aromatic hydrocarbons. Moreover, some remarks about the electronic excitations are given. At the end of the chapter, we present an overview of current scientific knowledge about superconductivity in this “new” class of organic superconductors. In *Ch. 4* and *5* the results of this work are presented. In detail, the first experimental part deals with the electronic properties for the undoped systems, whereas in *Ch. 5* we focus on the doping introduced changes in the electronic structure and their momentum dependence. A general summary trying to put everything into a more global picture is given afterwards in *Ch. 6* followed by an outlook. Some additional informations, which did not fit into the previous framework, are discussed in the appendices.

## Remark

For more clarity most of the formula are given with all universal constants set to unity except for those, where it is necessary to gain information of numeric values. This is done for convenience but also in order to emphasize the main physical statements.

For data evaluation and plotting, the IGORPRO software with extensions implemented by R. Schuster and R. Kraus was used. All other figures and sketches—as far as they were not taken from the reference source—were prepared using L<sup>A</sup>T<sub>E</sub>X’s PGF and TikZ package, respectively. Typesetting was done in L<sup>A</sup>T<sub>E</sub>X using the Kile frontend together with the *scrbook* class.





*"Despite my detour over the mountains, I've come further than I would have done on the flat trails."*

Reinhard Karl\*

# 2

## Electron Energy-Loss Spectroscopy

### 2.1. Introduction

ONE precondition to understand the principles, which lead to the fascinating properties of the systems that are around us, is to be able to perform accurate measurements, regardless of how complex they are. Spectroscopy, as the study of the interaction between matter and some kind of particle or field, has played a key role in the evolution of modern physics. Moreover, scattering experiments with fast particles have become an important tool, because compared to absorption experiments they make it possible to investigate not only the energy but also the spatial dependence of the possible excitations of matter. Today, scattering experiments are the basic principle to gain our experimental knowledge about the (electronic) structure of solids and are accessible in a wide energy range between meV and GeV.

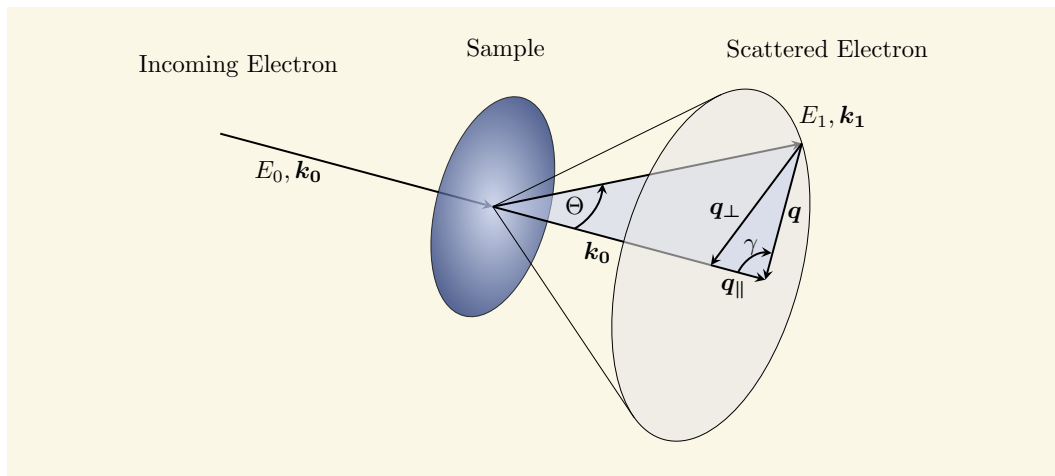
Inelastic electron scattering or electron energy-loss spectroscopy (EELS) can be seen as one of the most versatile spectroscopic methods for the study of condensed matter and has become a standard method for investigating the collective excitations of electrons, i. e. plasmons. Furthermore, it provides information on interband transitions between valence bands and conduction bands as well as on core-level excitations in order to learn more about the unoccupied density of states. In an EELS experiment, a beam of electrons is transmitted through a crystal whereby an interaction with the electronic system occurs and thus be subjected to an energy loss. This means that an energy transfer between the beam of charged particles and the system takes place. Hence, EELS at energies below 25 eV can be compared with light scattering spectroscopy whereas at higher energies it is in competition with X-ray absorption spectroscopy. In addition, EELS has the great advantage that the momentum transfer can be varied (which is not possible in optical spectroscopy) and therefore it becomes possible to measure dynamics of different types of excitations in momentum space for a wide range of samples from simple metals to complex oxides and even molecular solids.

---

\*Reinhard Karl (1946-1982). German mountaineer, photographer and writer.

In the following chapter we will describe on the one hand the general principle of EELS measurements in transmission (another possibility is to perform EELS in reflection to study, e. g., surface dynamics like the dispersion of surface phonons or to monitor epitaxial growth) supported by some theoretical remarks about scattering theory with electrons in general and the properties of the dielectric function. On the other hand we will give an insight into the experimental techniques like sample preparation and crystal growth, and list further details about the spectrometer itself and its performance.

## 2.2. Working Principle



**Figure 2.1.** | The basic scheme for an EELS experiment in transmission. The electrons with an energy  $E_0$  and an incoming momentum  $k_0$  are focused on the thin sample and scattered under an angle  $\theta$ . The momentum transfer  $q$  which takes place during the scattering process results in an energy transfer  $\omega$  in the sample. Furthermore, it is also possible to perform elastic scattering (Bragg scattering) by setting the energy loss to zero.

The basic scattering geometry of a usual electron scattering experiment is shown in Fig. 2.1. A beam of rather fast electrons, specified by a momentum  $\hbar k_0$ , is focused on a thin ( $\approx 100$  nm) film of the sample under investigation. While passing through the sample a fraction of the beam electrons is inelastically scattered by an angle  $\theta$  away from the initial direction. This leads to a momentum- ( $\hbar q$ ) and energy-transfer ( $\hbar\omega$ ) given by

$$\hbar q = \hbar k_0 - \hbar k_1 \quad (2.1)$$

and

$$\hbar\omega = E_0 - E_1 = \frac{\hbar^2(k_0^2 - k_1^2)}{2m} \quad (2.2)$$

and will as a consequence leave the sample in an excited state, which is characterized by the energy and momentum it acquired from the electrons in the beam.

According to Fig. 2.1 the momentum transfer  $q$  can be decomposed into components parallel and perpendicular to the incoming momentum  $k_0$

$$q^2 = q_{\parallel}^2 + q_{\perp}^2. \quad (2.3)$$

It is important to realize that the primary energy of the electrons is rather high ( $E_0 = 172$  keV) which leads to a large value of  $k_0 \sim 230 \text{ \AA}^{-1}$  (see Eq. A.2). Comparing this to a typical extension of a Brillouin zone inside a solid which is of the order  $1 \text{ \AA}^{-1}$  one arrives at small scattering angles  $\theta$  and therefore

$$q_{\perp} = k_1 \sin \theta \cong k_1 \theta \cong k_0 \theta. \quad (2.4)$$

Furthermore, the cosine theorem yields (cf. Fig. 2.1)

$$k_1^2 = k_0^2 + q^2 - 2k_0q \cos \gamma \cong k_0^2 - 2k_0q \cos \gamma. \quad (2.5)$$

Therefore the excitation energy reads

$$\hbar\omega \cong \frac{\hbar^2(k_0^2 - k_1^2)}{2m} \cong \frac{\hbar k_0}{m} \cdot q \cos \gamma = \frac{\hbar k_0}{m} \cdot q_{\parallel}. \quad (2.6)$$

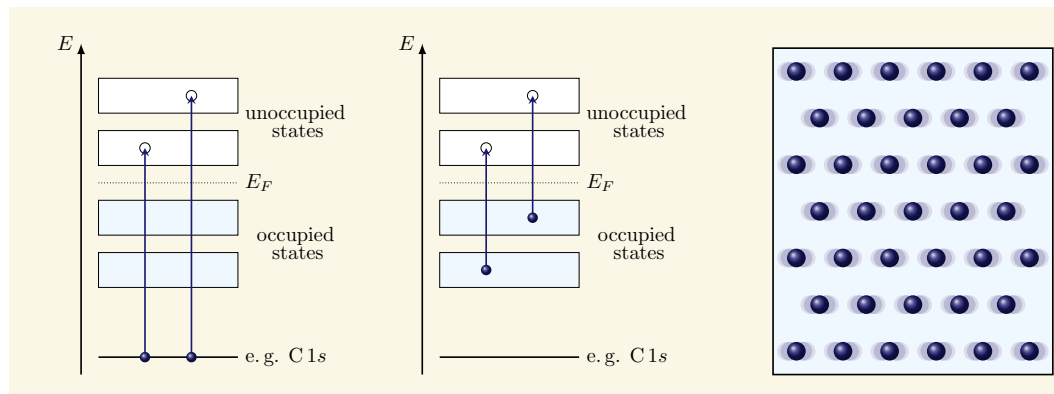
For a typical energy loss in the order of magnitude of  $\hbar\omega \sim 10$  eV and at experimentally observed scattering angles of  $\theta \sim 0.25^\circ$ , we obtain the important result

$$\frac{q_{\parallel}}{q_{\perp}} = \frac{m\omega}{\hbar k_0^2 \theta} \sim 10^{-3} \quad (2.7)$$

and so the momentum transfer can be regarded as lying completely within the plane which is perpendicular to the incoming electron beam. To obtain information beyond this particular plane one has to rotate the sample with respect to the beam. Another very important conclusion is that  $q \sim q_{\perp}$  stays constant over a relatively large energy range (up to 70 eV). This fact is essential for a correct evaluation of the dispersion measurements as well as the Kramers-Kronig analysis (see Sec. 2.3).

### 2.2.1. Possible EELS Excitations

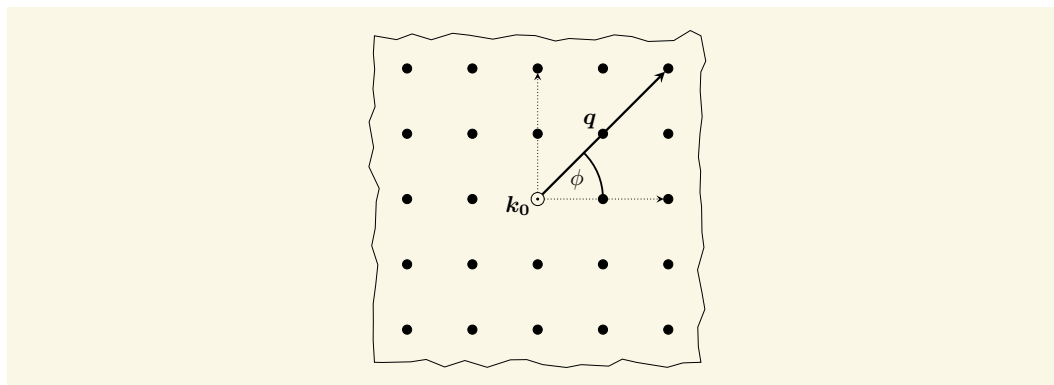
Two basic measuring processes can be distinguished in the EELS experiment. On the one hand one is able to investigate the electronic properties of a sample by measuring the energy-loss of electrons for fixed momentum transfer, which gives access to electronic excitations within the solid. The possible excitations are shown schematically in Fig. 2.2.



**Figure 2.2.** | Electronic excitations accessible in EELS. Note that the left and the middle panel represent the band scheme, while the right panel depicts the solid and its valence electrons.

The left panel of Fig. 2.2 represents the excitations of core level electrons of the individual elements. These excitations appear at high energies (e. g., around 284 eV for the carbon 1s level or 297 eV and 299 eV for the potassium  $2p_{1/2}$  and  $2p_{3/2}$  levels) and are of high importance, especially for the investigation of the doping level of a sample.

The interband excitations that are shown in the middle panel of Fig. 2.2 occur at energies up to a few electron volt and represent the excitation from an occupied state of the valence band of the solid to an unoccupied state of the conduction band. In case of small values of the momentum transfer (up to  $0.1 \text{ \AA}^{-1}$ ), these measurements are comparable with optical spectroscopy. Furthermore, also plasmon excitations, i. e., collective oscillations of the conduction electrons, can be detected (cf. Fig. 2.2 (right panel)).



**Figure 2.3.** | Sketch of the momentum transfer in the sample plane perpendicular to the incoming electron beam for a special case of a square lattice. Whenever the momentum transfer  $q$  connects two points of the reciprocal lattice the Bragg condition is fulfilled and there appears a peak in the elastic scattering spectrum.

In addition to the possibility of inelastic scattering processes with non-zero energy-loss, it is also possible to perform elastic scattering (Bragg scattering) by setting the energy-

loss to zero. This allows the analysis of the lattice structure and is an important tool for investigations on single-crystals where the electronic properties may depend on the direction in the reciprocal lattice. Due to the two-dimensionality of the momentum transfer (cf. Sec. 2.2) one may write

$$q_{\perp} = q = q_0 e^{i\phi}$$

and—as can be seen from Fig. 2.3—by varying either  $\phi$  or  $q_0$  it is possible to adjust  $q$  within the reciprocal lattice in order to find directions fulfilling the Bragg condition which may then be taken to measure, e. g., the dispersion of a particular excitation along a well defined axis.

### 2.2.2. Scattering Theory - The EELS Cross Section

The essential quantity which is actually measured in the EELS experiment is the doubly differentiated cross section

$$\frac{d^2\sigma}{d\Omega d\omega'}$$

which gives the probability of detecting an electron in a scattering angle element  $d\Omega$  having lost an energy  $d\omega$  compared to its initial energy  $E_0$ . Quantum mechanically, the scattering process can be described by a transition from an initial state  $|n_0, k_0\rangle$  (incident electron plus electrons in the solid in the ground state) to a final state  $|n_1, k_1\rangle$  (outgoing electron plus excited electrons in the solid). The interaction of the scattered electrons with the charges in the sample is driven by the Coulomb potential which is given by

$$H_{int} = \frac{e^2}{q^2}.$$

Due to their high kinetic energy, the incident electrons are distinguishable from electrons in the solid and only weak interactions of the electrons with the sample have to be considered. Then the differential cross-section can be written in the Born approximation [11, 12]

$$\frac{d^2\sigma}{d\Omega d\omega} = \sum_{n_0, n_1} |\langle n_1, k_1 | H_{int} | n_0, k_1 \rangle|^2 \delta(E_{n_0} + E_0 - E_{n_1} - E_1) \quad (2.8)$$

with the initial (final) states of the incoming (outgoing) electrons

$$|k_l\rangle \propto e^{ik_l r} \quad l = 0, 1$$

and the corresponding ones for the sample  $|n_l\rangle$ . The initial and final states can be written as simple products

$$|n_l, k_l\rangle = |n_l\rangle|k_l\rangle,$$

which leads to a new equation for the differential cross-section

$$\frac{d^2\sigma}{d\Omega d\omega} = \left(\frac{d\sigma}{d\Omega}\right)_{Ruth} \cdot S(\mathbf{q}, \omega), \quad (2.9)$$

where

$$\left(\frac{d\sigma}{d\Omega}\right)_{Ruth} = \frac{4}{a_0^2 q^4}$$

is the elastic Rutherford cross-section with  $a_0$  being the Bohr radius. The dynamic structure factor  $S(\mathbf{q}, \omega)$  is defined by

$$S(\mathbf{q}, \omega) = \frac{1}{N} \sum_{n_0, n_1} p_{n_0} \left| \langle n_1 | \sum_j e^{i\mathbf{q}r_j} | n_0 \rangle \right|^2 \delta(E_{n_0} - E_{n_1} + \omega). \quad (2.10)$$

The factor  $1/N$  has been included because the cross-section is defined per electron. The operator in the matrix elements is the Fourier transform of the electron density operator

$$n_{\mathbf{q}} = \sum_j e^{-i\mathbf{q}r_j}$$

To eliminate the  $\delta$  function, a time-dependent operator

$$n(\mathbf{q}, t) = e^{iH_0 t} n(\mathbf{q}) e^{-iH_0 t}$$

is introduced and the  $\delta$ -function can be written as

$$\delta(E_{n_0} - E_{n_1} + \omega) = \frac{1}{2\pi} \int dt e^{i(E_{n_0} - E_{n_1} + \omega)t}.$$

This close relationship between the structure factor and the density-density correlation function was first derived by Van Hove [11].

With the help of the Kubo formalism of linear-response theory [13, 14] and the fluctuation-dissipation theorem [15, 16] one may establish a relation between the dynamical structure factor  $S(\mathbf{q}, \omega)$  and the dielectric function  $\epsilon(\mathbf{q}, \omega)$ . This is an example of a very general principle in statistical physics, namely the fluctuation-dissipation theorem which always connects some sort of correlation function (the density-density correlation in this case) with a response function  $\epsilon(\mathbf{q}, \omega)$



$$S(\mathbf{q}, \omega) = \frac{q^2}{4\pi e^2} \frac{1}{1 - e^{-\beta\omega}} \operatorname{Im} \left( -\frac{1}{\epsilon(\mathbf{q}, \omega)} \right), \quad (2.11)$$

with  $\beta = 1/kT$  ( $k$  is the Boltzmann's constant). For typical electronic excitation energies  $\omega \gg 1/T$  and neglecting the Bose factor in the previous relation we obtain the final result

$$\frac{d^2\sigma}{d\Omega d\omega} = \frac{\text{const.}}{q^2} \cdot \underbrace{\operatorname{Im} \left( -\frac{1}{\epsilon(\mathbf{q}, \omega)} \right)}_{\text{Loss Function}}, \quad (2.12)$$

which relates the intensity measured in an EELS experiment to the dielectric function which provides access to the electronic structure of a sample under investigation.

### 2.3. The Dielectric Function

As one can see in Sect. 2.2.2, it is the dielectric function  $\epsilon(\mathbf{q}, \omega)$ , which provides the main ingredient to the signal measured in an electron energy-loss spectroscopy experiment. Therefore, it is instructive to introduce some of its properties to get a better understanding of the subsequent discussion.

In general, the dielectric function  $\epsilon(\mathbf{q}, \omega)$  describes the response of a system to a external perturbation. The addition of an external charge density  $\rho(\mathbf{r}, t)$  gives rise to a change in the density of the quasi-free conduction electrons within the system and screen, as a consequence, the perturbation charges. The most general form of the dielectric function is given by

$$E(\mathbf{r}, t) = \int d\mathbf{r}' \int dt' \epsilon^{-1}(\mathbf{r}, \mathbf{r}', t - t') \cdot \mathbf{D}(\mathbf{r}', t'). \quad (2.13)$$

For a homogeneous system the dielectric function depends only on the difference  $\mathbf{r} - \mathbf{r}'$  which modifies the above relation after a Fourier transform into

$$E(\mathbf{q}, \omega) = \epsilon^{-1}(\mathbf{q}, \omega) \cdot \mathbf{D}(\mathbf{q}, \omega). \quad (2.14)$$

Applying the jellium model one assumes that in equilibrium, the electronic and the ionic charge densities just compensate each other. Moreover, the perturbation charge is assumed to polarise only the more mobile electronic system while the ionic charges remain homogeneously distributed. The overall charge density then is the sum of  $\rho_{ext}$  and the induced charge density  $\rho_{ind}$ , which is produced in the electron gas:

$$\rho_{tot}(\mathbf{q}, \omega) = \rho_{ext}(\mathbf{q}, \omega) + \rho_{int}(\mathbf{q}, \omega). \quad (2.15)$$

Furthermore, from the Maxwell equations it is well known that the electric field  $E$  and the displacement  $D$  are caused by the total and external charges, respectively:

$$i\mathbf{q} \cdot \mathbf{D}(\mathbf{q}, \omega) = \rho_{ext}(\mathbf{q}, \omega) \quad (2.16)$$

$$i\mathbf{q} \cdot \mathbf{E}(\mathbf{q}, \omega) = \rho_{tot}(\mathbf{q}, \omega). \quad (2.17)$$

With the help of the relations given above, Eqn. 2.14 can be expressed as

$$\rho_{int}(\mathbf{q}, \omega) = \left( \frac{1}{\epsilon(\mathbf{q}, \omega)} - 1 \right) \rho_{ext}(\mathbf{q}, \omega). \quad (2.18)$$

This result shows that if  $\epsilon(\mathbf{q}, \omega)$  is very large it can be assumed that  $\rho_{int}(\mathbf{q}, \omega) \simeq -\rho_{ext}(\mathbf{q}, \omega)$ . The screening of the perturbation charges by the induced charges in the electron gas is virtually complete. The other limiting case of vanishing  $\epsilon(\mathbf{q}, \omega)$  corresponds to an intrinsic instability of the system, i. e., there is a redistribution of charges without an external driving force. According to Eqn. 2.18, arbitrarily small perturbation charges then suffice to provoke finite density fluctuations in the system of the conduction electrons. These collective excitations of the electronic system are associated with the quasi-particle called plasmon.

Another quantity of interest is the susceptibility

$$\chi(\mathbf{q}, \omega) = \frac{\rho_{int}(\mathbf{q}, \omega)}{v_{ext}(\mathbf{q}, \omega)}, \quad (2.19)$$

where  $v_{ext}(\mathbf{q}, \omega)$  stands for the external potential that is created by the external charge density according to the Poisson equation. It is possible to connect the susceptibility with the dielectric function according to

$$\frac{1}{\epsilon(\mathbf{q}, \omega)} = 1 + v_q \chi(\mathbf{q}, \omega), \quad (2.20)$$

where  $v_q = 1/q^2$  represents the Fourier transform of the Coulomb potential.

In order to learn more about the properties of the dielectric function  $\epsilon(\mathbf{q}, \omega)$  as well as plamonic excitations, the following paragraph describes some properties of  $\epsilon(\mathbf{q}, \omega)$  for a simple model of interacting electrons. Notice that this represents only an introduction to some ideas that will be of relevance in the subsequent discussion of the data. For further reading of extensive treatments comprehensive reviews are available (see, e. g., Ref. 17–19). Taking realistic particle interactions into account, an exact calculation of the susceptibility or equivalently of the dielectric function is no longer possible. Therefore the following discussion presents an approximation of the jellium model, i. e., the toy-model of electrons interacting with a homogeneous positive background, whose Hamiltonian is defined by:

### 2.3. The Dielectric Function

$$H = \sum_k \omega_k c_k^\dagger c_k + \sum_k \frac{2\pi e^2}{k^2} (\rho_k^\dagger \rho_k - \hat{N}) = \sum_i \frac{p_i^2}{2m} + \sum_k \frac{2\pi e^2}{k^2} (\rho_k^\dagger \rho_k - \hat{N}), \quad (2.21)$$

with the single particle energies  $\omega_k$ , the creation (annihilation) operators  $c_k^\dagger$  ( $c_k$ ), the density operator  $\rho_k = \sum_i \delta(\mathbf{r} - \mathbf{r}_i)$  and the number operator  $\hat{N}$ . With the help of the equation of motion introduced in Ref. 20

$$\frac{\partial^2 \rho_k}{\partial t^2} + \omega_p^2 \rho_k = \sum_i \left( \frac{\mathbf{k} \cdot \mathbf{p}_i}{m} - \frac{k^2}{2m} \right)^2 e^{-ikr_i} + \frac{4\pi e^2}{m} \sum_{q \neq k} \frac{\mathbf{k} \cdot \mathbf{q}}{q^2} \rho_{q-k} \rho_k,$$

where  $\omega_p$  is the plasma frequency

$$\omega_p = \sqrt{\frac{4\pi N e^2}{m}}$$

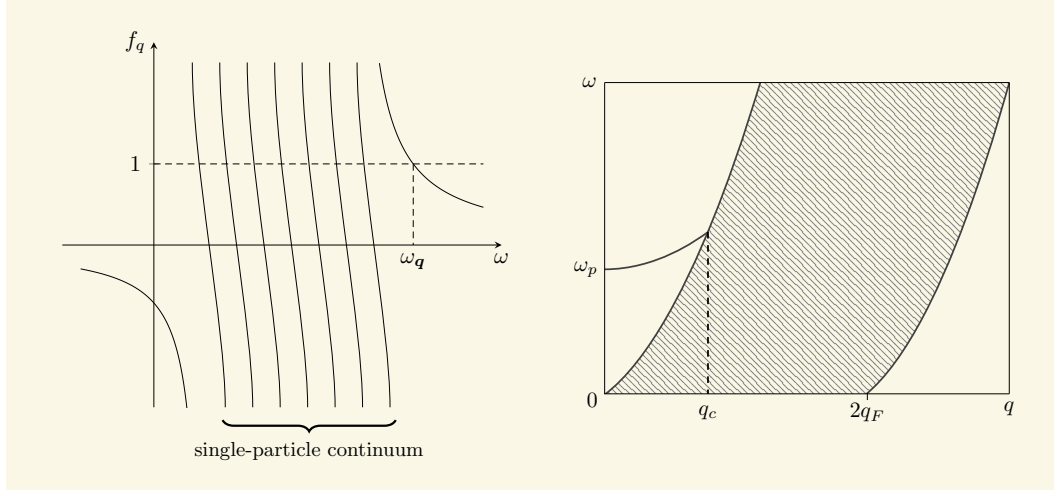
and the approximation that the electrons only respond to the total field, which is composed of the external field and the field induced by the external field, it is possible to describe collective excitations. This approach was first formulated by Bohm and Pines and is called random-phase approximation (RPA) [21, 22]. The Coloumb interaction results in a density oscillation with the well-known ‘‘plasma’’ frequency, with other words the electron gas will oscillate at a characteristic frequency  $\omega_p$  like a harmonic oscillator. The quanta of this collective modes are called plasmon. For higher momenta the collective motion of the electron gas as a whole loses its meaning and the individual properties of single electrons become more important. In the RPA, the electrons respond to the applied external field and the averaged potential of the electron gas. Any fluctuations and short range inhomogeneities are ignored. Therefore, the RPA is valid in the weak coupling regime, i. e., this assumption requires high electron densities that homogenize all local fluctuations quickly by effective dielectric screening. The critical parameter is the Wigner-Seitz radius  $r_s$ , which describes the mean distance between two electrons in the system. It is defined as

$$r_s = \frac{1}{a_0} \left( \frac{3}{4\pi n} \right)^{1/3},$$

where  $a_0 = 0.529 \text{ \AA}^{-1}$  is the Bohr radius and  $n$  represents the particle density. In typical metallic systems the  $r_s$ -value lies in the range of  $2 < r_s < 6$ . Therefore, one may expect some influences of the electron-electron interactions on the electronic properties and one has to keep in mind that RPA cannot predict the quantitatively behavior of real metals, but it works well in special cases and allows to retrieve qualitative behavior.

Finally one can obtain the generalized susceptibility in the RPA. It reads

$$\chi(\mathbf{q}, \omega) = \frac{\chi^0(\mathbf{q}, \omega)}{1 - v_q \chi(\mathbf{q}, \omega)} =: \chi_{RPA}(\mathbf{q}, \omega) \quad (2.22)$$



**Figure 2.4.** | Left panel: Graphic illustration of the determination of the zeros of the Lindhard function. The horizontal dashed line indicates the position where  $\chi^0(\mathbf{q}, \omega) = v_q^{-1}$  corresponds to the possible electronic transitions. Right panel: The  $(\mathbf{q}, \omega)$ -plane and the relation between the plasmon mode (solid line) and the single particle continuum (hatched area). In the RPA the plasmon exists only up to a critical momentum  $q_c$  where it enters the continuum and decays into particle-hole pairs. This figure is reproduced from Ref. 24.

with the susceptibility of the non-interacting system

$$\chi^0(\mathbf{q}, \omega) = \frac{2}{V} \sum_k \frac{n_k^0 - n_{k+q}^0}{\omega + \omega_k^0 - \omega_{k-q}^0 + i\delta}, \quad (2.23)$$

where the  $n_k^0$  refer to the occupation number of the free system and the damping  $\delta$  is introduced for the sake of normalization. Together with Eq. 2.20 the dielectric function in the RPA is given by

$$\epsilon_{RPA}(\mathbf{q}, \omega) = 1 - v_q \chi^0(\mathbf{q}, \omega) = 1 - v_q \sum_k \frac{n_k^0 - n_{k+q}^0}{\omega + \omega_k^0 - \omega_{k-q}^0 + i\delta}. \quad (2.24)$$

This expression is also called the Lindhard function [23]. From Eq. 2.18 and Eq. 2.20 it is evident that the zeros of the dielectric function are of particular interest, because they determine the proper frequencies of the system. From Eq. 2.24 one can obtain them by applying the condition

$$f_q(\omega) \equiv v_q \chi^0(\mathbf{q}, \omega) \stackrel{!}{=} 1.$$

The function  $f_q(\omega)$  exhibits a dense series of poles within the single particle continuum (cf. left panel of Fig. 2.4). In the thermodynamic limit, these are congruent with the single-particle excitations, i. e., the formation of particle-hole pairs. There is, however, another

### 2.3. The Dielectric Function

solution, which fulfills the required condition and is outside the continuum at higher energies and therefore corresponds to a collective excitation in the electron gas. This is the so-called plasma oscillation or plasmon.

A feature of special relevance for the later discussion is the momentum dependence of the plasma frequency, i. e., the plasmon dispersion which can be derived from the Lindhard function under some assumptions [19, 23]. Finally, the plasmon dispersion can be expanded into a Taylor series at  $q = 0$  given by

$$\omega(q) = \omega_p + \alpha q^2 + \mathcal{O}(q^4); \quad \alpha = \frac{3}{5} \frac{E_F}{\omega_p}. \quad (2.25)$$

Qualitatively, the excitation spectrum as sketched in Fig. 2.4 (right panel) is found and concludes the results for the relation between the single-particle and collective modes in the RPA. There is a continuum of particle-hole excitations which scales quadratically with momentum. Moreover, a general behavior that can be deduced from Eq. 2.25 is a quadratic plasmon dispersion that starts at  $q$  equal zero and will certainly run into the free particle decay at a finite critical wave vector  $q_c$ . Interestingly, there are numerous examples in the literature that this is also realized for real materials. We will however observe and discuss partly remarkable deviations from this theoretical prediction in the Ch. 4 and Ch. 5.

As the dielectric function—and also the loss function—are so-called response functions they reveal several very useful properties. First, from the fact that the response of the system is causal, one obtains the Kramers-Kronig (KK) relations

$$\operatorname{Re} \left( \frac{1}{\epsilon(\mathbf{q}, \omega)} \right) - 1 = \frac{1}{\pi} \mathcal{P} \int \frac{d\omega'}{\omega' - \omega} \left[ \operatorname{Im} \left( \frac{1}{\epsilon(\mathbf{q}, \omega')} \right) \right] \quad (2.26)$$

$$\operatorname{Im} \left( \frac{1}{\epsilon(\mathbf{q}, \omega)} \right) = -\frac{1}{\pi} \mathcal{P} \int \frac{d\omega'}{\omega' - \omega} \left[ 1 - \operatorname{Re} \left( \frac{1}{\epsilon(\mathbf{q}, \omega')} \right) \right], \quad (2.27)$$

which are an essential tool to deduce the complete dielectric function from the signal measured in the EELS experiment ( $\mathcal{P}$  denotes the Cauchy principal value or principal part of the integral\*). With that it is possible to derive, in principle, all optical constants like, e. g., the optical conductivity, the refractive index etc. [25]. Besides the KK equations there exist more relations, so called sum rules, that are important for the evaluation of the data as well as for the calibration of the loss function and the consistency check of our KK analysis. One of these sum rules relates the loss function and the dielectric function to the density  $N$ , of all valence electrons:

\*The principal part of an integral that has a divergence at  $c$  within the integration range  $a \rightarrow b$  is defined as:

$$\mathcal{P} \int_a^b f(x) dx = \lim_{\delta \rightarrow 0} \left( \int_a^{c-\delta} f(x) dx + \int_{c+\delta}^b f(x) dx \right).$$

$$\int_0^{\infty} d\omega \omega \operatorname{Im} \left( -\frac{1}{\epsilon(\mathbf{q}, \omega)} \right) = \int_0^{\infty} d\omega \omega \epsilon_2 = \omega_p^2 \cdot \frac{\pi}{2} \propto N. \quad (2.28)$$

With that, the strengths of possible transitions are not independent from each other but are balanced in a way that enhancing the weight in a particular energy range of the spectrum by, e. g., the appearance of a phase transition will reduce the intensity in another energy window to keep the above given integral at a constant value. In practice, calculations as well as experiments are of course always restricted to a finite energy window and one may evaluate partial sum-rules according to

$$\int_{\omega_0}^{\omega_1} d\omega \omega \operatorname{Im} \left( -\frac{1}{\epsilon(\mathbf{q}, \omega)} \right) = \omega_p^2 \cdot \frac{\pi}{2} (N_{eff}/N),$$

that provide access to an effective number of charge carriers  $N_{eff}$  contributing to a particular type of excitation within a given energy range.

In conclusion, for metallic systems a further sum rule can be employed [12], which allows an additional check of our analysis:

$$\int_0^{\infty} d\omega \frac{\operatorname{Im} \left( -\frac{1}{\epsilon(\mathbf{q}, \omega)} \right)}{\omega} = \frac{\pi}{2}. \quad (2.29)$$

At the end of this section we want to mention that the RPA is a quite good approach but real materials show a number of properties that may complicate a theoretical treatment significantly. In the following we will briefly introduce some of them, which are of relevance for the later discussion. First of all, as a mean-field theory, RPA does not take into account short-range exchange and correlations between electrons. The local correlation and exchange interactions can be represented by a local field correction function  $G(\mathbf{q}, \omega)$ . Within the concept of the *a priori* unknown  $G(\mathbf{q}, \omega)$  the dielectric function is given by

$$\epsilon(\mathbf{q}, \omega) = 1 - \frac{v_q \chi^0(\mathbf{q}, \omega)}{1 + G(\mathbf{q}, \omega) v_q \chi^0(\mathbf{q}, \omega)}.$$

Up to now we have considered a homogenous electron gas. If one has to deal with inhomogeneous electron systems one has to take into account so-called crystal local-fields effects, which were first studied by Ehrenreich, Cohen [26], Adler [27], and Wiser [28]. In real crystals it is necessary to consider variation of the field on lattice distance, because of the interaction of electrons with the crystal lattice. That means that the polarization due to an external perturbation fluctuates on the atomic scale. The periodicity within a crystalline solid leads to the condition

$$\epsilon(\mathbf{r}, \mathbf{r}', t) = \epsilon(\mathbf{r} + \mathbf{R}, \mathbf{r}' + \mathbf{R}', t),$$

for the dielectric function with  $\mathbf{R}$  being a lattice vector. As a consequence this leads to a more complex expression for the electric field (cf. Eq. 2.14)

$$E(\mathbf{q} + \mathbf{G}, \omega) = \sum_{\mathbf{G}'} \epsilon_{\mathbf{G}\mathbf{G}'}^{-1}(\mathbf{q} + \mathbf{G}, \omega) \cdot D(\mathbf{q} + \mathbf{G}', \omega), \quad (2.30)$$

with the notation

$$\epsilon_{\mathbf{G}\mathbf{G}'}^{-1}(\mathbf{q} + \mathbf{G}) = \epsilon^{-1}(\mathbf{q} + \mathbf{G}, \mathbf{q} + \mathbf{G}', \omega). \quad (2.31)$$

In Eq. 2.30 and 2.31  $\mathbf{q}$  is a wavevector within the first Brillouin zone and  $\mathbf{G}$  and  $\mathbf{G}'$  are reciprocal lattice vectors. An intriguing consequence of Eq. 2.30 is that an external plane wave perturbation  $D(\mathbf{q} + \mathbf{G}', \omega)$  (or the corresponding external charge density) will induce microscopic electric fields with the same frequency  $\omega$  but different and not even necessarily parallel wavevectors. The field components with  $\mathbf{G} \neq \mathbf{G}'$  (off-diagonal components of the dielectric matrix  $\epsilon_{\mathbf{G}\mathbf{G}'}$ ) that mix the various Bragg reflexes are called crystal local field effects (LFE). For small values of momentum one averages over several unit cells which results in the macroscopic response given by

$$\epsilon(\mathbf{q}, \omega) = \lim_{q \rightarrow 0} \frac{1}{\epsilon_{\mathbf{G}=0, \mathbf{G}'=0}^{-1}(\mathbf{q}, \omega)}.$$

In contrast, for higher values of  $\mathbf{q}$  one cannot, in general, neglect the influence of the lattice potential and one has to take the crystal local field effects into account.

### 2.3.1. The Drude-Lorentz-Model

To obtain an impression of the loss functions dependence on  $\omega$ , it is intuitive to consider the famous Drude-Lorentz-model which is—even though its simplicity—extremely helpful for an easy understanding of the physical processes behind optical properties and a rough understanding of the dielectric function.

It is assumed that all excitations of the electrons can be expressed by a sum of driven harmonic oscillators satisfying the equation of motion. For one oscillator this classical oscillator ansatz for the equation of motion in an external electric field  $E(x, t)$  leads to

$$\ddot{x} + \gamma \dot{x} + \omega_0^2 x = -\frac{e}{m} E(x, t),$$

where  $x$  represents the position of the electron,  $\gamma$  the damping factor,  $\omega_0$  the eigenfrequency of the oscillator,  $e$  the elementary charge and  $m$  the electron mass. Assuming  $E(x, t) = E_0(x)e^{-i\omega t}$  for the external field, the solution of the differential equation is then given by

$$x = -\frac{e}{m} \frac{E_0(x)}{\omega_0^2 - \omega^2 - i\gamma\omega}.$$

Using the definition of the macroscopic polarization  $P = -Nex$  (where  $N$  is the particle density) combined with some electrostatics leads to the result for the dielectric function  $\epsilon(\omega)$

$$\epsilon(\omega) = 1 + \frac{\omega_p^2}{\omega_0^2 - \omega^2 - i\gamma\omega},$$

with the plasma frequency  $\omega_p$  defined by

$$\omega_p = \sqrt{\frac{Ne^2}{\epsilon_0 m}}.$$

Extending this to more than one oscillator, like one would expect in a real material, we arrive at

$$\epsilon(\omega) = 1 + \sum_i \frac{f_i \omega_p^2}{\omega_{i0}^2 - \omega^2 - i\gamma_i \omega}.$$

Here the  $f_i$  are the oscillator strengths that measure the transition probability in the dipole regime. As can be seen  $\epsilon(\omega) \in \mathbb{C}$  and therefore it is possible to write

$$\epsilon(\omega) = \epsilon_1(\omega) + i\epsilon_2(\omega),$$

with

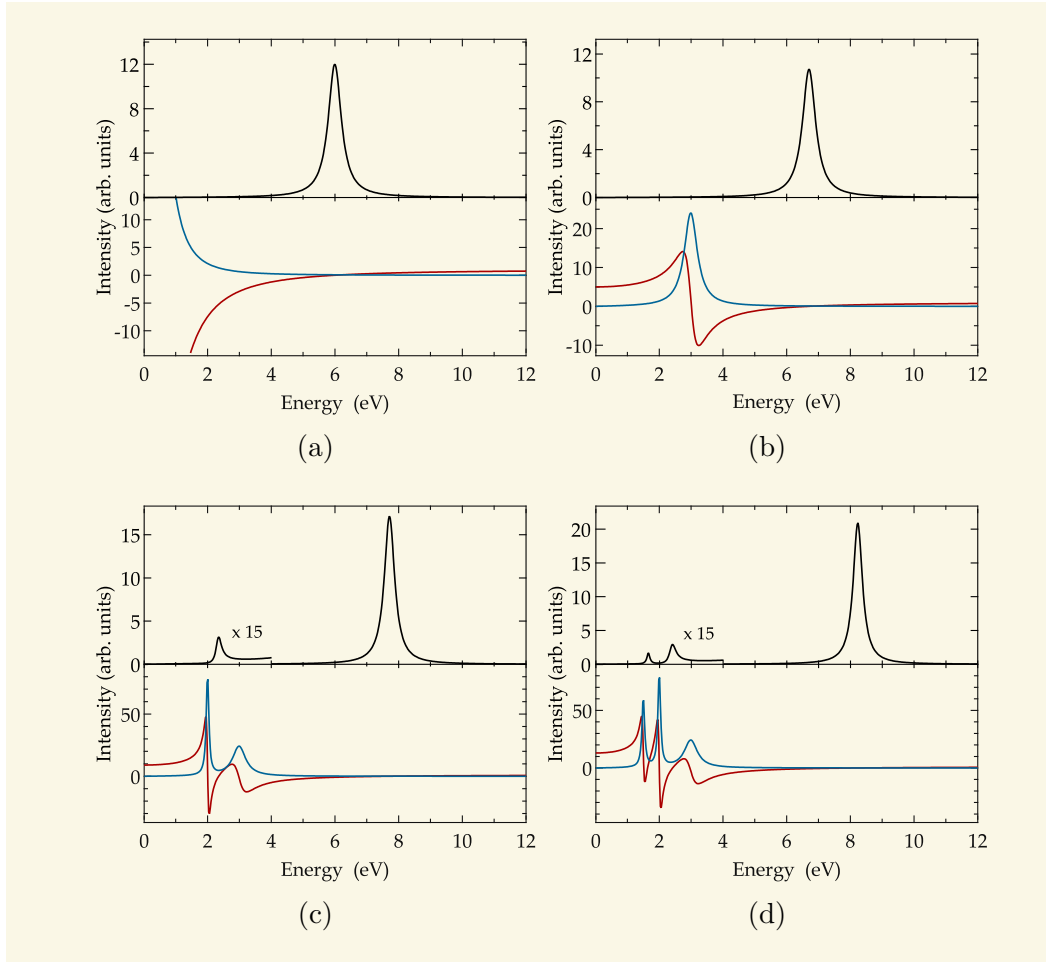
$$\begin{aligned} \epsilon_1(\omega) &= 1 + \omega_p^2 \sum_i \frac{f_i (\omega_{i0}^2 - \omega^2)}{(\omega_{i0}^2 - \omega^2)^2 + \gamma_i^2 \omega^2} \\ \epsilon_2(\omega) &= \omega_p^2 \sum_i \frac{f_i \gamma_i \omega}{(\omega_{i0}^2 - \omega^2)^2 + \gamma_i^2 \omega^2}. \end{aligned}$$

Finally, the loss function—the quantity measured in the EELS experiment—can be calculated

$$\text{Im} \left( -\frac{1}{\epsilon(\omega)} \right) = \frac{\epsilon_2(\omega)}{\epsilon_1^2(\omega) + \epsilon_2^2(\omega)}. \quad (2.32)$$



### 2.3. The Dielectric Function



**Figure 2.5.** | The loss function  $\text{Im}(-1/\epsilon(\omega))$  (black line),  $\epsilon_1$  (red line) and  $\epsilon_2$  (blue line) of solids using the Drude-Lorentz-model. (a) Free-electron metal, (b) Insulator, (c) Semiconductor with a strong interband transition across the fundamental gap, (d) Semiconductor with transitions related to defect states in the gap.

In order to illustrate typical dielectric properties of solids, Fig. 2.5 shows a summary of the qualitative behavior of the three quantities  $\epsilon_1(\omega)$ ,  $\epsilon_2(\omega)$  and  $\text{Im}(-1/\epsilon(\omega))$  calculated for various combinations of oscillators. The used parameters are listed in Tab. 2.1.

In the special case of a metallic system the electrons are assumed to be free, i. e.,  $\omega_0 \equiv 0$  which reduces the above equations for the real and imaginary part of the dielectric function to

$$\epsilon_1(\omega) = 1 - \omega_p^2 \sum_i \frac{f_i}{\omega^2 + \gamma_i^2}$$

$$\epsilon_2(\omega) = \omega_p^2 \sum_i \frac{f_i \gamma_i}{\omega(\omega^2 + \gamma_i^2)}$$

**Table 2.1.** | Parameters (in eV) for the Drude-Lorentz dielectric functions shown in Fig. 2.5

	Drude						Lorentz					
	$\omega_0$	$\gamma$	$\omega_p$	$\omega_{1_0}$	$\gamma_1$	$f_1$	$\omega_{2_0}$	$\gamma_2$	$f_2$	$\omega_{3_0}$	$\gamma_3$	$f_3$
(a)	0	0.5	6	-	-	-	-	-	-	-	-	-
(b)	-	-	-	3	0.5	6	-	-	-	-	-	-
(c)	-	-	-	3	0.5	6	2	0.1	4	-	-	-
(d)	-	-	-	3	0.5	6	2	0.1	4	1.5	0.1	3

and leads to dielectric functions shown in Fig. 2.5 (a). Here the damping  $\gamma$  is given by the scattering of charges by phonons or impurities. Close to the zero-crossing of  $\epsilon_1$  the loss function has a strong maximum due to collective excitations of the electrons, i. e., the plasmon.

In Fig. 2.5 (b), the dielectric function of a typical insulator is simulated by an oscillator having an energy equal to the gap energy  $\omega_g = 3$  eV. Then the plasmon energy is defined by

$$\omega_p = \sqrt{\omega_g^2 + \frac{Ne^2}{\epsilon_0 m}}.$$

The most important feature for a nonmetallic system is that the peak in the loss function does not necessarily correspond to the value of the true transition at  $\omega = \omega_0$ . The exact position of the loss function peak can be evaluated according to

$$\frac{\partial}{\partial \omega} \text{Im} \left( -\frac{1}{\epsilon(\omega)} \right) \stackrel{!}{=} 0 \quad \xrightarrow{\gamma \rightarrow 0} \omega = \sqrt{\omega_0^2 + \omega_p^2},$$

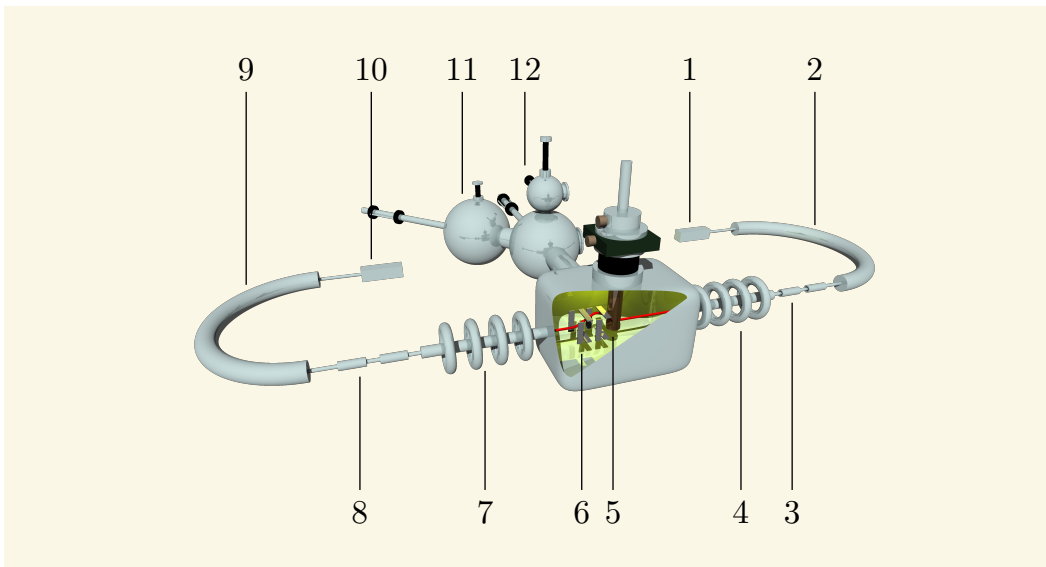
which in this case (vanishing damping) corresponds exactly to the second zero of  $\epsilon_1(\omega)$ .

Finally, Fig. 2.5 (c) shows the simulation of the dielectric function of a typical semiconductor such as  $\pi$  conjugated hydrocarbons investigated in this thesis. The two used oscillators correspond on the one hand to excitations of weakly bonded  $\pi$  electrons and on the other hand to excitations of more strongly bonded  $\sigma$  electrons. The interband plasmon due to the  $\pi$  electrons appears, as discussed above, at higher energy than that of the  $\pi$  oscillator. Furthermore, momentum-dependent measurements of such interband plasmons provide useful informations about the dispersion of bands. That means that if the valence as well as the conduction band are flat, the energy of the transition is not changed upon changing the momentum transfer. Therefore, the plasmon shows zero dispersion in momentum transfer. The situation is different if both bands are curved and hence a non-zero dispersion (positive or negative) must appear. Low doping of such systems leads to additional transitions into unoccupied levels created in the gap. Its influence on the dielectric functions is shown in Fig. 2.5 (d).

In conclusion, the complexity of the loss function can also be seen by the fact that  $\text{Im}(-1/\epsilon(q,\omega))$  is not only a superposition of two oscillators like in  $\epsilon_2$ , i. e., two neighboring transitions are decoupled in  $\epsilon_2$  but they do interfere with each other in  $\text{Im}(-1/\epsilon(q,\omega))$  in a way that depends on the values of the parameters in the Drude-Lorentz-model.

### 2.4. Experimental Details

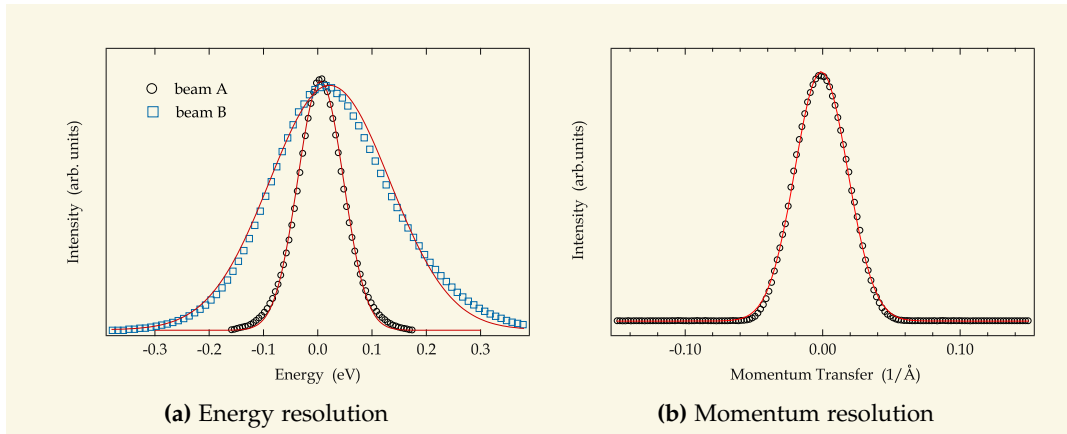
#### 2.4.1. The Spectrometer



**Figure 2.6.** | Schematic drawing of the electron energy-loss spectrometer. (1 - Source, 2 - Monochromator, 3 - Zoom lenses, 4 - Accelerator, 5 - Sample holder with cryostat, 6 - Deflection plates, 7 - Decelerator, 8 - Zoom lenses, 9 - Analyser, 10 - Multiplier, 11 - Preparation chamber, 12 - Sample magazine and Fast entry)

In Fig. 2.6 we show the main parts of the transmission electron energy-loss spectrometer. The electron source consists of a tungsten cathode followed by a lens system that focuses the electron beam on the entrance of the monochromator. Afterwards, the electron beam is guided by so called zoom lenses to the accelerator that increases the energy of the electrons to a value of  $E_0 = 172$  keV. After passing through the sample, momentum selection of the scattered particles is achieved by two pairs of deflection plates, arranged horizontally and vertically, forcing the scattered electrons back on the optical axis. After being decelerated, the electrons reach the analyzer and finally the detector, where a photo multiplier produces the signal transferred to the computer.

For an optimal investigation of the distinct types of electronic excitations—valence- as well as core-level excitations—different beam characteristics are possible. The settings required for a certain beam are stored in files containing all necessary adjustments for



**Figure 2.7.** | The energy- and momentum resolution curves for the pure electron beam (without sample). The data (black circles - beam A used for investigation of valence band excitations; blue diamonds - beam B used for investigations of core-level excitations) fitted to Gaussians (red solid line). The obtained FWHM values are  $\Delta E_{\text{beam A}} \approx 85$  meV and accordingly  $\Delta E_{\text{beam B}} \approx 200$  meV as well as  $\Delta q \approx 0.03 \text{ \AA}^{-1}$  (notice that the momentum resolution for both beams is equal).

the power supplies, deflection plates and so on. Nevertheless, each beam is tuned by a automatic procedure before a new sample is loaded for best possible performance. The characteristic data (energy and momentum resolution) for the two electron beams used throughout this thesis are plotted in Fig. 2.7. They are fitted with Gaussians according to

$$I(q) \propto \frac{1}{\sigma_q} \cdot \exp \left[ - \left( \frac{q}{\sigma_q} \right)^2 \right]$$

$$I(E) \propto \frac{1}{\sigma_E} \cdot \exp \left[ - \left( \frac{E}{\sigma_E} \right)^2 \right],$$

with the widths  $\sigma_q$  and  $\sigma_E$ . The energy and momentum resolution were chosen to be 85 meV and  $0.03 \text{ \AA}^{-1}$  for valence band excitation and 200 meV and  $0.03 \text{ \AA}^{-1}$  for core-level excitations, respectively (cf. Fig. 2.7).

#### 2.4.2. Sample Preparation

One of the major problems in the application of EELS to solid-state physics and material science is the preparation of the samples. From Fig. 2.6 it is obvious that the experiments are performed in a transmission geometry. Therefore samples with a thickness of only about 100 nm are needed and built up the main criterion whether or not a system can be investigated by EELS. There exist several possibilities to obtain the required thickness of the films depending on the microscopic structure of the actual compound. On the one

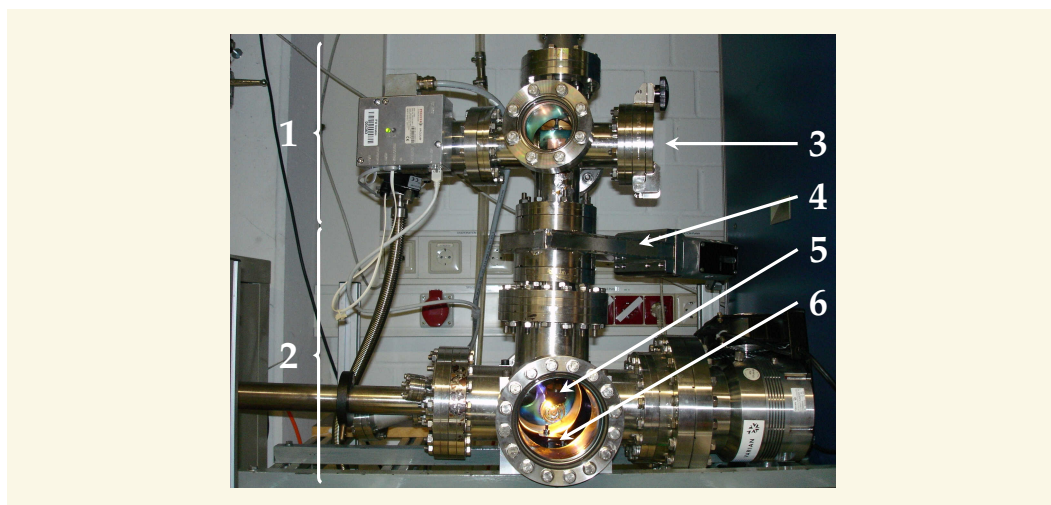


**Figure 2.8.** | The pentacene (left) as well as tetracene (right) crystals as obtained by sublimation from the gas phase.

hand thin films of single crystals can be prepared either by cutting thin slices from a macroscopic single crystal with the help of an ultramicrotome—a special device allowing precise cuts with the help of a diamond knife—or cleaving repeatedly with the help of adhesive tape, which is dissolved in organic solvents afterwards.

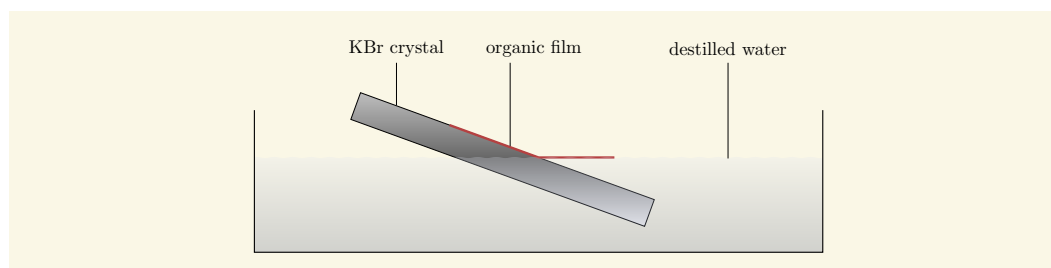
Previous to the thin film preparation single crystals of very good quality have to be grown by sublimation from the gas phase. In detail, the pentacene crystals used throughout this thesis were synthesized by Helmuth Berger from the EPFL in Lausanne via a directional sublimation of two or three times purified pentacene. The crystal growth was carried out at temperatures between 220 °C and 280 °C in closed, evacuated pyrex ampoules and a horizontal two-zone furnace was used. The growth procedure lasted about four to six weeks. The typical dimensions of the crystals are (4...10) mm × (1...3) mm × (0.05...0.25) mm. In case of tetracene, single crystals were synthesized via physical transport in an inert gas stream (argon and hydrogen mixture) in the IFW Dresden, whereas the sublimation occurred at about 300 °C in the hot zone of the furnace and the tetracene single crystals were grown at a temperature of about 150-200 °C. To obtain well defined and large crystals (dimension of 10 mm × 7 mm × 0.1 mm) the crystal growth lasted between one and six hours. An impression of their optical appearance is provided by Fig. 2.8. The chrysene and picene single crystals were prepared via physical vapor growth in a vertical geometry. Chrysene as well as picene were sublimed from a glass surface and the crystal growth occurred on a Al foil on top. The growth lasted 12 hours and resulted in very thin, singly-crystalline platelets with typical dimensions of about 0.5 mm × 0.5 mm × 100 nm.

For the present work also large thin films of organic compounds have been produced by thermal evaporation under high vacuum onto single crystalline substrates (e. g. KBr) kept at room temperature in a separate vacuum chamber as one can see in Fig. 2.9. In detail, the whole evaporation system consists of two main parts: the prechamber and the evaporation chamber. Via a fast entry and the prechamber one has the possibility to transfer the KBr substrate (with a dimension of 5 mm × 20 mm × 30 mm) into or out of the vacuum system without destroying the pressure in the main evaporation chamber. The



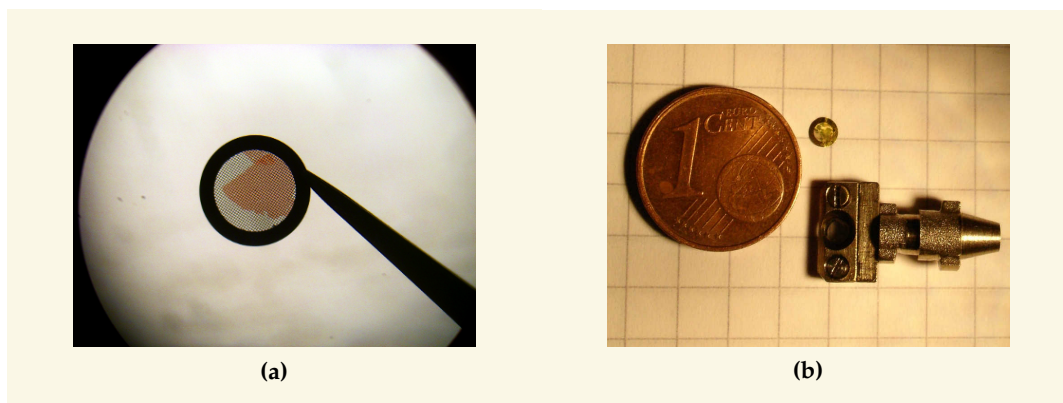
**Figure 2.9.** | UHV chamber which was used for the thermal evaporation of the organic thin films. In detail: 1 - Prechamber, 2 - Evaporation chamber, 3 - Fast entry for the transfer of the KBr-crystal into/out of the vacuum system, 4 - Valve between upper and lower chamber, 5 - Quartz crystal microbalance for an *in situ* measurement of the film thickness, 6 - Oven used for thermal evaporation.

different organic powders<sup>†</sup> were filled into a small tube made of ceramic and installed in an oven, which one can find at the bottom of the evaporation chamber. Finally, the oven is heated up slowly until the sublimation temperature of the organic powder is reached and the evaporation starts. During the vacuum deposition the film thickness can be monitored *in situ* via a quartz crystal microbalance, which is fixed directly on top of the oven. With that technique we are able to influence the crystal growth and thus the crystal orientations by controlling the deposition rate, evaporation temperature and film thickness.



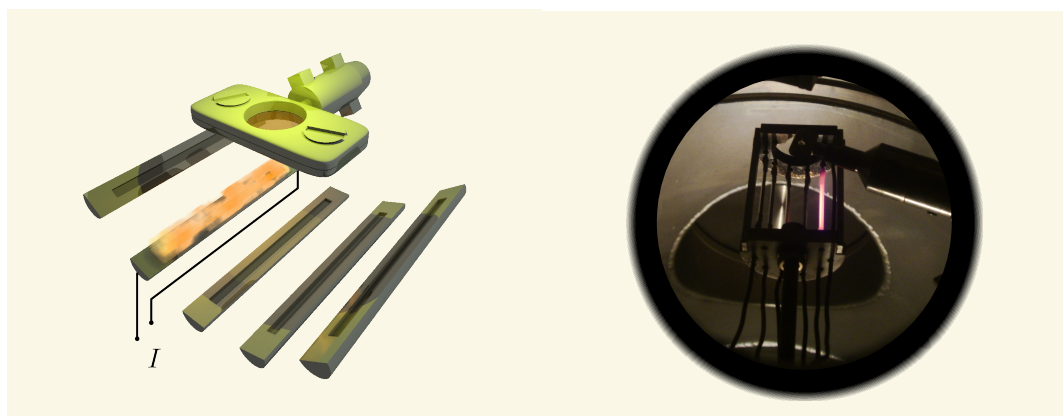
**Figure 2.10.** | Simplified view of the preparation process of the thin films for the investigation using the EELS spectrometer. The evaporated potassium bromide (KBr) crystal is floated off in distilled water until the organic thin film is replaced from the substrate. Afterwards, small pieces of the film can be mounted onto standard TEM grids and transferred into the spectrometer.

<sup>†</sup>The organic powders were bought by Sigma-Aldrich Chemie GmbH (in case of picene, chrysene, coronene, tetracene, and pentacene) as well as BGB Analytik Vertrieb GmbH (in case of 1,2;8,9-dibenzopentacene).



**Figure 2.11.** | (a) A typical snapshot of a thin film placed on a standard TEM grid (diameter of  $\approx 5$  mm) intended for usage in the EELS spectrometer. The image shows a 1,2;8,9-dibenzopentacene sample prepared by thermal evaporation under high vacuum onto a single-crystalline KBr substrate followed by removing it from the substrate in distilled water. (b) Comparison between a one Cent coin, a used TEM grid and the whole sample holder to get a better idea of the dimension of the samples under investigation.

Subsequent to the evaporation the films have to be separated from the KBr substrate. For that purpose the films are floated off in distilled water until the organic thin film is detached from the substrate and floats at the surface of the water due to the surface tension (cf. Fig. 2.10). Afterwards, small pieces of the film are mounted onto standard electron microscopy grids (see Fig. 2.11 (a)), incorporated into an EELS sample holder (see Fig. 2.11 (b)), and transferred into the spectrometer.



**Figure 2.12.** | Left panel: Schematic drawing of a sample holder and the *in situ* doping with alkali metals evaporated from commercial getter sources. Right panel: Snapshot of the construction how it looks like in reality. At the bottom of the picture one can see the holder for the getter sources (notice that the fifth getter is in an operating state). Furthermore, one can identify the transfer rod with a sample holder on top as well as the oven in the upper part of the picture.

In addition, we are able to intercalate the samples with alkali metals (e. g., potassium) in the preparation chamber of the EELS spectrometer. In detail, the sample is moved to the preparation chamber (base pressure lower than  $10^{-10}$  mbar) and exposed directly over alkali metal getter sources<sup>‡</sup> (distance between getter source and sample is about 30 mm). The getters were heated up due to their resistivity by applying a specific current, where the alkali metal was released and started to evaporate (cf. Fig. 2.12). The doping level can be influenced by changing the exposure time as well as the current through the potassium getters. Furthermore, we can heat the sample both during the intercalation process and afterwards up to several hundred degrees centigrade to control the diffusion of the alkali metal into/within the sample to achieve homogeneously doped films as well as to evaporate alkali metal atoms from the sample which are accumulated on the surface.



---

<sup>‡</sup>SAES GETTER S.p.A Viale Italia 77, 20020 Laina, Italien



*“They are ill discoverers that think  
there is no land, when they can see  
nothing but sea.”*

Sir Francis Bacon\*

# 3

## Polycyclic Aromatic Hydrocarbon Systems And Their Properties

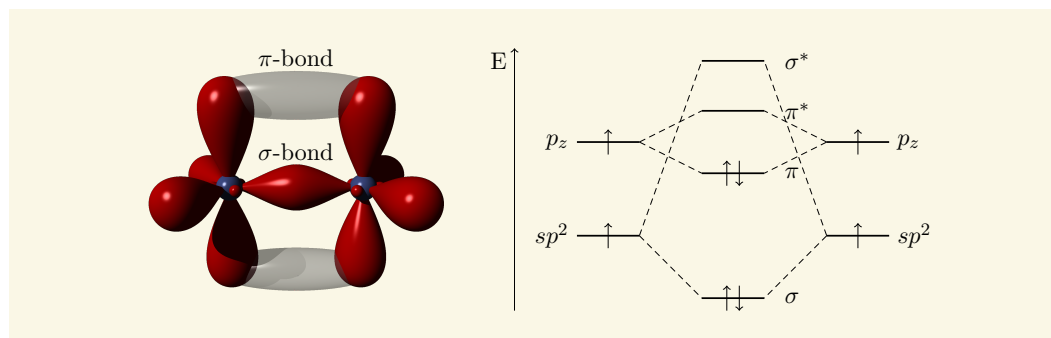
### 3.1. Introduction

**A**LL compounds investigated in the present thesis belong to the huge family of molecular crystals—in particular to the class of aromatic hydrocarbons—which only consist of fused aromatic rings and do not contain heteroatoms or carry substituents [29]. In recent years the investigation of the physical properties of organic solids has attained greatly increased importance. The wide variety of these compounds, the advantages of the relatively low cost and the possibility to modify them using the methods of synthetic organic chemistry in a practically unlimited fashion have aroused high expectations for the development of new materials. In particular their potential application in organic electronic devices has motivated many investigations in the past. These have been exploited in organic field effect transistors in view of fundamental as well as applied aspects [30–35]. Moreover, organic semiconductors are also of interest for manufacturing of organic photovoltaic cells [36–38], organic light emitting diodes [39–41] or organic spintronics [42–44].

However, within this class of materials, almost every ground state can be realized at will, spanning from insulators to semiconductors, metals, superconductors or magnets. Due to their relatively open crystal structure their electronic properties can be easily tuned by the addition of electron acceptors and donors. In some cases, this results in intriguing and unexpected physical properties. A prominent example for the latter is the formation of metallic, superconducting or insulating phases in the alkali metal doped fullerenes depending on their stoichiometry [5, 10, 45, 46]. More recently, further interesting phenomena were observed in alkali metal doped molecular materials such as the observation of an insulator-metal-insulator transition in alkali doped phthalocyanines [47], a transition from a Luttinger to a Fermi liquid in potassium doped carbon nanotubes [48], the formation of a Mott state in potassium intercalated pentacene [49], or a potassium induced phase

---

\*Sir Francis Bacon (1561-1626). English philosopher, statesman, scientist, jurist and author.



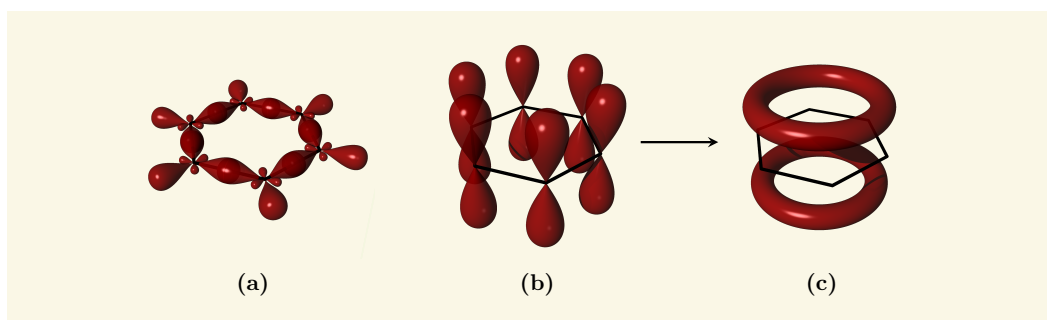
**Figure 3.1.** | Left panel: Spatial distribution of the  $\sigma$ -type molecular orbitals formed with two  $sp^2$ -hybrid atomic orbitals as well as the  $\pi$ -type orbitals formed from the  $p_z$  atomic orbital. Right panel: Schematic energy diagram for the formation of a double bond between two carbon atoms. Both atomic orbitals, the  $sp^2$  as well as the  $p_z$ , are occupied by one electron. The splitting into bonding and antibonding orbitals depends on the strength of the overlap of the atomic orbitals.

transition in iron phthalocyanine thin films [50]. Also theoretical considerations lead to fascinating predictions such as the formation of strongly correlated metals in the family of electron doped phthalocyanines [51].

Current interest focuses in particular on solids composed of organic molecules which contain conjugated systems of  $\pi$  electrons. The electron configuration of a free carbon atom in its ground state is  $1s^2 2s^2 2p^2$ . An unusual property of the carbon atom is that, among other configurations, a so-called double bond between two carbon atoms can be formed due to a  $sp^2$ -hybridisation, which describes the deformation of the atomic orbitals by the interaction between the atoms of a molecule. The result are three degenerate orbitals out of one  $s$  and two  $p$  orbitals, which are coplanar and oriented at  $120^\circ$  relative to one another. Chemical bonds formed by formation of an orbital overlap of two  $sp^2$ -orbitals are called  $\sigma$  bonds and are localised between the bonding C atoms (see Fig. 3.1 left panel). The energy difference between the occupied binding orbitals ( $\sigma$ ) and the unoccupied anti-binding orbitals ( $\sigma^*$ ) is quite large and well beyond the visible spectral range. The fourth orbital,  $p_z$ , remains unchanged and is directed perpendicular to the plane of the  $sp^2$  orbitals, and thus to the plane of the C atoms. The overlap of neighbouring  $p_z$  orbitals leads to an additional bond, the so called  $\pi$  bond, and as a consequence to a delocalised density of electrons above and below the plane of the molecule. Because of the smaller overlap of the  $p_z$  orbitals compared to the  $sp^2$  orbitals the energy splitting between bonding ( $\pi$ ) and antibonding ( $\pi^*$ ) is much weaker and leads to semiconducting properties (cf. Fig. 3.1).

If carbon atoms form larger molecules, typically with benzene rings as the basic unit, the  $\pi$ -bonds become delocalized and form a  $\pi$ -system which often has the extensions of the molecule. In case of a single benzene ring (see Fig. 3.2), which can be seen as the building block of all compounds investigated in this thesis, there are one valence electron per C atom left over in the  $p_z$  orbital, altogether six electrons that are not involved in the  $sp^2$  hybridisation. The total electronic wave function for these  $p_z$  electrons can be described

### 3.2. Features Of Aromatic Hydrocarbon Molecules



**Figure 3.2.** | The benzene molecule  $C_6H_6$ . (a)  $\sigma$ -type molecular orbitals formed with  $sp^2$ -hybrid atomic orbitals from the carbon atoms, (b)  $\pi$ -type orbitals and (c) delocalized  $\pi$ -system resulting from two indistinguishable  $\pi$ -orbital configurations.

as a linear combination of the  $p_z$  orbitals of the six C atoms. This linear combination spreads the wave function over all C atoms in the benzene hexagon. Thus, there are not enough electrons to form double bonds on all the carbon atoms, but the “extra” electrons strengthen all bonds on the ring equally and contribute to the stability of the planar structure. The resulting molecular orbital has  $\pi$  character. The gap between occupied and empty states in these  $\pi$ -systems becomes smaller with increasing delocalization, leading to absorption and fluorescence in or near the visible spectral range.<sup>§</sup>

### 3.2. Features Of Aromatic Hydrocarbon Molecules

All compounds which are under investigation in this thesis are hydrocarbon molecules with structures that include fused benzene rings, which are also responsible for the electronic properties. The arrangement of the benzene rings represents the main and obvious difference especially in the two main classes of aromatic hydrocarbon molecules (cf. Tab. 3.1). In one-dimensional extended linear hydrocarbons,  $[n]$ acene (such as tetracene and pentacene) consists of a linear fusion of  $n$  benzene rings, while  $[n]$ phenacene (such as chrysene and picene) are built up of benzene rings in a zigzag or armchair manner.  $[n]$ phenacene molecules have a lower reactivity than  $[n]$ acene and show high stability even

<sup>§</sup>In a simple model, electrons that have equal probabilities to be found anywhere along an interval  $l$  (in case of a single benzene ring  $l$  is the circumference of the hexagon) can be treated like electrons in a potential box. The discrete energy levels are defined by

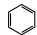
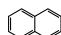
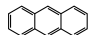
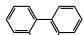
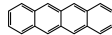
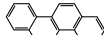
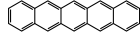
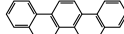
$$E_n = \frac{n^2 h^2}{2m_e l^2} \quad n = 1, 2, 3, \dots$$

Transition between the energy level  $n = 1$  and  $n = 2$  have the energy

$$h\nu = \Delta = \frac{h^2(2n+1)}{2m_e l^2}.$$

With the typical C–C distance in benzene of about 140 pm this crude model results in absorption bands around  $\lambda = 200$  nm for a excitation of the  $\pi$  electrons of benzene, which agrees fairly well with the observed absorption wavelength [52].

**Table 3.1.** | The first representatives of the class of [*n*]acene (consists of a linear fusion of *n* benzene rings) and [*n*]phenacene (consists of a zigzag fusion of *n* benzene rings) and their structural as well as chemical formula (*n* indicates the number of benzene rings and the rule for the chemical formula is  $C_{4n+2}H_{2n+4}$ ).

<i>n</i>	Acene	Phenacene	Formula
1	Benzene 		$C_6H_6$
2	Naphthalene 		$C_{10}H_8$
3	Anthracene 	Phenanthrene 	$C_{14}H_{10}$
4	Tetracene 	Chrysene 	$C_{18}H_{12}$
5	Pentacene 	Picene 	$C_{22}H_{14}$

against  $O_2$  and  $H_2O$ . This argument can be supported on the one hand experimentally by the synthesis of longer molecules in case of the phenacenes ([11]phenacene has been synthesized [53], while [9]acene has been the largest acene obtained up to date [54]) and on the other hand by theoretical elaborations [55].

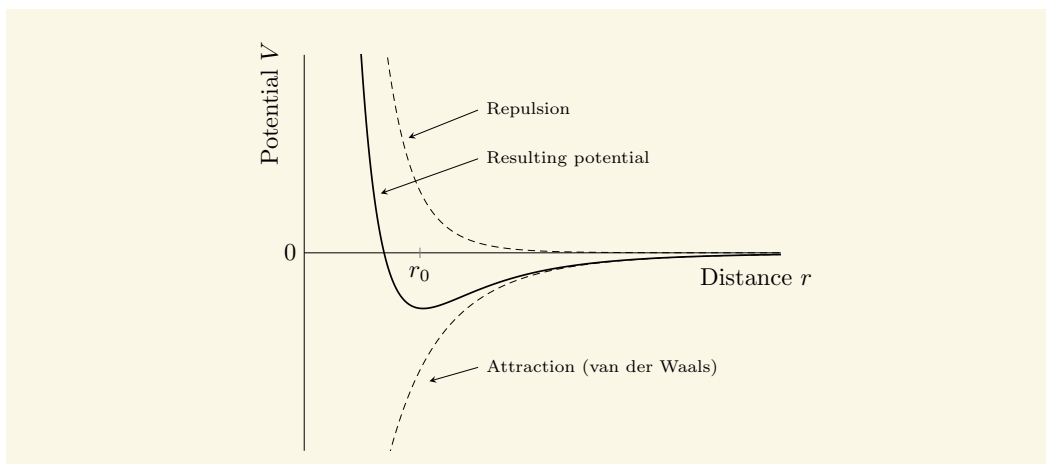
Phenacenes such as picene have attracted less attention than acenes, such as pentacene, for the use in organic electronic devices, because only a few efficient synthetic methods are currently available for [*n*]phenacenes, which also results in a much higher price for such materials. Another very important fact, which one has to have in mind during the work with the phenacene systems is that a huge number of them are suspected to be carcinogenic, teratogenic and mutagenic [56, 57].

Before discussing the crystal structure in detail, the question arises how a large number of those hydrocarbon molecules assembles to form a solid. From a quantum-mechanical point of view this is of course due to the interaction of the above mentioned  $\pi$ -electron system which can be understood at a rather phenomenological level by the Lennard-Jones-potential [58, 59]

$$V(r) = \frac{a}{r^{12}} - \frac{b}{r^6},$$

where *r* indicates the distance between two neighboring constituents. The constants *a* and *b* depend on the kind of interacting atoms and are closely related to the range of interaction. Therein the attractive  $1/r^6$  part arises from induced dipole-dipole interactions between the molecules situated at different lattice sites and the repulsive  $1/r^{12}$  contribution, coming from the inner electrons and the atomic nuclei, boils down to Pauli's exclusion principle, hindering the molecules from getting too close to each other. This effect becomes important only at very small distances and increases very rapidly with further decreasing distance. The superposition of the repulsion and the attraction yields the equilibrium distance  $r_0$  between the molecules, as one can see in Fig. 3.3. The reason for this type of bond formation is the closed shell structure of the molecular units in molecular solids. In

## 3.2. Features Of Aromatic Hydrocarbon Molecules



**Figure 3.3.** | The repulsive potential combined with the van der Waals attraction gives the overall, resulting potential (Lennard-Jones potential). The interaction energy has its minimum at the equilibrium distance  $r_0$ .

general the dipole-dipole mediated interactions are weaker than the covalent bonds in a 'normal' solid and therefore the electronic properties of a molecular solid are often very similar to those of the individual molecular building blocks.

As an alternative to the Lennard-Jones-potential, one can also carry out calculations using an exponential repulsive potential which leads to the so called Buckingham potential [60] given by

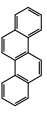
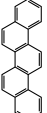
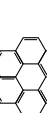
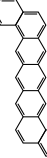

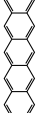
$$V(r) = C \cdot e^{-\alpha r} - \frac{b}{r^6}.$$

### 3.2.1. Crystal Structure Of Nonpolar Molecules

In a crystal of nonpolar molecules with relatively weak dispersive forces and strong short-range repulsion, one can assume that the molecules within the crystal will attempt to pack in a manner where they reach the densest possible packing with the least possible repulsion. The arrangement of the molecules will be determined by atom-atom potentials. Therefore, the lattice energy is minimized when the number of van der Waals atom-atom contacts is as large as possible. A useful parameter for judging the efficiency of a molecule for using space in a solid state arrangement is the packing coefficient  $K$  introduced by Kitaigorodskii [75]. The values of  $K$  for aromatic hydrocarbons lie between 0.68 (benzene) and 0.80 (perylene) [76] (For a comparison: the packing coefficient of ice, which is bound through dipolar forces and hydrogen bonding, is about 0.38 [77]).

Planar hydrocarbon molecules crystallize in a layered structure in which the molecular packing in each layer is affected by two important intermolecular interactions: C—H interactions between adjacent molecules, and the C—C interactions between molecules in neighboring layers. There are different packing forms possible, whereby the simplest one is

**Table 3.2.** | The crystallographic data of all aromatic hydrocarbons investigated in this thesis.  $V$  indicates the volume of one unit cell and  $Z$  describes the number of molecules in the unit cell.

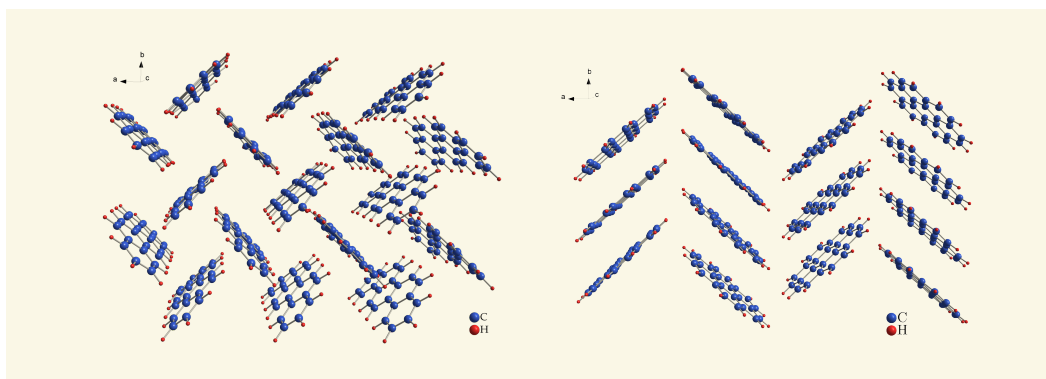
						
	Chrysene $C_{18}H_{12}$	Picene $C_{22}H_{14}$	Coronene <sup>a</sup> $C_{24}H_{18}$	1,2,8,9-dibenzopentacene <sup>b</sup> $C_{30}H_{18}$	Tetracene $C_{18}H_{12}$	Pentacene $C_{22}H_{14}$
crystal structure	monoclinic	monoclinic	monoclinic	-	triclinic	triclinic
space group	I2/c	P2 <sub>1</sub>	P2 <sub>1</sub> / <i>a</i>	-	P $\bar{1}$	P $\bar{1}$
$a/\text{Å}$	8.386	8.480	16.094	-	6.056	6.266
$b/\text{Å}$	6.196	6.154	4.690	-	7.837	7.775
$c/\text{Å}$	25.203	13.515	10.049	-	13.010	14.530
$\alpha/^\circ$	90.0	90.0	90.0	-	77.13	76.47
$\beta/^\circ$	116.2	90.5	110.8	-	72.12	87.68
$\gamma/^\circ$	90.0	90.0	90.0	-	85.79	84.68
$V/\text{Å}^3$	1175	705	710	-	573	685
$Z$	4	2	2	-	2	2
Reference	[66]	[67]	[68]	-	[69] <sup>c</sup>	[73, 74]

<sup>a</sup>Coronene crystals show two structural phase transitions depending on pressure and temperature in the range between 140-180 K [61, 62] and at 50 K [63].

<sup>b</sup>Up to now, no details of the crystal structures are published in literature. Only for the related compound Dibenz[*a,h*]anthracene two significantly different crystal structures are published [64, 65].

<sup>c</sup>There are also other crystal structures published in literature, which have been, and still are, under discussion. (cf. [70-72])

### 3.2. Features Of Aromatic Hydrocarbon Molecules



**Figure 3.4.** | The so-called herringbone structure using the example of picene (left panel). All aromatic hydrocarbons investigated in this thesis crystallize in this typical arrangement of the single molecules. In the right panel the crystal structure ( $\gamma$ -structure) of solid coronene is shown, where the herringbone arrangement is flattened.

the herringbone type, in which the C–H interactions between nearest-neighbor molecules dominate to produce a non-parallel arrangement [78]. All acenes as well as phenacenes belong to this group (see left panel of Fig. 3.4). When the C–C or  $\pi$ – $\pi$  interaction between out-of-plane p orbitals of neighboring molecules increases, the herringbone arrangement is flattened and the distance between the molecules in the non-parallel form increases. This is the so-called  $\gamma$ -structure, which is realised in solid coronene (cf. 3.4 right panel). Furthermore, there are two other packing forms described in literature. A further increase in the C–C interaction produces the  $\beta$ -structure (layer like structure) and finally a structure in which units of two molecules form a herringbone arrangement called the “sandwiched” herringbone structure like in pyrene [78, 79].

An overview about the crystallographic data of all investigated hydrocarbons is given in Tab. 3.2. Except for chrysene, the essential ingredient of the structures is a monoclinic (in case of picene and coronene) or triclinic (in case of tetracene and pentacene) lattice containing two non-equivalent molecules per unit cell which refers to the impossibility to reproduce molecule 2 from molecule 1 just by translations along the fundamental lattice vectors. This behavior is quite common not only for hydrocarbons [80–82] but also for other organic solids such as PTCDA [83].

In addition, the tendency to form different polymorphs, i. e., the ability of a solid material to exist in more than one form or crystal structure, is often observed in molecular solids. Depending on different process parameters such as temperature, pressure, and sample preparation, the molecular packing produces slight modifications in the crystal structure. For instance, in case of pentacene the existence of a large polymorph variety is reported several times in literature [73, 74, 84–88].

In case of investigations of single crystals or partially oriented evaporated samples one has to keep in mind, that within the EELS experiment all measurements were done in the momentum space. This fact is essential, especially by comparing EELS measurements with

other optical measurements. Employing the crystallographic data shown in Tab. 3.2 it is possible to calculate the reciprocal lattice, using the well known formulae [89]

$$\begin{aligned} \mathbf{a}^* &= 2\pi \frac{\mathbf{b} \times \mathbf{c}}{\mathbf{a} \cdot (\mathbf{b} \times \mathbf{c})} \\ \mathbf{b}^* &= 2\pi \frac{\mathbf{c} \times \mathbf{a}}{\mathbf{a} \cdot (\mathbf{b} \times \mathbf{c})} \\ \mathbf{c}^* &= 2\pi \frac{\mathbf{a} \times \mathbf{b}}{\mathbf{a} \cdot (\mathbf{b} \times \mathbf{c})}, \quad \mathbf{a}, \mathbf{b}, \mathbf{c} \in \mathbb{R} \end{aligned}$$

whereby  $\mathbf{a} \cdot (\mathbf{b} \times \mathbf{c})$  is the volume of the unit cell.

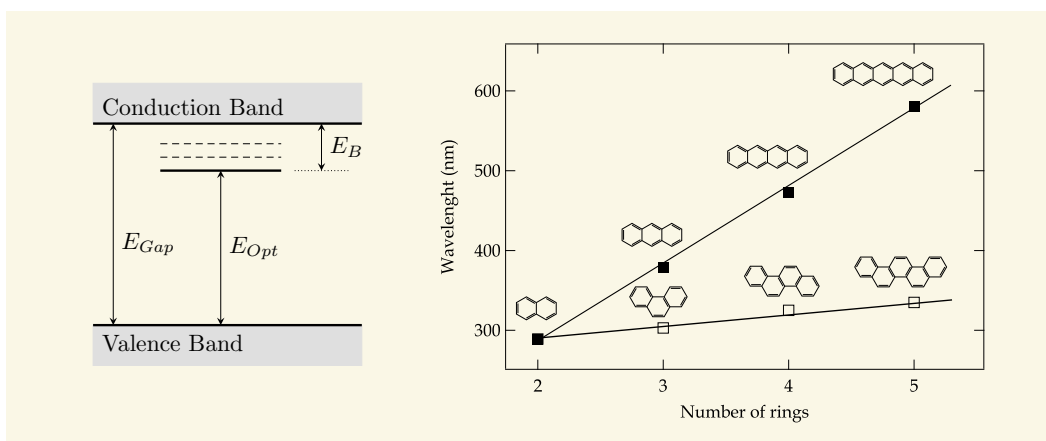
### 3.2.2. Electronic Properties: Optical Absorption And Excitons

All semiconductors are characterised by a so-called band gap, whose definition, as the energy required for creating an electronic transition, is not unique in a semiconductor. Conventionally two cases are distinguished often termed transport gap and optical gap (see Fig. 3.5 left panel) where the former one describes the energy ( $E_{Gap}$ ) required to create unbound electron hole pairs and therefore enables electrical conductivity by transferring an electron from the valence band to the conduction band. Furthermore, it is possible to create bound electron hole pairs, i. e., excitons, which are attracted to each other by the electrostatic Coulomb force and are responsible for the absorption in the energy range  $E_{Opt} \leq E \leq E_{Gap}$  [90]. In general one can conclude that the lowest electronic excitations in organic molecular solids usually are excitons due to the weak Van der Waals interaction between the molecules, which is responsible for the molecular arrangement in the crystal [91, 92].

Figure 3.5 (right panel) shows the comparison of the onset energy of the first absorption band (p-band), which originates from the energy difference between the highest occupied molecular orbital (HOMO) and the lowest unoccupied molecular orbital (LUMO), between  $[n]$ acenes and  $[n]$ phenacenes as a function of the number of benzene rings. On the one hand one can clearly identify a remarkable shift to longer wavelengths (lower energies) when the number of benzene rings increases for acenes [94, 95]. This implies that linearly annulated molecules with more benzene rings have smaller HOMO-LUMO gaps. In contrast, the first absorption band of  $[n]$ phenacenes changes only slowly with increasing the number of rings, and the HOMO-LUMO gap is located in the UV region. The remaining question—what is the origin of the differences between the two series of compounds—can be answered based on theoretical calculations [93] as well as geometrical considerations. Less delocalization in zig-zag structures in the direction parallel to the long axis leads to a more stable compound compared to the linearly annulated systems and therefore supports the stability of phenacene molecules as mentioned above [96, 97]. In case of the acenes the linear molecular structure allows a delocalization of the HOMO and LUMO over the entire molecule which leads to the different excitation offsets. Furthermore, according to Clar's sextet rule also the degree of aromaticity is most important for the characterization of the



### 3.3. Superconductivity In Carbon-Based Materials



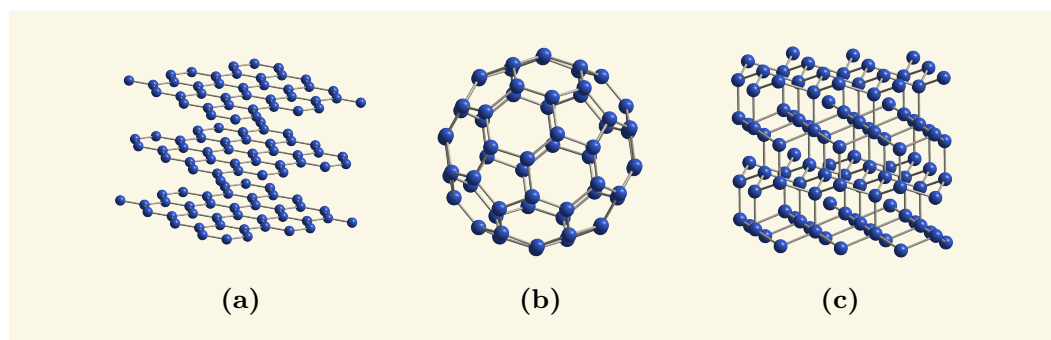
**Figure 3.5.** | Left panel: Schematic view of a semiconductor band-structure. The transport gap  $E_{Gap}$  corresponds to the energy required for a transition between valence band and conduction band whereas the optical gap  $E_{Opt}$  is needed for creating an exciton. The short lines indicate the exciton ground state (solid) and higher excitonic levels (dashed) and  $E_B$  is the binding energy of the exciton. Right panel: Onset energy in optical absorption of phenacenes and acenes depending on the length of the chain. This figure is reproduced from Ref. 93.

properties [98]. Clar proposed that the chemical reactivities and other properties could be understood best in terms of localization of the aromatic sextets present in the molecule [99]. For a more detailed discussion and additional explanations about aromaticity and Clar's sextet rule see Appendix B.

### 3.3. Superconductivity In Carbon-Based Materials

#### 3.3.1. A Short Overview

Carbon based superconductors have a long history dating back to the year 1965, when superconductivity was discovered in potassium intercalated graphite with transition temperatures of  $T_c < 1$  K [100]. Graphite (see Fig. 3.6(a)) can become superconducting when alkali-metal atoms are intercalated into the gaps between the single graphene sheets. Subsequently, the transition temperature was increased up to 5 K by changing the alkali-metal as well as synthesis parameter like pressure [101–104]. 40 years later, intercalated graphite came back into the focus of researcher due to the discovery of superconductivity in calcium doped graphite with a remarkably high  $T_c$  for a carbon based superconductor of 11.5 K [105]. Another class of organic superconductors are the charge-transfer salts where superconductivity was discovered for the first time in 1980 in the so-called Bechgaard salts (TMTSF-compounds) with a  $T_c$  around 1 K [106, 107]. This was followed by the group of the quasi two-dimensional charge transfer systems, which have as their organic basic structural unit the donor molecule bisethylenedithio-tetrathiafulvalene (BEDT-TTF) and reach a critical temperature of  $T_c = 1.5$  K at normal pressure [108]. With a moderate applied



**Figure 3.6.** | Carbon network materials: (a) graphite, (b)  $C_{60}$  and (c) diamond. (Crystal structures were plotted via Crystal Impact Diamond 3.1f using the *cif*-files based on published crystal structures in Ref. 110–112).

pressure,  $T_c$  can be increased to 8 K [109], the highest transition temperature among the organic superconductors at that time.

However, the discovery of a superconducting phase in the alkali metal doped fullerides (cf. Fig. 3.6 (b)) in 1991 represented a breakthrough in the field of superconductivity. In particular the superconducting fullerides have attracted a lot of attention, and rather high  $T_c$ 's in, e. g.,  $K_3C_{60}$  ( $T_c = 18$  K)[5],  $Cs_2RbC_{60}$  ( $T_c = 33$  K)[113] or  $Cs_3C_{60}$  ( $T_c = 38$  K) [6, 7] have been reported. In the past years, more than 20 superconducting fullerene compounds were discovered and also the highest  $T_c$  of 40 K in a carbon-based material was found in an alkali doped  $C_{60}$  ( $Cs_3C_{60}$  under 15 kbar [114]). Furthermore, it was shown that the superconducting transition temperature in alkaline-metal-doped fullerene increases with the unit-cell volume [115], which had been believed to be an evidence for the BCS mechanism<sup>||</sup> of  $C_{60}$  solid superconductivity. A fully developed theory of superconductivity in this compounds is still lacking, but it has been widely accepted that strong electronic correlations and the Jahn-Teller electron-phonon coupling [118, 119] produce local electron-pairings and the occurrence of superconductivity can be understood within the framework of the conventional BCS theory<sup>\*\*</sup>.

Finally, also the last allotrope of carbon discussed in this overview, diamond (see Fig. 3.6 (c)), which is a wide-gap semiconductor, shows superconductivity with a  $T_c$  of 4 K when carbon atoms are substituted by boron atoms [122]. Heavy boron doping leads to an increase of the transition temperature up to around 11 K in thin films grown by various chemical vapor deposition techniques [123]. Thus, one can conclude that all of the carbon networks (zero-dimensional  $C_{60}$ , two-dimensional graphite and three-dimensional diamond) can be modified in one or the other way with the result of the appearance of a superconducting phase. Interestingly, the procedures for inducing superconductivity

<sup>||</sup>Microscopic theory of superconductivity proposed by John Bardeen, Leon N. Cooper and John R. Schrieffer in the year 1957, which describes superconductivity as a effect caused by a condensation of pairs of electrons into a boson-like state [116, 117].

<sup>\*\*</sup>This represents only a short overview about this topic. For further reading one can find more informations in Ref. 10 and 120 and in the review articles by Baenitz [121] and Gunnarson [45].

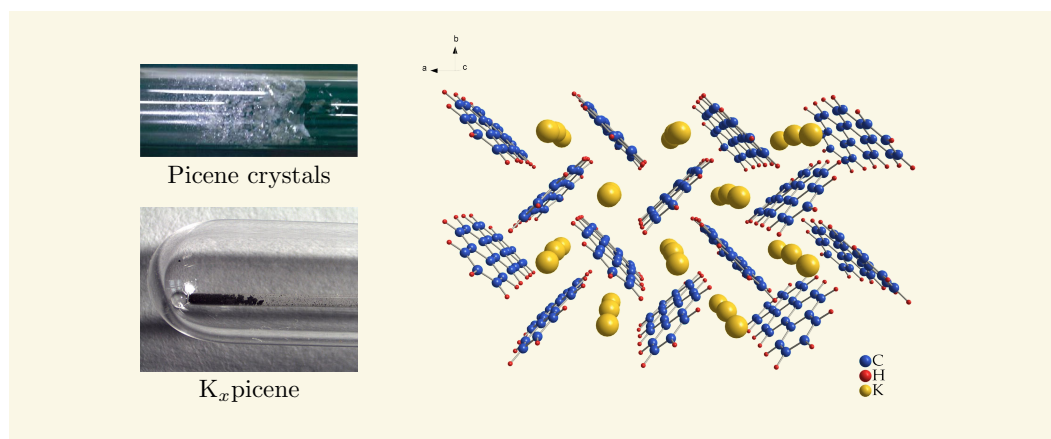
### 3.3. Superconductivity In Carbon-Based Materials

are significantly different and depend on the covalent bond form ( $sp^2$  for graphite,  $sp^3$  for diamond, and a mixture of  $sp^2$  and  $sp^3$  in case of fullerene). Superconductivity in materials with an  $sp^2$  structure is produced by intercalation of metal atoms, and in those with an  $sp^3$  character by substitution of the carbon atoms by other elements. Generally, one can determine that the observed transition temperatures in organic systems are substantially lower than those in inorganic superconductors such as cuprates (e. g.,  $\text{HgBa}_2\text{Ca}_2\text{Cu}_3\text{O}_x$  with max.  $T_c \approx 133$  K at ambient pressure [124] and a  $T_c$  up to 153 K at 150 kbar [125]) or iron-pnictides (e. g.,  $\text{SmFeAsO}_{1-x}\text{F}_x$  with a  $T_c = 55$  K [126, 127]). This fact can be understood if one considers, that the electronic band width, which gives the basic energy scale, usually is an order of magnitude smaller in the organic systems compared with inorganic materials. On the other hand, the discovery of unsuspected superconductivity of the well known magnesiumdiboride ( $\text{MgB}_2$ ) in 2001 with a  $T_c = 39$  K [128] may indicate the possibility of higher- $T_c$  superconductors still in common and known materials like carbon based materials which provide an important and rich research stage for superconductivity.

#### 3.3.2. The "New" Class Of Hydrocarbon Superconductors

In the case of organic superconductors, no new systems with high  $T_c$ 's similar to those of the fullerides have been discovered in the past decade. But in 2010, the field was renewed with the discovery of superconductivity in alkali-metal doped picene with a  $T_c$  up to 18 K by doping with potassium [129]. This discovery is the starting point for the development of a new class of aromatic hydrocarbon superconductors, comprising molecular crystals doped with alkali or alkaline earth metals. These crystals consist of polycyclic aromatic hydrocarbons, i. e., planar molecules formed by a number of juxtaposed hexagonal benzene rings. Interestingly, it is therefore more reminiscent of a small fragment of a single sheet of graphite, rather than a three-dimensional  $\text{C}_{60}$  molecule. This planarity is imposed on picene by the overlap of  $\pi$ -electrons throughout the molecule.

Pristine solid picene (see Sec. 3.2.1 and Tab. 3.2 for details of the crystal structure) is a semiconductor with a transport gap of about 4 eV [130, 131] and a white colour (cf. 3.7). Mitsuhashi *et al.* made their superconducting samples by reacting alkali-metal vapour with solid picene. In detail, the alkali metals were intercalated into crystals of picene by annealing nominal compositions of picene and alkali metals in glass tubes at 440 K and an initial pressure of  $1 \cdot 10^{-6}$  mbar for several days (7-21 days). After this procedure a significant color change to black was observed, which was also the case in our experiments. Because of the weak interactions between the single molecules in a picene crystal, it is possible for the alkali-metal atoms to enter the lattice by increasing the spacing between the molecules. The exact positions of the alkali metal atoms are still undetermined experimentally but within the framework of density functional theory calculations a prediction of a plausible crystalline structure for doped picene has been released in some publications [132–134] with the result that the potassium atoms (and also the other alkali metal atoms) are arranged in the intralayer region as shown in the right panel of Fig. 3.7. Figure 3.8 shows the magnetization  $M$  (expressed as  $M/H$ , where  $H$  is the applied magnetic field (here 20 Oe)) as a function of temperature  $T$  for  $\text{K}_{3,3}\text{picene}$  for zero field (ZFC)



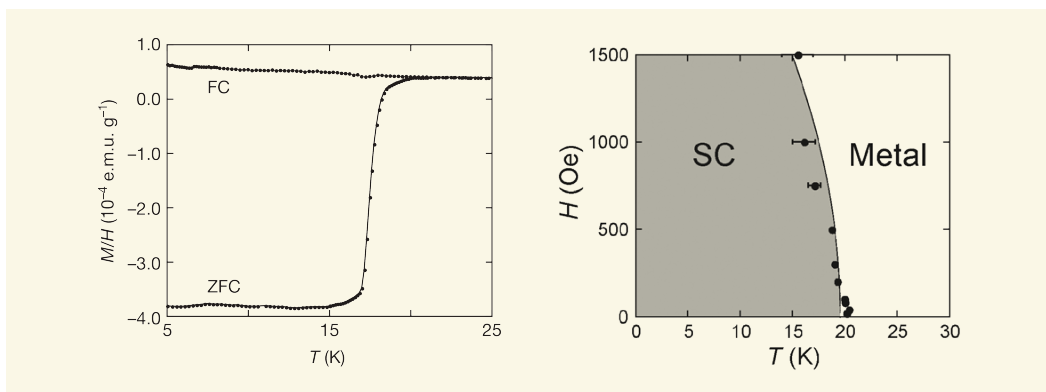
**Figure 3.7.** | Left panel: Physical appearance and colour of pristine picene and potassium doped picene. (Photos are taken from [129, 135]) Right panel: Crystal structure after doping, here especially the case of  $K_3$ picene. This figure is based on a crystal structure of potassium-doped picene with an exact stoichiometry of  $K_3$ picene theoretically determined within density functional theory by de Andres *et al.* [133].

and field cooling (FC) measurements. As one can see from the plot, the magnetization decreases below 20 K and from the inflection point of the spectra a transition temperature of 18 K was determined. Furthermore, also doped samples with different compositions of potassium were prepared. The results can be summarised as follows: a temperature-independent behaviour of the susceptibility is observed for  $x \leq 2.5$ , which indicates Pauli paramagnetism. At  $2.6 \leq x \leq 3.3$  the susceptibility drops suddenly at 7 or 18 K (depending on the preparation process) with decreasing temperature and finally above an  $x$ -value of 3.3 a Curie-like behaviour is observed. Notice that in this thesis the  $x$ -values represent the nominal mole ratios, e. g., a sample with a molar ratio of 3:1 for potassium and picene is represented as  $K_3$ picene. Additionally, measurements of the susceptibility at different magnetic fields show that the superconducting phase is not completely destroyed by the application of weak  $H$ , as one can see in the superconducting phase diagram in Fig. 3.8, showing that  $K_{3.3}$ picene is a type-II superconductor with a lower critical magnetic field  $H_{c1}$  of 380 Oe.

In the end, the group of Mitsuhashi and co-workers presented in their publication also results of rubidium (Rb) and calcium (Ca) intercalated picene, and showed that at a nominal compositions of  $Rb_{3.1}$ picene as well as  $Ca_{1.5}$ picene a superconducting phase transition at 7 K can be observed. This supports the idea that a three electron transfer to each picene molecule can lead to superconductivity.

After this unexpected discoveries in intercalated picene crystals superconductivity was also reported in other alkali-metal-intercalated polycyclic aromatic hydrocarbons. First of all Wang *et al.* observed superconductivity with  $T_c = 5$  K in potassium and rubidium doped phenanthrene ( $A_3$ phenanthrene, where A can be either K or Rb) [136]. Furthermore, also in strontium (Sr) and barium (Ba) doped phenanthrene a superconducting phase

### 3.3. Superconductivity In Carbon-Based Materials



**Figure 3.8.** | Left panel: Magnetization  $M$  (expressed as  $M/H$ , where  $H$  is the applied magnetic field) as a function of temperature  $T$ , for  $K_{3,3}$ picene for zero field cooling (ZFC) and field cooling (FC) measurements. From the inflection point of the plots, the  $T_c$  was determined to be 18 K. Right panel: Superconducting phase diagram for the 18 K superconductor determined from the  $M/H$  versus  $T$  plots. SC denotes the superconducting phase. Images were taken from Ref. 129.

was observed with a critical temperature of  $T_c = 5.6$  K and 5.4 K for  $Sr_{1.5}$ phenanthrene and  $Ba_{1.5}$ phenanthrene, respectively [137]. At the end, the successful syntheses of La- and Sm-doped phenanthrene powder samples and the discovered superconductivity at  $T_c$  around 6 K in them are reported [138].

Subsequently, these observations are followed by the discovery of a superconducting transition in  $K_3$ coronene at a  $T_c$  of 15 K [139], whereas the coronene molecule is made out of six benzene rings which are arranged in a circle as depicted in Tab.3.2. (In contrast to the other materials under investigation coronene belongs to the group of circulenes [140] which are closed rings consisting of benzenes. Other members of this group are e.g. corannulene [141] or kekulene [142, 143].) The superconducting coronene samples were produced by a long-time annealing procedure of coronene crystals and potassium at 570 K related to which was reported in case of picene. Additionally, for potassium contents  $x \leq 2.5$  the samples show Pauli-like paramagnetism, which indicates metallic behaviour.

Most recently, Xue *et al.* reported the observation of superconductivity at 33 K in K-doped 1,2:8,9-dibenzopentacene [144], which is higher than any  $T_c$  reported previously in any other organic superconductor besides the alkali-metal doped  $C_{60}$ . Dibenzopentacene is a molecule formed by seven benzene rings as depicted in Tab.3.2. It looks like a pentacene molecule with one snapped off benzene ring on both ends. Unfortunately, up to now, no details of the crystal structure are published. The samples were prepared in a similar way as the picene superconductors by direct heating of potassium metal with dibenzopentacene in an evacuated tube at 570-620 K for 7-20 days. To improve the homogeneity of the products, a second post-annealing procedure sometimes was performed. All obtained products are uniformly dark black in color, which is totally different compared with the orange/red color of pure dibenzopentacene. Superconductivity was observed for the samples with compositions of  $K_x$ dibenzopentacene with  $3 \leq x \leq 3.5$ .

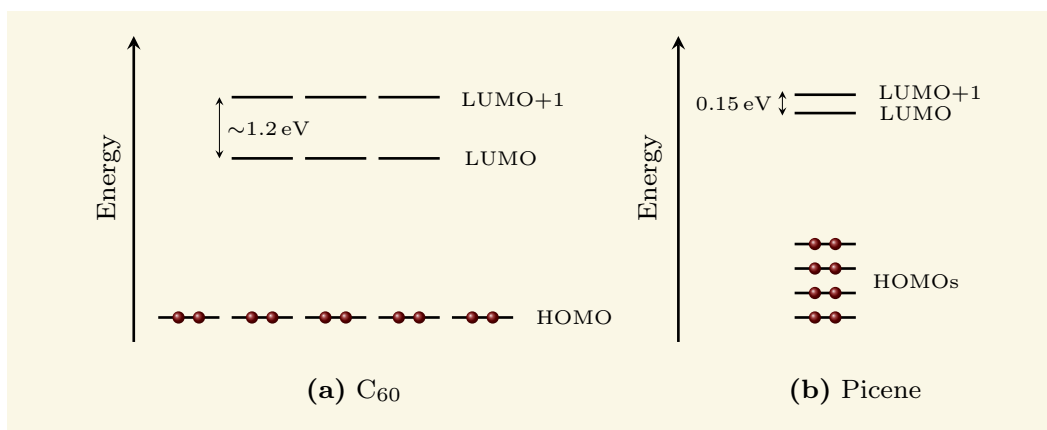
All these experimental observations and the increased attention on this class of materials ask for theoretical consideration which are necessary to get an idea for the explanation of superconductivity and further to clarify what makes this hydrocarbon superconductors so special compared to similar organic semiconductors, e. g., the difference between picene and pentacene. A first-principle electronic structure calculation was performed by Kosugi *et al.* in the density functional theory (DFT) with the local-density approximation (LDA) for both pristine and doped solid picene [132, 145]. To understand solid aromatic molecules, such as picene, compared to other families of  $\pi$ -electron-based superconductors, it is important to consider the nature of the orbitals accepting the electrons introduced by intercalation—with other words—the main character of the conduction band. First of all a comparison with  $C_{60}$  is very instructive. The highly symmetrical nature of  $C_{60}$  makes the electron-accepting orbital triply degenerate (three orbitals with the same energy). In picene, degeneracy is impossible at first view because the symmetry of the molecule is too low. Therefore, it is very surprising that Kosugi and colleagues' calculations show that the conduction band comprises four bands very close in energy suggesting a high density of states mainly derived from the LUMO and LUMO+1 (see Fig. 3.9). This, as a consequence, creates an accidental or pseudo degeneracy. It may can be seen as a possible link to the electronic structure of the fullerides. This results were moreover verified by additional calculations by Rubio and co-workers [130].

The existence of low-lying, unoccupied  $\pi$ -electronic states in picene allows the molecule to accept electrons from the alkali metals, thus generating the charge carriers required for superconductivity. This is quite the same mechanism of charge-carrier generation as is found in the metal-doped graphite and  $C_{60}$  compounds as described in the previous section. Obviously, the number of metal atoms per picene molecule controls the number of electrons donated to the hydrocarbon, and thus determines how many electrons fill the lowest-energy orbitals to become possible charge carriers. Taking into account the electronic structure of picene, it seems reasonable that, up to four electrons could be accepted by the molecule's empty orbitals, which are pseudo-degenerate and lowest in energy. If three electrons are transferred from three K atoms to picene in  $K_3$ picene, the LUMO+1 level is half occupied. In most theories of superconductivity the density of states at the Fermi level sensitively controls  $T_c$ . The expected weak overlap between the outer orbitals of the molecules in the picene materials should lead to a high density of electronic states at the Fermi level, which might in part explain why the observed transition temperatures are relatively high.

Motivated by the first theoretical calculations and the innovative experimental results further publications, both theoretical [134, 147–155] and experimental [156–158], about picene und additional about phenanthrene [159–163] were released.

With the discovery of superconductivity in solid coronene upon potassium doping, calculations of the electronic structure for this compound are necessary for a fundamental understanding of the mechanism behind the superconductivity in this new class of aromatic superconductors, and further to answer the question whether other aromatic compounds can become superconducting as well. Interestingly, recent *ab initio* calculations show that

### 3.3. Superconductivity In Carbon-Based Materials



**Figure 3.9.** | Comparison of the highest occupied molecular orbitals (HOMOs) and the lowest unoccupied molecular orbitals (LUMOs) of picene and fullerene, where the red balls represent electrons. (a) The LUMO of C<sub>60</sub> is triply degenerate: it consists of three orbitals of equal energy. Doping with alkali-metals donate electrons to the molecule's LUMO, and generate as a consequence the necessary charge carriers for metallic conduction. (b) In picene, LUMO and LUMO+1 (the second lowest unoccupied molecular orbital) are almost equivalent in energy, creating a pseudo-degeneracy. Superconducting charge carriers are also generated in picene by accepting electrons from alkali-metals intercalated into the system. The degeneracy (or pseudo degeneracy) of the LUMOs in both compounds is crucial for generating a high density of electronic states at the Fermi level of these solids, which influences the transition temperature. Scheme is reproduced from Ref. 146.

even in the case of undoped solid coronene the conduction band, with a width of 0.4 eV, comprises four bands, which basically originate from the two LUMOs [164]. Reflecting the higher symmetry of a coronene molecule compared to picene the four bands are doubly-degenerated. For potassium doped coronene the problem of the missing experimental knowledge about the crystal structure remains. Anyway, Kosugi *et al.* calculated—within a theoretical structure optimization of K<sub>3</sub>coronene—the electronic band structure which is significantly more dispersive than the undoped one, where the LUMO-derived band group is fused with the upper band group, resulting in a much wider band group. In the end, the reported Fermi surface consists of multiple sheets, as in doped picene but with the different topology of the surface.







*“Man hat nur Bausteine, kein Gebäude, so lange man nicht die verwickelten Erscheinungen einem Prinzip unterwürfig gemacht hat.”*

Carl Friedrich Gauß\*

# 4

## Results Part I: EELS On Pristine Aromatic Hydrocarbon Systems

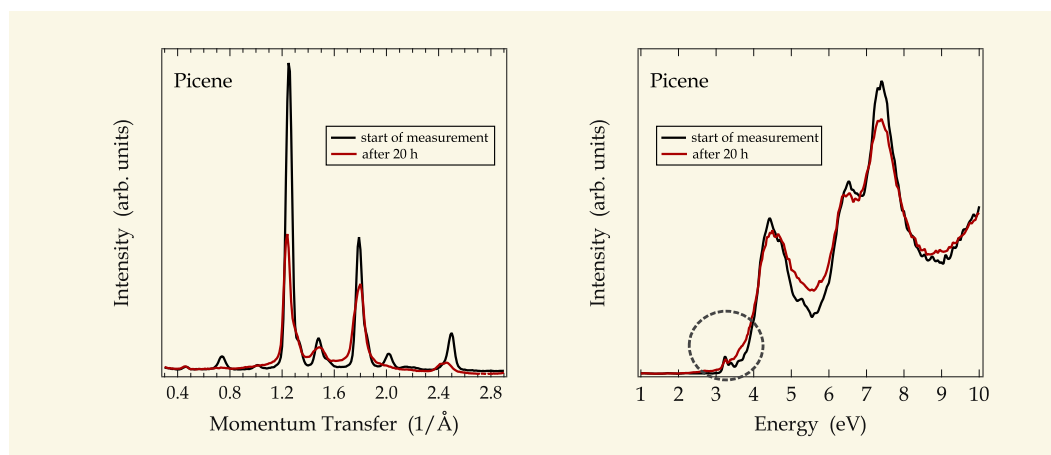
**T**UNING the electronic structure and carrier density by intercalation is crucial to modern day semiconductor technology. In general, the carrier density plays a pivotal role for the materials properties, because intercalation can induce, e. g., a charge transfer, a shift of the Fermi energy and in general wide-ranging changes in the electronic properties of the system. After the discovery of superconductivity in some polyaromatic hydrocarbons it is necessary to clarify the physical principle, which is responsible for their superconductivity state and their rather high transition temperatures. The foundation for the understanding of superconductivity in this “new” organic superconductors is the investigation of the physical properties of the corresponding molecular materials in the undoped state. With this knowledge we are later able to ascribe changes in the spectra directly to the introduced charge carriers, i. e., the doping procedure, and explain how and to which extent doping influences the electronic structure. Therefore, the aim of this chapter is to give an overview over the ground state properties of the investigated hydrocarbon systems and—in addition—compare acenes and phenacenes to get first evidence, what may explain their different behavior upon alkali metal doping. Moreover, the comparison with theoretical data helps to explain the nature of the observed excitations as well as the structure of the HOMO and LUMO.

### 4.1. Beam Damage Effects

Before we start to present our results on EELS measurements on several selected polycyclic hydrocarbon systems, a first important experimental result is the high sensitivity of all of the employed films to the electron exposure. Obviously the energy introduced into the sample by the electron beam causes tremendous changes. Figure 4.1 (left panel) reveals

---

\*Carl Friedrich Gauß (1777-1855). German mathematician and physical scientist who contributed significantly to many fields, including number theory, statistics, analysis, differential geometry, geodesy, geophysics, electrostatics, astronomy and optics.

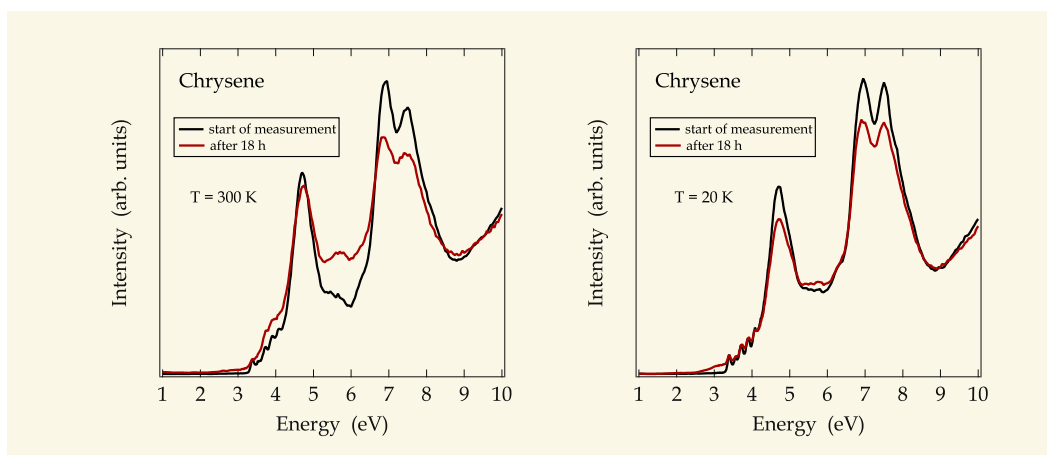


**Figure 4.1.** | Left panel: The variations of the Bragg spectra induced by the electron beam, shown for picene thin films with a pronounced texture. The black spectrum shows the Bragg diffraction profile after an exposure time of  $\approx 5$  min and the same spectrum is plotted after more than 20 hours of measuring (red spectrum). Right panel: The aging behavior of the loss-function for a typical picene thin film for a momentum transfer of  $q=0.1 \text{ \AA}^{-1}$ . The circle emphasises the modifications in the lowest lying electronic transition discussed in detail in the text.

a loss of intensity or rather vanishing of single peaks in the Bragg spectra, and further a broadening of the Bragg reflections for long measuring times. This observations can be seen as a direct evidence for an increase of the amorphous background and a destroyed periodic arrangement of the building blocks, indicated by the suppressed Bragg peaks. Moreover, also the electronic structure, i. e., the loss function suffers a strong mutation as depicted in Fig. 4.1 (right panel) where, as an example, the loss function of picene is shown. Also in case of the loss spectra a clear broadening of the individual features as well as the decrease in intensity is observable. These modifications occur over the whole spectrum and so the volume plasmon (not shown in Fig. 4.1) is affected as well as the lower lying electronic transition. Interestingly, the effect seems to be most pronounced for the small excitations right above the excitation onset (cf. circle in Fig. 4.1 and Fig. 4.2), so-called excitons.

Furthermore, the manipulator in our EELS spectrometer is equipped with a helium flow-cryostat and a temperature controller, allowing measurements in a temperature regime of  $T \approx 20 \dots 400$  K. A comparison of the effect of aging between samples measured at room temperature and samples measured at 20 K, as depicted in Fig. 4.2 exemplary for the case of chrysene, signals a suppression of the damaging effect by measuring at low temperatures. In detail, as shown in the left panel of Fig. 4.2, a clear decrease in intensity and broadening can be observed after 18 hours measuring at room temperature. Especially, the fine structure of the excitonic excitations in the range between 3 and 4.5 eV can not be identified after this exposure time. In contrast to that, the changes in the electronic structure are much weaker in case of cooling down the sample to 20 K. Slight changes

## 4.2. Electronic Properties Of Pristine Picene Thin Films



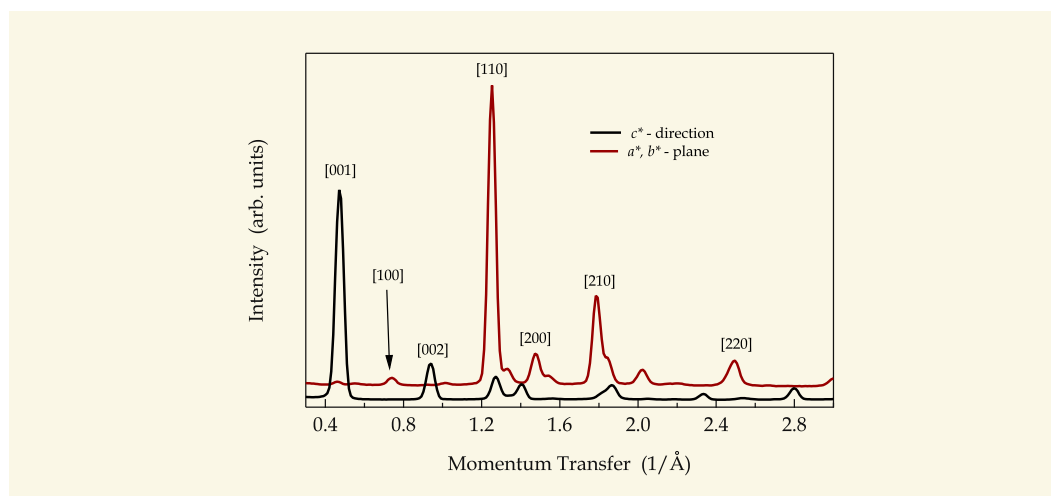
**Figure 4.2.** | Comparison of the effect of aging between measurements at 300 K and 20 K exemplary for the case of chrysene measured with a momentum transfer of  $q = 0.1 \text{ \AA}^{-1}$ .

are observable likewise, but even after 18 hours the pronounced fine structure right after the excitation onset can be distinguished, which gives rise to the assumption that the lifetime of the organic thin films can be extended when the measurements are performed at low temperatures. Additionally, similar aging effects were observed for all hydrocarbon systems under investigation in this thesis.

Unfortunately, the processes leading to these effects are unknown. A possible reason might be the creation of radicals by the electron beam which afterwards react with each other or with residual impurities within the vacuum chamber. Another possibility is the cracking of bonds between the different benzene rings within one hydrocarbon molecule. This expectation might be the reason for the much stronger aging effect that is observable for the excitonic structures, which are individual for every single molecule. Small changes, i. e., breaking of single bonds, influence them in a stronger way like the features at higher energies. The important message, which we learn from this observations is that the samples have to be checked repeatedly for any sign of degradation because otherwise no reliable data about the electronic structure would be obtained and a clear determination between doping introduced and degeneration changes is not possible. Therefore the experimental data presented in the following were measured several times and their reliability is ensured as they were shown to be reproducible for different samples and different measuring routines.

## 4.2. Electronic Properties Of Pristine Picene Thin Films

After the discovery of superconductivity in alkali metal-doped picene with transition temperatures up to 18 K first of all the investigation of the physical properties of undoped picene is required in order to develop an understanding of the normal-state properties and



**Figure 4.3.** | Electron diffraction profiles of solid picene for the two different orientated films. The values in parentheses give the corresponding Miller indices and their positions are in fair agreement with the structural data described in Ref. 67.

further to create a foundation for the discussion of the doping induced changes discussed in detail in Ch. 5.

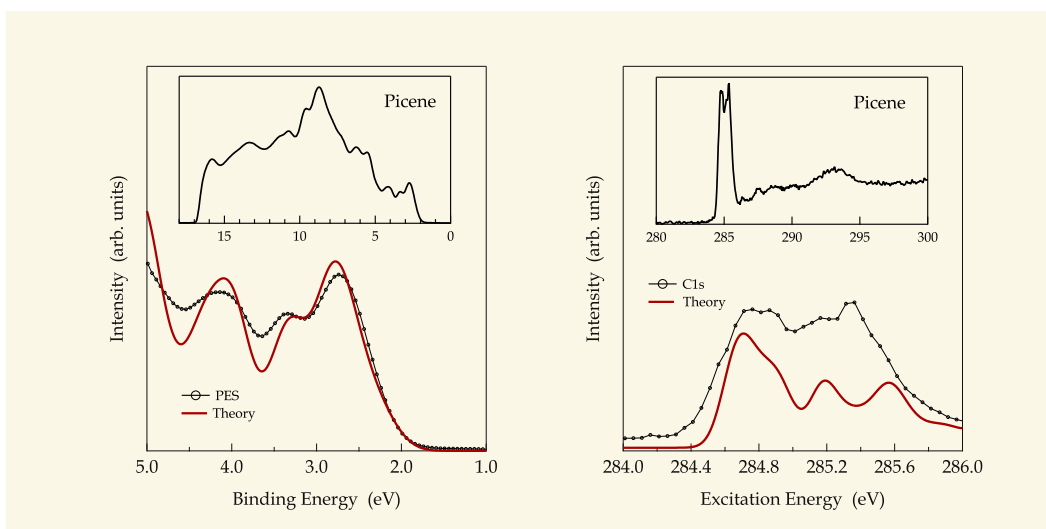
For our investigations using EELS, we prepared picene films with a thickness of about 100 nm by thermal evaporation (cf. Ch. 2 Sec. 2.4.2). Two deposition rates, 0.2 and 4 nm/min, were chosen to obtain films with different preferred crystal orientations. Prior to the EELS measurements the films were characterized *in situ* using electron diffraction. All the observed diffraction peaks were consistent with the crystal structure of picene as given in Tab. 3.2 in Sec. 3.2.1. Moreover, the diffraction spectra shown in Fig. 4.3 revealed a pronounced texture: films grown with a deposition rate of 0.2 nm/min showed a strong preference for crystallites having their  $a^*$ ,  $b^*$ -plane parallel to the film surface, whereas films grown with 4 nm/min showed a considerable number of crystallites having their  $c^*$ -axis on the film surface.

We start the presentation with the photoemission profiles of picene as shown in Fig. 4.4 (left panel), which is compared with the theoretical density of states (DOS), calculated within the accurate GW approximation of manybody perturbation theory by the group of A. Rubio<sup>†</sup> (For more details about the photoemission measurements and the theoretical calculations see Appendix C). The structures closest to the chemical potential (Binding Energy [BE] = 0 eV) arise from the  $\pi$ -derived highest occupied molecular orbital (HOMO) of picene followed by deeper-lying electronic states (HOMO-1, HOMO-2, etc.). Upon solid formation, these orbitals form bands with a relatively small bandwidth of about 0.5 eV since the interaction between the molecules in solid picene is essentially van der Waals like.

<sup>†</sup>A. Rubio, P. Cudazzo, and M. Gatti

(Nano-Bio Spectroscopy group and ETSF Scientific Development Centre, Departamento Física de Materiales, Universidad del País Vasco, Centro de Física de Materiales CSIC-UPV/EHU-MPC and DIPC, Av. Tolosa 72, ES-20018 San Sebastián, Spain)

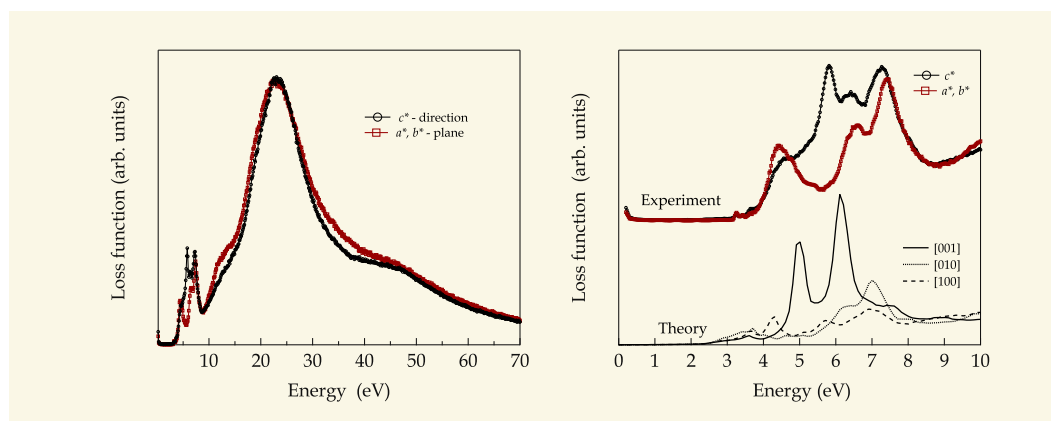
## 4.2. Electronic Properties Of Pristine Picene Thin Films



**Figure 4.4.** | Left panel: Valence band photoemission data of solid picene near the chemical potential. The inset shows the full spectrum including the secondary electron cutoff. Right panel: C 1s excitation data of solid picene measured using EELS. The inset shows a much larger energy range. In the case of the C 1s comparison, the theoretical data have been shifted such that the first peaks coincide.

The calculations based on DFT using LDA follow the results of Ref. 145, but there is a major modification of the shape of the DOS if many-body correlation effects embedded in the GW approximation are taken into account. Quasiparticle corrections change the positions and intensities of the main peaks. The final result is in excellent agreement with the measured PES data. Below about 6–7 eV BE, we find that the  $\sigma$ -derived states additionally contribute to the photoemission spectrum. The spectral sharpness of the photoemission structures confirms that upon solid formation the molecular electronic states of picene remain relatively unchanged. Closest to the chemical potential, the photoemission data reveal three maxima in the electronic DOS at 2.7, 3.35, and 4.15 eV, corresponding to the highest eight valence bands. This observation demonstrates that the first occupied electronic levels of Picene are quite close in energy. The onset of the occupied electronic DOS is at about 2 eV below the chemical potential (or Fermi energy), which indicates quite a large band gap of solid picene. The ionization potential of solid picene is determined using the data in Fig. 4.4 is 6.4 eV, i. e., picene is rather stable against oxidation as mentioned in Sec. 3.2.2. The work function of picene is thus 4.4 eV.

In the right panel of Fig. 4.4, the C 1s core excitation spectra of picene measured with EELS are depicted. Due to dipole selection rules, these data represent transitions into empty C 2p-derived levels. In other words, core level EELS is able to probe the projected unoccupied electronic DOS of carbon-based materials. We thus compare the experimental EELS with the unoccupied DOS calculated in the GW approximation. Analogous to other  $\pi$  electronic systems, the features below 291 eV are caused by excitations into  $\pi^*$ -derived electronic states. The step-like structure at about 291 eV corresponds to the onset of



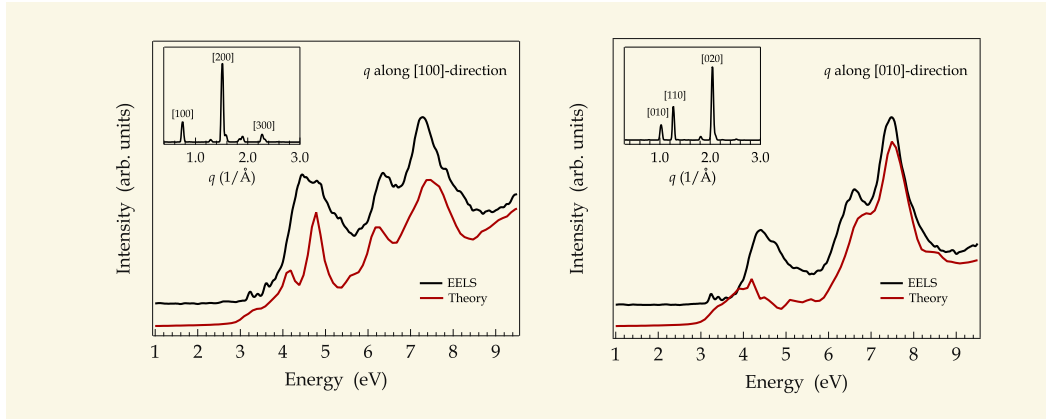
**Figure 4.5.** | Loss function of solid picene measured with a small momentum transfer of  $0.1 \text{ \AA}^{-1}$  for a wide energy range (left panel) and in an energy range between 0 - 10 eV (right panel). The experimental data represent excitations with predominant  $a^*, b^*$  polarization (red squares) and with a strong contribution of excitations polarized along the  $c^*$ -axis (black circles). Furthermore, a comparison with the theoretical loss function, calculated within the RPA, for the three fundamental directions [100], [010] and [001] is shown in the lower part.

transitions into  $\sigma^*$ -derived unoccupied levels. The C 1s core excitation spectrum of picene shows a very sharp and dominating excitation feature right after the excitation onset at 284.3 eV, due to excitonic interactions with the core hole [165–167]. This excitation feature is characterized by a fine structure with maxima at 284.75, 284.85, 285.15, and 285.35 eV. These peaks are in very good agreement with the theoretical data if GW corrections are taken into account. From this analysis, we can unambiguously assign those structures to several unoccupied levels that are very close in energy.

When doped with electrons, these states become occupied, and this quasi-degeneracy was proposed to cause a high DOS at the Fermi level in superconducting  $\text{K}_3\text{picene}$ , a situation that resembles that in fullerenes and would be favourable for a relatively high transition temperature into the superconducting state. Moreover, this quasi-degeneracy of the conduction bands is also helpful in reducing the impact of electron correlation effects, i. e., to realize a metallic ground state similar to  $\text{K}_3\text{C}_{60}$  [10], which is a necessary prerequisite for superconductivity.

After this discussion of the occupied and unoccupied DOS we present in Fig. 4.5 the loss function of solid picene, which provides insight into the electronic excitations of this compound. The experimental data presented in Fig. 4.5 are taken with a small momentum transfer  $q$  of  $0.1 \text{ \AA}^{-1}$ , which represents the so-called optical limit. Taking into account the anisotropic molecular and crystal structure of picene, it is reasonable to expect an anisotropic loss function as well. For a momentum transfer  $q$  parallel to the  $a^*, b^*$  plane as well as to the  $c^*$ -axis the loss function of picene is dominated by a broad structure at about 23 eV (cf. Fig. 4.5), which is attributed to the volume plasmon, a collective excitation of all valence electrons ( $\pi + \sigma$  plasmon). With increasing thickness of the films there is an

## 4.2. Electronic Properties Of Pristine Picene Thin Films



**Figure 4.6.** | The loss function spectra for  $q=0.1 \text{ \AA}^{-1}$  along the two main crystallographic directions,  $a^*$  and  $b^*$ , measured in a picene single crystal. For a better comparison the theoretical spectra were slightly shifted to higher energies.

enlarged possibility for multiple scattering within the sample leading to additional peaks at integer values of the plasmon frequency. This explains the shoulders around 46 eV in Fig. 4.5 (left panel). However, the well-structured loss function below 10 eV with clear maxima at about 4.6, 5.8, 6.4, and 7.3 eV in the experimental spectra is a signature of the energetically sharp and well-defined molecular electronic levels of picene, which remain relatively unchanged going to the solid state. The theoretical results for the loss function, calculated in the framework of the RPA [12, 26], match the experimental measurements very well and provide fundamental insights which help to interpret the spectra. The fact that the observed maxima with high intensity are close in energy is also in good agreement with the well-structured data shown in Fig. 4.4 for the electronic DOS, and we ascribe the excitation maxima in Fig. 4.5 to excitations between the energetically close-lying first occupied and unoccupied electronic states of picene. With respect to the experimental spectra, the theoretical results show a slight underestimation of the peak positions due to the fact that the band gap opening due to GW corrections and excitonic effects—both absent in the calculations—do not exactly compensate for each other. From the analysis of the theoretical spectra we find that in the spectrum with  $q$  parallel to the [001]-axis the first main structure at about 5 eV is located in the continuum of single-particle excitations and is due to interband transitions (seen as peaks in the imaginary part of  $\epsilon$ ). Instead, the second peak at about 6.1 eV occurs in correspondence to a zero of the real part of  $\epsilon$ , where also the imaginary part is small. Therefore, this structure can be assigned to a plasmon, related to collective excitations with  $\pi$  character.

In addition to the polycrystalline samples discussed above we also prepared single crystals of picene via physical vapor growth in a vertical geometry over 12 hours under normal pressure. The resulting crystals are very tiny and the profit is very limited. In spite of it all we were able to collect some measurable single crystals of picene. The corresponding elastic scattering profiles for the two main crystallographic directions,  $a^*$  and  $b^*$ , are shown as inset in Fig. 4.6. Indeed the observed diffraction peaks were

consistent with the reported crystal structure of picene and further these spectra show that our samples are single crystalline and within this very simple manufacturing process of rather high quality.

The comparison with the calculated loss spectra for the  $a^*$  and  $b^*$ , as shown in Fig. 4.6, implies a very good agreement between theory and experiment. The main features are well reproduced by the calculations and can be assigned to interband transitions. Additional to the polycrystalline films, which are a mixture of different crystallite directions, the single crystal spectra show a slight anisotropy between the two directions. The differences between theory and experiment, i. e., the redshift of the theoretical spectra in the peak positions, can be explained as a consequence of the fact that the LDA band-gap underestimation is larger than the electron-hole binding energy (for a better comparison the difference is compensated in Fig. 4.6 by a  $x$ -offset of 0.5 eV of the calculated spectra). Unfortunately, we were not able to measure the spectra with  $q$  oriented along the  $c^*$ -direction, due to the orientation of the single crystals and the properties of the manipulator.

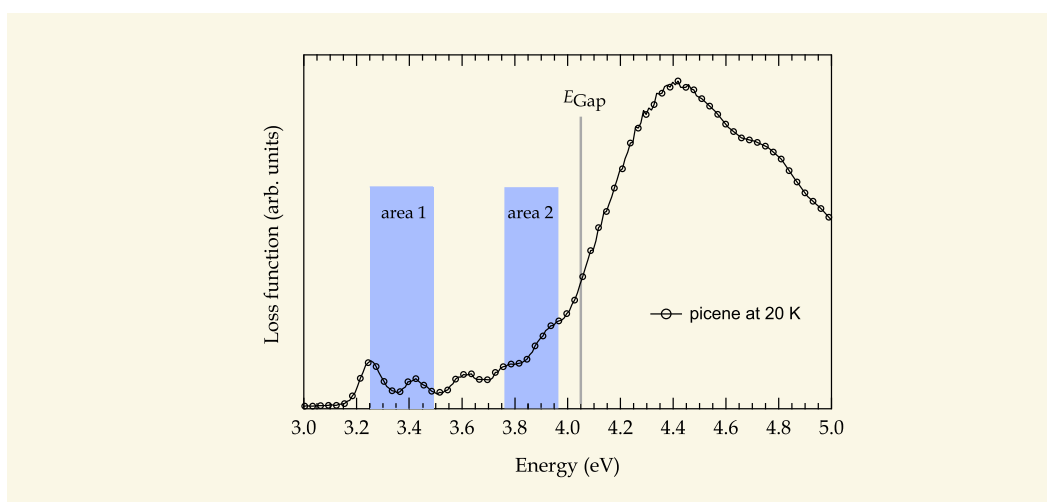
#### 4.2.1. Kramers-Kronig Analysis Of Undoped Picene

As mentioned in Sec. 2.3, further informations about the electronic properties of a system can be gained by performing a Kramers-Kronig analysis, which provides us with other typical optical parameters like the real and imaginary part of the dielectric function or the optical conductivity. To be able to perform such a KKA, the raw data have to be corrected by reasonable subtraction of the elastic line and multiple scattering effects. This was done under consideration according to the following procedure. A constant background was subtracted from the whole spectrum which accounts for the noise of the photo multiplier. This was done simply to reduce the signal to zero below the onset of the lowest lying structure in the loss function spectra which is motivated by vanishing absorption between the valence band and the exciton ground state (cf. Sec. 4.2.2). To reduce the influence of multiple scattering (represented by the shoulder around 46 eV in the spectra) these structures were removed from the raw data by assuming a  $\omega^{-3}$  behavior of the loss function which is typical for a Lorentz oscillator in the limit  $\omega \rightarrow \infty$  [168]. Subsequently, a KKA was performed under the side condition of the strictly valid sum rule (see Eq. 2.28). An evaluation of this sum rule for the loss function and the dielectric function after our KKA results in a very good agreement of the two values with an error of less than 1.2%. Additionally, from the comparison with the value of the plasma frequency calculated from the number of valence electrons  $N$  (with  $N = 204$  electrons per unit cell indicates the electron density in the case of picene) we obtain a value of about 3 - 3.5 for the background dielectric function  $\epsilon_\infty$ , which is in a very good agreement with the calculated value of  $\epsilon_1(E = 0)$ .



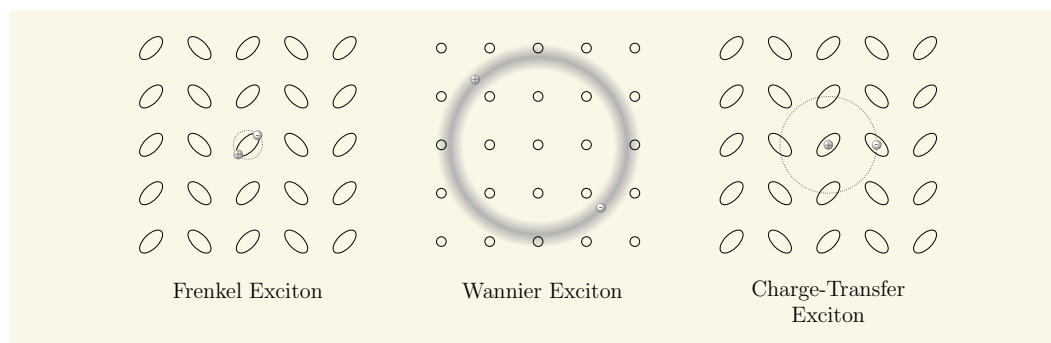
## 4.2.2. Exciton Character In Picene Molecular Solids

Zooming into the energy region around the excitation onset reveals an onset in the experimental spectra, i. e., an optical gap, of 3.15 eV. This onset also represents a lower limit for the band gap (or transport energy gap) of solid picene. While the fundamental band gap is severely underestimated by the 2.39 eV LDA result (see also [145]), the GW band structure displays a direct quasiparticle gap of 4.08 eV (at the Z point of the Brillouin zone) [130]. The excitation onset of picene is followed by a pronounced fine structure as depicted in Fig. 4.7. One can identify five well separated features at 3.25, 3.41, 3.61, 3.77, and 3.93 eV. Compared to EELS measurements of solid picene at room temperature (cf. Fig. 4.5), these low-energy structures are significantly better resolved and well defined upon cooling down to 20 K.



**Figure 4.7.** Loss function of solid picene measured with a momentum transfer of  $q = 0.1 \text{ \AA}^{-1}$  at 20 K. The two emphasized areas indicate the energy ranges of former observed peaks in the optical-absorption spectrum of picene in solution as reported in Refs. 169 and 170. In addition, the transport energy gap  $E_{Gap}$  of solid picene is indicated.

In general, the lowest electronic excitations in organic molecular solids usually are excitons, i. e., bound electron-hole pairs [81, 91, 92, 171, 172]. This is one of the consequences of the weak van der Waals interaction between the molecules, which is responsible for the molecular arrangement in the crystal. The decision criterion that has to be considered to analyze the excitonic character and binding energy of an excitation is the energy of the excitation with respect to the so-called transport energy gap, which represents the energy needed to create an unbound, independent electron-hole pair. This transport energy gap of picene has been estimated to about 4.05 eV [131]. Consequently, the five excitation features in solid picene that are observed below 4 eV as depicted in Fig. 4.7 are excitons, and the exciton binding energy of the lowest-lying exciton is as large as about 0.85 eV. The results of the GW-calculations also imply that in picene one should expect an exciton BE larger



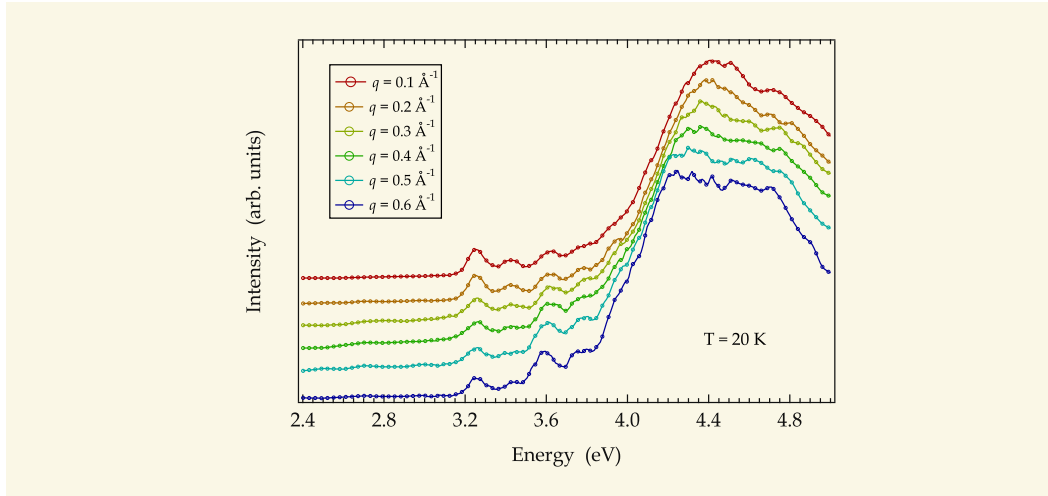
**Figure 4.8.** | Schematic view of a Frenkel- (left), Wannier- (middle), and Charge-Transfer-Exciton (right), whereby the ball with a plus or a minus sign symbolizes a hole or a electron, respectively. The Frenkel state is very localized and therefore also more tightly bound whereas in case of a Wannier exciton the electron distribution is spread over a wide area (indicated by the large circle) of the lattice. Depending on the exact conditions it is also possible to generate an intermediate state that is typically spread over one or two adjacent lattice molecules, often termed charge-transfer (CT) exciton.

than that in its close relative pentacene, where it is less than 0.5 eV and where a smaller band gap (2.3 eV) has also been reported [173–176].

In addition, the electronic excitation spectrum of individual picene molecules has been studied in the past using optical-absorption measurements [169, 170]. In Fig. 4.7, we have highlighted the energy areas in which these optical data show corresponding excitation structures. Intriguingly, these studies reveal five excitations below 4 eV, however no excitation feature has been observed so far in the energy window around 3.61 eV. In general, electronic excitations in solution and in the condensed phase can be observed at different energies due to different screening effects related to the polarization of the surrounding. An assignment of the excitation at 3.61 eV to one of the features observed for picene molecules in solution would thus require a downshift of this excitation feature of about 200 meV or more going to the condensed phase. However, we do not observe such a large shift for the lowest-lying excitations; in their case, the difference between solution and solid-state data is smaller than 40 meV. As a consequence, an assignment of the excitation feature at 3.61 eV to a molecular electronic transition also seen in the optical absorption of picene molecules in solution would require an anisotropy of the dielectric screening of more than a factor of 5, taking into account the different polarization of the excitations [169]. Such a large anisotropy, however, is very unlikely for a molecular crystal made out of aromatic hydrocarbons. For instance, in the case of pentacene ellipsometry investigations of single crystals revealed a maximal anisotropy of the dielectric constant along the crystal axes of less than 1.8 [177]. We therefore assign the exciton at 3.61 eV to a solid-state induced electronic excitation, a conclusion that is further supported by the momentum dependence of this excitation, as discussed below.

The most likely candidate for such an excitation is a charge transfer transition, where in the final state the electron and hole sit on adjacent picene molecules (cf. 4.8). This is

## 4.2. Electronic Properties Of Pristine Picene Thin Films



**Figure 4.9.** | Momentum dependence of the EELS spectra of solid picene. The measurements were carried out at  $T = 20$  K.

reminiscent of the low energy excitations of pentacene, where also such charge transfer excitations have been discussed [173, 175, 178]. Within a simple point charge approach, one can estimate the binding energy  $E_B$  of such a charge transfer exciton using

$$E_B \sim \frac{1}{4\pi\epsilon_0\epsilon_r} \frac{e^2}{\langle r \rangle},$$

where  $\langle r \rangle$  denotes the mean distance between two adjacent molecules which participate in the charge transfer excitation, and  $\epsilon_r$  is the static dielectric constant ( $\epsilon_r \sim 3.5$  for picene). The distance of the two adjacent molecules in the  $a, b$ -plane of solid picene is about  $5.3 \text{ \AA}$ , which leads to an estimate for  $E_B$  of about  $0.7 \text{ eV}$ . In other words, in picene it is reasonable to assume charge transfer excitons at similar energies as intra-molecular excitons, also called Frenkel excitons. Moreover, the presence of both types of excitons at similar energies can lead to a sizable interaction of these excitation species and result in excitons with a mixed character, a situation that has been discussed in the past also for other organic molecular solids (for a detailed discussion see Sec. 4.4) [179–181].

In order to obtain a more detailed picture of the excitons in picene we have measured the loss function with increasing momentum transfer  $q$ . As shown in Fig. 4.9, all identified excitons in picene with the exception of the feature at  $3.61 \text{ eV}$  do not change in energy within a momentum range up to  $0.6 \text{ \AA}^{-1}$ , which covers almost the entire first Brillouin zone parallel to the  $a^*, b^*$  crystal directions. Consequently, in the framework of an exciton band structure description this yields a vanishing group velocity ( $\sim \frac{\partial E(k)}{\partial k}$ ) for these excitations, i. e., they can be regarded as rather localized. For the excitation at  $3.61 \text{ eV}$  a very small negative dispersion of about  $30 \text{ meV}$  can be observed in Fig. 4.9. In consideration of the assignment of this excitation to a charge transfer exciton (see above), this finite dispersion

would corroborate the different character of this excitation, we however emphasize that the size of the dispersion is close to the experimental resolution.

Interestingly, we can also identify a substantial intensity variation, especially for the three excitons lowest in energy. Moreover, while the intensity of the first two excitons at 3.25 and 3.41 eV decreases with increasing momentum transfer  $q$ , the opposite is the case for the exciton observed at 3.61 eV. In case of localized excitations, i. e., those with negligible dispersion, their character can be analyzed in terms of a multipole expansion, whereas upon increasing momentum transfer dipole (or optically) allowed excitations loose intensity and dipole forbidden excitations (e. g., quadrupole transitions) will increase in intensity [182–185].

In detail, the matrix element  $M$  for EELS is proportional to  $\langle f | \exp(iqr) | i \rangle$  which can be expanded to

$$M \propto \sum_n \frac{i^n}{n!} (q\langle r \rangle)^n \left\langle f \left| \left( \frac{r}{\langle r \rangle} \right)^n \right| i \right\rangle.$$

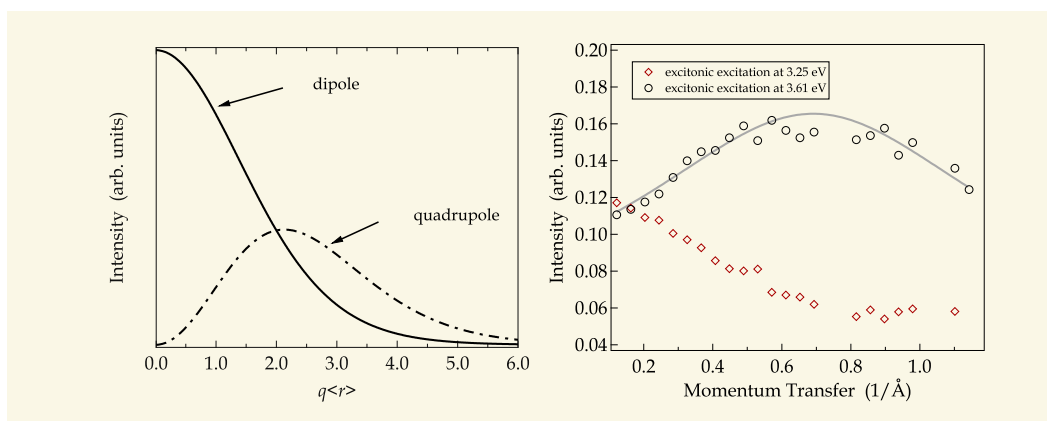
Hereby, the introduction of a mean radius  $\langle r \rangle$  allows one to separate the characteristic dimensionless  $q\langle r \rangle$  dependence of the matrix element from the (now also dimensionless) constant excitation probability  $\langle f | (r/\langle r \rangle)^n | i \rangle$ . In the case of excitations with a specific multipole character, e. g., dipole excitations, the latter has a finite value only for the corresponding  $n$  (e. g.,  $n=1$ ). The mean radius  $\langle r \rangle$  gives a measure for the extension of the electron-hole wave function  $\Psi_{e-h}(r)$  in the excited state, which represents the probability amplitude to find the electron at a certain distance  $\langle r \rangle$  assuming that the hole is fixed. Therefore, the momentum dependence of the excitation intensity  $I_n$  ( $\propto |M|^2$ ) of an excitation with a specific multipole character can be written as

$$I_n \propto \frac{n!^{-2} (q\langle r \rangle)^{2n}}{N}, \quad N = \sum_n \frac{(q\langle r \rangle)^{2n}}{n!^2}.$$

$N$  is the sum over the intensities of all excited (final) multipole contributions and represents a normalization factor which guarantees the oscillator strength sum rule. In the left panel of Fig. 4.10 we show the intensities  $I_n$  as a function of  $q\langle r \rangle$  for  $n=1$  (dipole excitation) and  $n=2$  (quadrupole excitation).

Thus, the two singlet excitons with lowest excitation energy in solid picene are of predominant dipole character, while the following exciton at 3.61 eV is characterized by a significant dipole forbidden contribution. Furthermore, the momentum value  $q_{max}$ , where a dipole forbidden excitation reaches its intensity maximum can be used to estimate the mean radius of the wave function of this excitation:  $\langle r \rangle \sim 2/q_{max}$  [183, 185]. In Fig. 4.10 (right panel) we present a comparison of the intensity variation of the excitons at 3.25 and 3.61 eV. Again, the decreasing intensity for the lowest lying exciton clearly signals its predominant dipole allowed character in good agreement to the fact that this feature was also observed in optical absorption measurements of picene molecules in solution [169, 170]. In contrast, the intensity of the 3.61 eV exciton reaches its intensity maximum at finite

### 4.3. Electronic Properties Of Pristine Coronene Thin Films

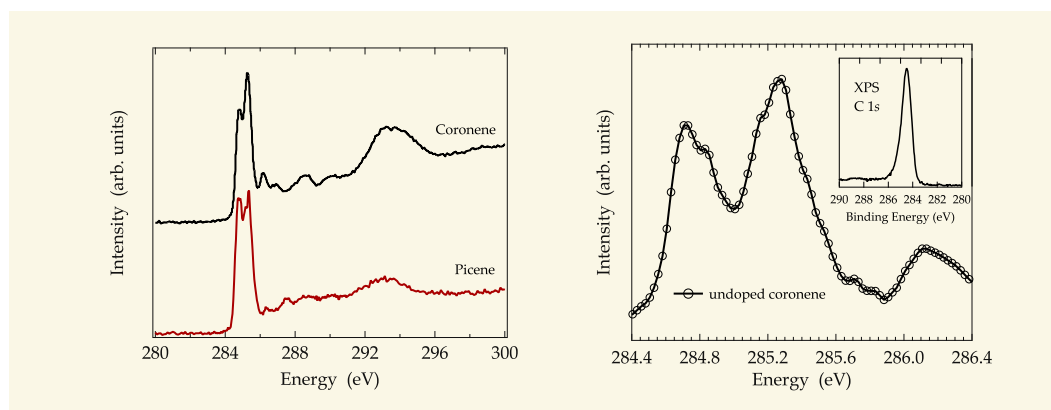


**Figure 4.10.** | Left panel: Intensity of a pure dipole or quadrupole excitation in EELS as a function of the reduced parameter  $q\langle r \rangle$ . Right panel: Momentum dependence of the spectral weight of the two excitonic excitations at 3.25 eV (red diamonds) and 3.61 eV (black circles) as observed in the loss function of solid picene. The data around  $0.75 \text{\AA}^{-1}$  and  $1.05 \text{\AA}^{-1}$  could not be determined accurately enough because of considerably enhanced multiple scattering in this region due to [100] and [010] Bragg reflections. The data are normalized to the  $q$  dependent intensity variation at 10 eV excitation energy in order to take into account the overall momentum dependence of the scattering cross section.

momentum (about  $0.7 \text{\AA}^{-1}$ ) as would be theoretically expected for, e. g., a quadrupole excitation [185]. This underlines a significant dipole forbidden part and now gives a (very rough) estimate of the radius of this exciton of about  $3 \text{\AA}$ . Here, one should keep in mind that our data also suggest a mixed character of the excitons in solid picene (see discussion above), which limits a quantitative analysis of the exciton extension. Nevertheless, the observed momentum maximum is in reasonable agreement to our interpretation of the exciton at 3.61 eV having charge transfer character.

### 4.3. Electronic Properties Of Pristine Coronene Thin Films

After picene also coronene was found to become superconducting upon potassium intercalation. It is therefore obvious to investigate the electronic structure also for coronene—first of all in the undoped phase. The starting point of the investigation of the undoped coronene films is very similar to picene. In Fig. 4.11 we present the carbon 1s core-level excitation of pristine coronene. The comparison with the C 1s excitation of picene displays that the principle shape of the spectrum is very similar. We can clearly identify a sharp and strong feature in the range between 284 and 286 eV as well as a broad excitation at  $\sim 294$  eV, which can be discussed in a similar way as in the case of picene (see Sec. 4.2). Moreover, the spectrum shows additional small features at 286.1, 286.9, 288.6, and 290.2 eV. Because of the higher symmetry of the coronene molecules, compared to picene, we expect a degeneracy of the higher molecular orbitals which can be directly seen by the well-separated features

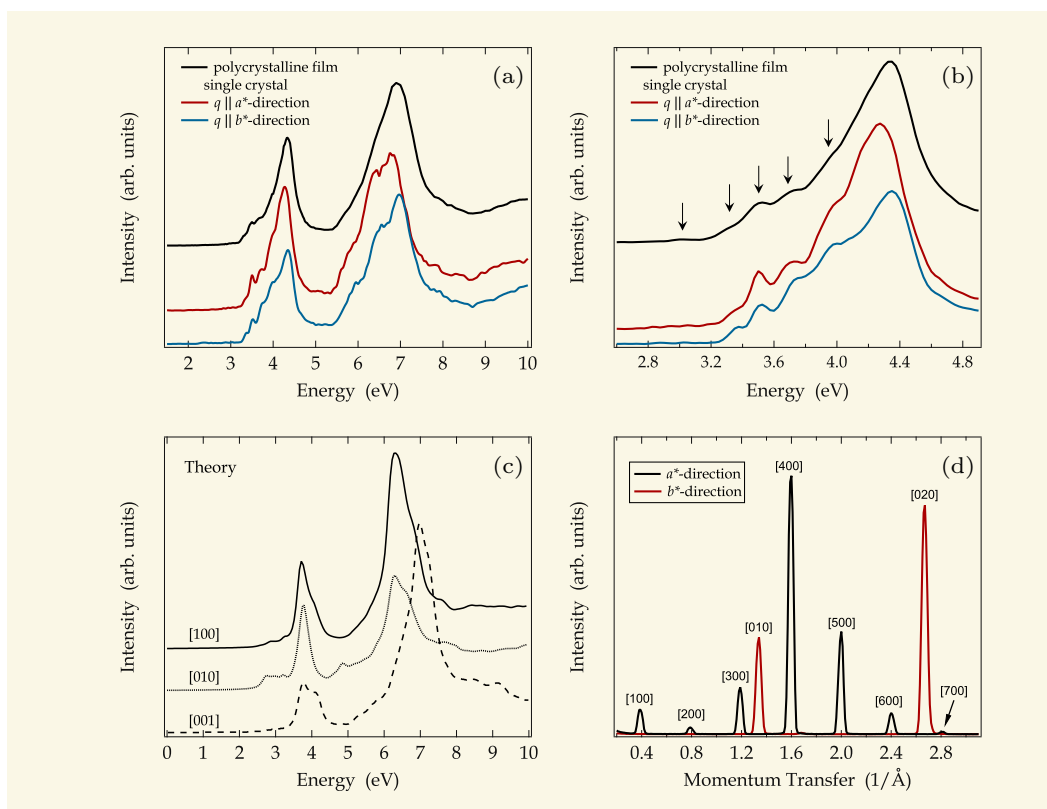


**Figure 4.11.** | Left panel: C 1s core-level excitations of pristine coronene in comparison with pristine picene. Right panel: Zoom at the dominant C 1s excitation right after the excitation onset at 284.4 eV for undoped coronene measured with higher energy resolution (85 meV). The inset shows the C 1s core-level spectrum for an undoped coronene film grown on SiO<sub>2</sub> and measured using x-ray photoemission spectroscopy (XPS).

above 286 eV. Such a well-pronounced structure representing higher lying molecular orbitals is very similar to what was observed for fullerene [186–189]. When we focus on the dominating excitation feature right after the excitation onset, as shown in the right panel of Fig. 4.11, we can identify a characteristic fine structure with maxima at 284.75, 284.85, 285.15, and 285.35 eV. These features can be identified with maxima in the unoccupied density of states, since the C 1s levels of the different C atoms in coronene are virtually equivalent as revealed by x-ray photoemission spectra (see Fig. 4.11 and Ref. 190). The peak width of the C 1s photoemission line is smaller than 1 eV as seen in the inset of Fig. 4.11 (Note that the energy resolution for the XPS measurements is  $\approx 0.35$  eV). The broadening of the spectral linewidth is a result of lifetime effects, very similar to what was observed for C<sub>60</sub>, where all carbon atoms are symmetrically equivalent [191].) The observation of four peaks in Fig. 4.11 (right panel) is in very good agreement with first-principles band structure calculations for undoped coronene, which found four close-lying conduction bands (arising from the doubly degenerate LUMO with  $e_{1g}$  symmetry as well as the doubly degenerate LUMO+1 with  $e_{2u}$  symmetry) in this energy region [164].

Furthermore, we show in Fig. 4.12 (a) a comparison of the loss functions measured of a polycrystalline film as well as of a single crystal of coronene in an energy range of 0–10 eV. These data are taken with a small momentum transfer  $q$  of  $0.1 \text{ \AA}^{-1}$ . For undoped coronene, we can clearly identify two main maxima at about 4.3 and 6.9 eV. The single crystalline samples were a priori characterized by elastic scattering and the electron diffraction profiles, as shown in Fig. 4.12 (d), reveal the very good quality of the crystals. The loss spectra of the single crystal show in addition that there is no significant polarization dependence. The overall shape of the spectra and peak positions are the same for measurements with  $q$  parallel to the  $a^*$ - and to the  $b^*$ -direction. Moreover,

### 4.3. Electronic Properties Of Pristine Coronene Thin Films



**Figure 4.12.** (a),(b) Loss function of a polycrystalline as well as a single crystalline sample of pristine coronene. In case of the single crystal the measurements were performed along the two main crystallographic axes  $a^*$  and  $b^*$ . (c) Calculated loss function for  $q$  along [100]-, [010]-, and [001]-direction. (d) Electron diffraction profiles of solid coronene for momentum transfers parallel to  $a^*$ - and  $b^*$ -direction revealing the very good quality of the employed thin films. The values in parentheses give the corresponding Miller indices and their positions are in fair agreement with the structural data described in Tab. 3.2.

LDA calculations including GW correction were evaluated [151] and display a very good agreement with our measurements (cf. Fig. 4.12 (c)). From the calculations we can assign the first main feature to interband transitions while the second one is a localized plasmon. In addition, zooming into the energy region around the excitation onset in the experimental spectra reveals an optical gap of 2.8 eV (see Fig. 4.12 (b)). This onset also represents a lower limit for the band gap of solid coronene. The excitation onset of coronene is followed by five additional well-separated features at 3, 3.3, 3.5, 3.7, and 3.95 eV indicated with arrows in Fig. 4.12 (b). The main features of our spectrum are in good agreement with previous EEL measurements in the gas phase [192, 193] and optical absorption data [194, 195]. Unfortunately, different values for the transport energy gap from 3.29 eV up to 3.54 and 3.62 eV were published in previous publications [190, 196, 197]. Consequently, only the lowest excitation that is observed can safely be attributed to a singlet exciton.

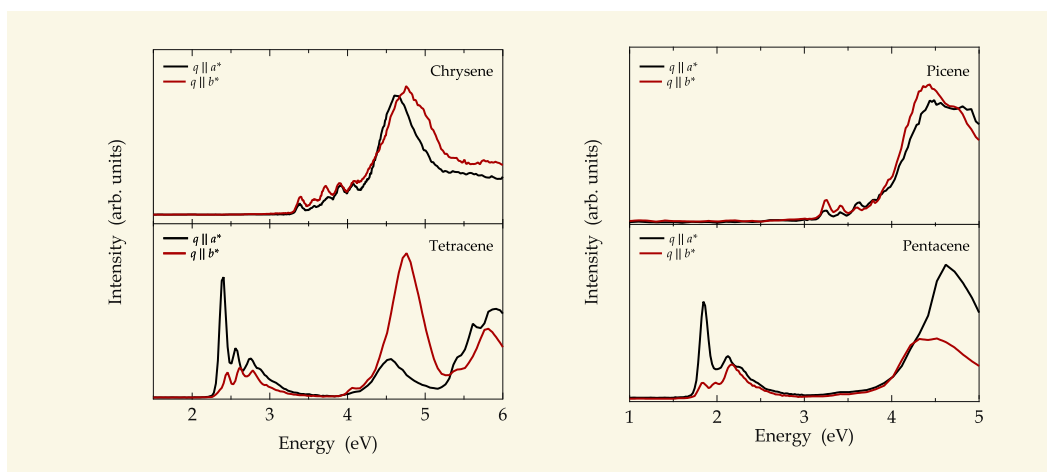
#### 4.4. Comparison Between The Electronic Structure Of Selected Acenes And Phenacene

The close structural relationship between acenes and phenacenes implies that a comparison of the electronic structure can help to deepen the knowledge about these aromatic hydrocarbons and might be a way to answer the question what makes picene so special compared to pentacene. Therefore, we compared the loss function of chrysene (four benzene rings connected in a zig-zag manner) to the one of tetracene (linear arrangement of four benzene rings) as well as the one of picene (five benzene rings connected in a zig-zag manner) to the one pentacene (linear arrangement of five benzene rings) single crystals. All measurements have been done for a small momentum transfer of  $0.1 \text{ \AA}^{-1}$  parallel to the two main crystallographic axes,  $a^*$  and  $b^*$ . Figure 4.13 reveals the significant difference in regard to the relative spectral weight of the low energy excitations of these four hydrocarbons. First of all, the clear difference of the size of the optical gap is in good agreement with previous publications [93–96].

For chrysene and picene (see upper panel in Fig. 4.13) we observe a broad peak around 4.5 eV as well as a pronounced fine structure right after the excitation onset. The main features in our spectra, except for some small intensity variations, are in very good agreement with previous optical absorption data [198]. Often, the low energy electronic excitations in molecular solids are excitons, as discussed in the previous section. This is also true for the two phenacenes studied here since their excitation onset is significantly below the transport energy gap which has been estimated to be about 4.2 eV for chrysene and 4 eV for picene [131, 154]. The equivalent is true for tetracene and pentacene with transport gaps of about 3.3 and 2.2 eV, respectively [176, 199, 200]. For many molecular crystals it is not unusual that the lowest singlet excitations are split into Davydov components, which arise from the interaction of the excitation dipoles of the symmetrically inequivalent molecules in the crystal unit cell [201]. These Davydov components frequently have a particular polarization dependence. In general, this can be also seen in our data and results in the two different energy positions of the first peak for  $q$  polarized along  $a^*$  and  $b^*$ . The spectra for chrysene and picene however—as shown in Fig. 4.13—are isotropic in terms of the energy positions, and only some small intensity variations were seen, going from the  $a^*$  to the  $b^*$  directions. Thus, our data do not reveal different Davydov components. This might be related to the rather small spectral weight of the lowest lying excitations in these materials, which could also imply a rather small Davydov splitting [91, 201].

Going to the linear acene crystals (lower panels in Fig. 4.13), these observations change substantially. The low energy excitations occur at much lower energies, their spectral weight is much larger, and their fine structure is significantly different. From older systematic studies of the optical absorption spectra of acenes and phenacenes as a function of the molecule lengths it is known that the energy position of these excitations in acenes quite strongly shifts to lower energies upon increasing the length of the molecules, while it remains quite constant in the case of the phenacenes [93]. This is related to the molecular structure and symmetry, which allows a delocalization of the HOMO and the LUMO

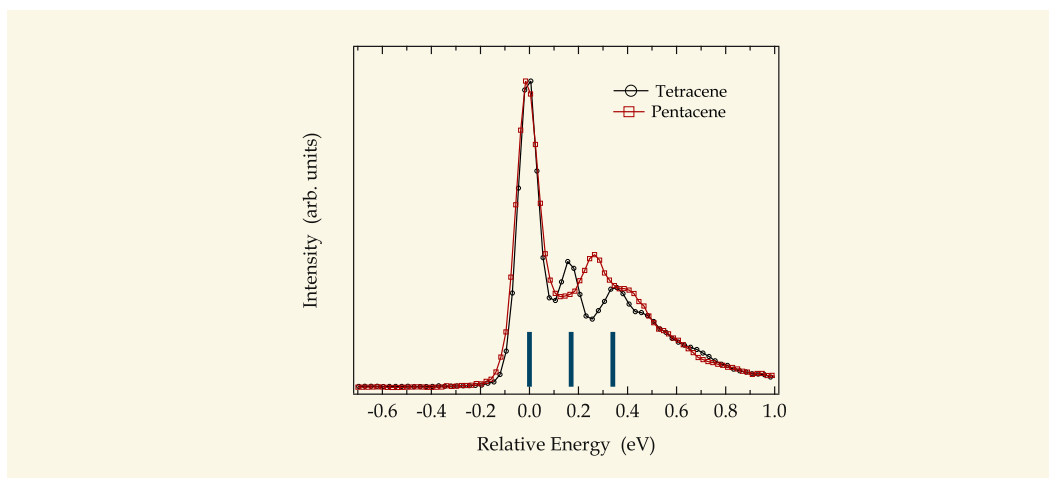




**Figure 4.13.** | Loss function of chrysene and tetracene (left panel) as well as picene and pentacene (right panel) single crystals for momentum transfers parallel to the two main directions in reciprocal space,  $a^*$  and  $b^*$ . The absolute value of the momentum transfer is  $0.1 \text{ \AA}^{-1}$  for all measurements.

of acenes over the entire molecules, while for their counterparts these orbitals remain localized at particular sites of the molecule [93, 202]. This difference in the molecular orbital structures most likely is also responsible for the different excitation probabilities (intensities), since this is directly related to the overlap of these orbitals. In view of the different excitation intensities it is also tempting to attribute the clearly observed Davydov splitting for tetracene (with Davydov components at about 2.38 and 2.45 eV) and pentacene (with Davydov components at about 1.84 and 1.98 eV) to the larger excitation dipoles for acenes. However, it has been shown recently that neither the Davydov splitting nor the exciton dispersion in acene crystals can be explained on the basis of molecular excitations only, but they can only be understood when an admixture of charge transfer (CT) excitations to the molecular (Frenkel) excitons is taken into account [203]. Finally, it is interesting to note that at energies of 4.5 and 5 eV the spectra of the four materials show qualitative similarities, in contrast to lower energies. In all four cases, there is a clear spectral structure in this energy range, which in addition is characterized by a similar anisotropy of the energy position.

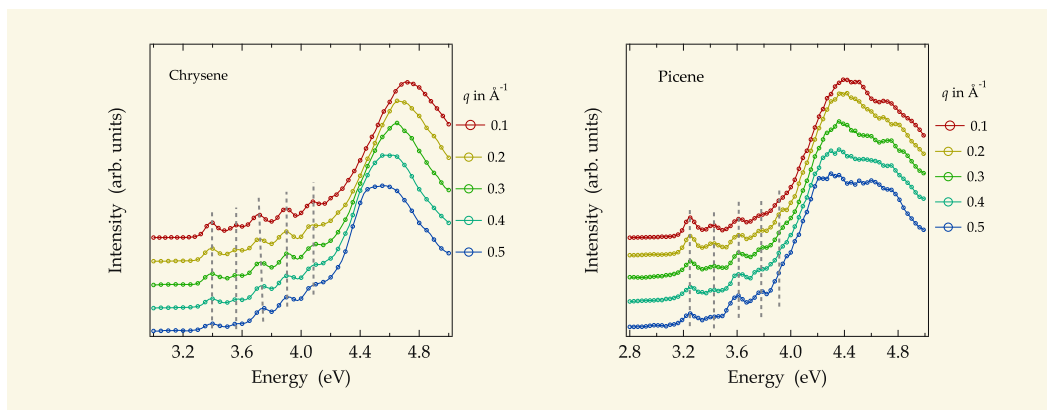
To get a deeper insight into the contribution of CT excitons to the acene spectra we show in Fig. 4.14 a comparison of the excitation spectra for tetracene and pentacene with the momentum vector parallel to the corresponding  $a^*$  axis. These spectra have been shifted in energy such that the first excitation features coincide and they were normalized to the same peak height of the first feature. The excitation spectrum of tetracene consists of the main peak followed by equidistant vibrational satellites as has been also observed in previous optical studies of crystals and films [198, 206]. Moreover, this vibrational progression is also seen in optical absorption data of tetracene in solution [204], i. e., for individual molecules, and the energy distance between the satellites of about 170 meV corresponds



**Figure 4.14.** | Comparison of the exciton structure of tetracene and pentacene measured with  $q$  parallel to the  $a^*$ -axis. The energy positions of the main excitation and vibrational satellites in the optical absorption spectra of tetracene and pentacene in solution [204, 205] are indicated by vertical bars.

well to C—C stretching vibrations observed using Raman scattering [207]. Thus, at least on a qualitative level the tetracene excitation spectrum can be rationalized by molecular (Frenkel) excitons that couple to molecular vibrations. The equivalent picture may now be expected for pentacene, since the corresponding vibrations as well as their impact on electronic levels should be very similar for the two molecules. Figure 4.14 however does not support this expectation. Instead, the pentacene spectrum is characterized by a satellite feature at about 270 meV above the main excitation. This energy distance is far too large to represent a vibrational satellite, and consequently the excitation 270 meV above the main feature must be of different origin.

In the light of the discussion above and recent reports in the literature we attribute the second excitation feature in the pentacene spectrum as seen in Fig. 4.14 to CT excitations in the crystal. In general, this assignment is in agreement with electro-absorption data where a CT excitation was reported at about 2.12 eV [208]. Also, calculations of the electronic polarization in pentacene crystals and the energy of CT states have indicated that such CT states have a binding energy of about 0.7 eV, which is of the same magnitude as the molecular Frenkel excitons [209]. Given this close excitation energy of Frenkel and CT states, they have to interact, i. e., excitation spectroscopy will probe mixed Frenkel-CT states. Indeed, recent advanced calculations of the singlet excitation spectra of acene crystals [203] and other  $\pi$ -conjugated molecular crystals [210, 211] as well as experimental studies [212] demonstrated that the exact spectral shape can only be understood with the inclusion of CT excitons and their coupling to the molecular Frenkel states. Interestingly, these calculations also predict that the contribution of the CT excitations to the lowest exciton feature quite significantly varies as a function of the length of the acene molecule. For tetracene a 27% contribution was reported, while for pentacene this contribution

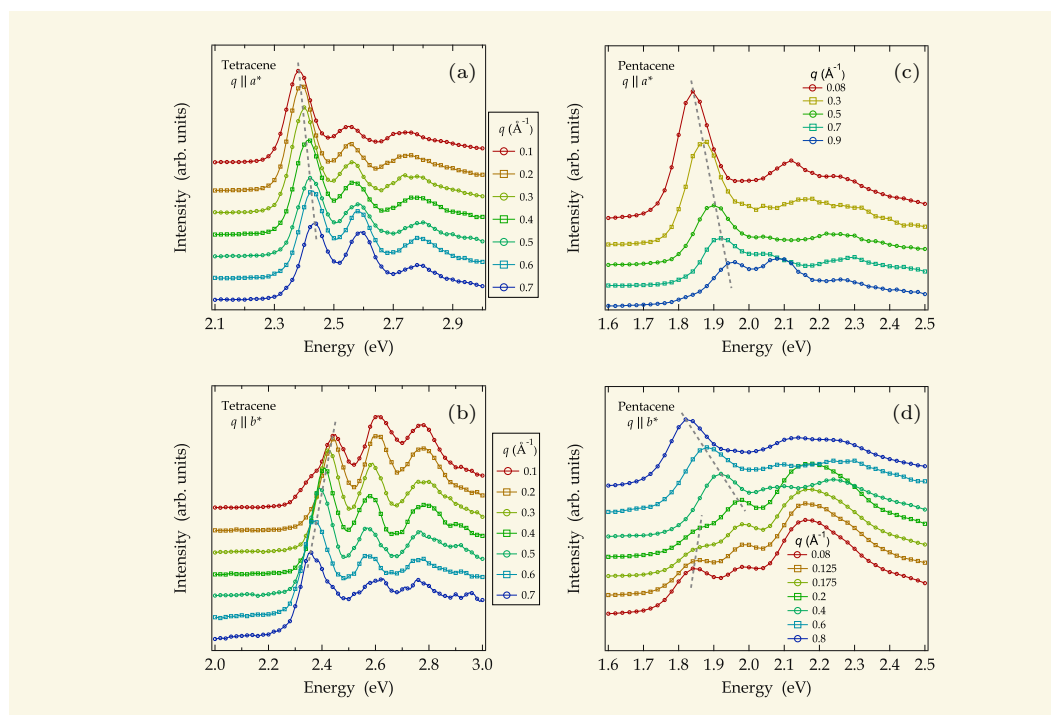


**Figure 4.15.** | Momentum dependence of the EELS spectra of solid (polycrystalline) chrysene (left panel) and picene (right panel). The measurements were carried out at  $T = 20$  K. The grey lines are intended as a guide to the eye.

is—with 48%—much larger. Such a difference must then also affect the higher lying part of the excitation spectrum, since a mixture/hybridization of Frenkel and CT states will result in two mixed states (of bonding and anti-bonding character). The resulting mixed character of these states naturally governs the spectral weight of the corresponding excitation taking into account that (most likely) the transition dipole of molecular Frenkel excitations is much larger than that of the CT transitions. Thus, in a mixed system the higher lying (former pure CT) excitation gains in intensity with increasing degree of mixture due to the Frenkel contribution in its wave function. This now harbors the explanation of the difference of the excitation spectra of tetracene and pentacene as revealed in Fig. 4.14. The interaction in tetracene is not large enough to modify the higher lying part of the spectrum visibly as compared to pure molecular excitations (as seen in solution), while in pentacene a “new” excitation feature shows up at about 270 meV above the lowest singlet exciton, and we attribute this to the anti-bonding part of the mixed Frenkel-CT system. Since both parts of the exciton wave function couple to the vibrations of the molecules, the total spectral shape of the electronic excitation spectrum becomes a complex mixture of satellites of electronic as well as vibronic origin, and a detailed analysis requires sophisticated, state-of-the-art modelling, which is beyond the scope of this thesis.

It is interesting to note that calculations based upon DFT predicted that the energetically lowest singlet excitons in pentacene have a predominant charge transfer character [173, 175, 213, 214], in good correspondence to what we have discussed above. Moreover, these DFT calculations also predict a dependence of the exciton wave function and its charge-transfer character on the length of the acene molecules [175]. However, the exact spectral shape as measured has not been reproduced by such calculations.

To get more information about these two classes of hydrocarbons we also measured the loss function with increasing momentum transfer  $q$ . As shown in Fig. 4.15, all identified excitons in chrysene and picene do not change in energy within a momentum range up to  $0.5 \text{ \AA}^{-1}$ . Consequently, in the framework of an exciton band-structure description this



**Figure 4.16.** | Loss function of single crystalline tetracene (panel a and b) and pentacene (panel c and d) as a function of momentum transfer parallel to the reciprocal lattice direction  $a^*$  as well as  $b^*$ . The gray dashed lines are intended as a guide to the eye.

yields a vanishing group velocity, with other words the excitons can be regarded as being rather localized. There are however also differences in the momentum dependence of the excitation spectra between chrysene and picene. While in the latter, one of the low lying excitations increases in spectral weight with increasing momentum transfer, which has been taken as evidence for the additional contribution of a charge transfer exciton to the spectra (see Sec. 4.2.2), this is not the case for chrysene.

Moreover, the observation of localized excitonic states in chrysene and picene is in significant contrast to what was seen for tetracene and pentacene. As depicted in Fig. 4.16 the data clearly demonstrated a strong momentum dependence of the excitons, i. e., our data provide the exciton band structure. Focussing on, e. g., pentacene, for a momentum transfer parallel to  $a^*$  (Fig. 4.16 (c)) we can observe a clear upshift of the exciton with increasing  $q$ . This upshift is accompanied by a decreasing spectral weight. The data for  $q \parallel b^*$  are more complex due to the presence of both Davydov split exciton components. At lower momentum transfers (up to  $0.2 \text{ \AA}^{-1}$ , Fig. 4.16 (d)), the lowest energy component disperses to larger energies while the second exciton does not show a significant change. Going to larger momenta the upper Davydov component disperses negatively reaching the initial energy of the lower component ( $q = 0.08 \text{ \AA}^{-1}$ ) at about  $0.8 \text{ \AA}^{-1}$ . Very similar data are observed for tetracene (Fig. 4.16 (a) and (b)).

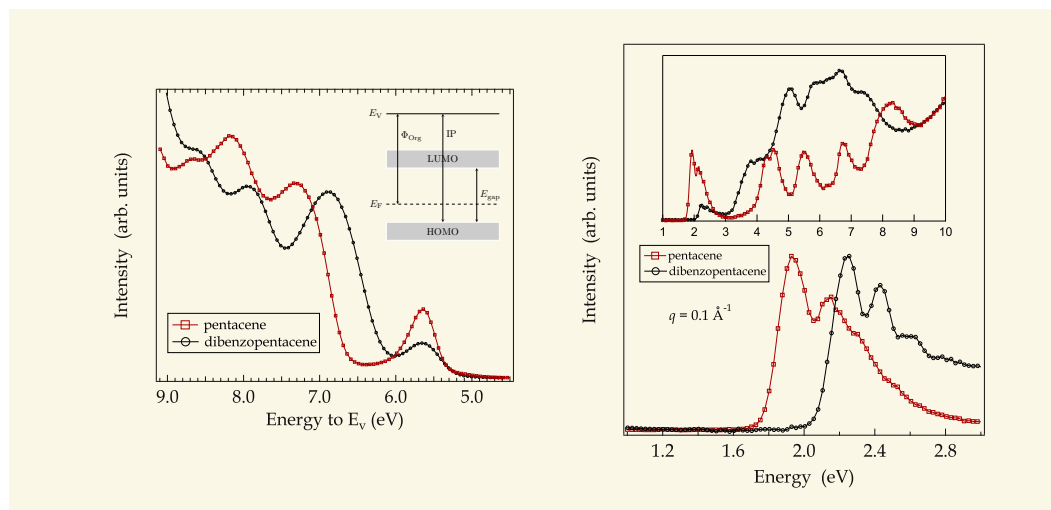
## 4.5. Electronic Properties Of Pristine 1,2:8,9-dibenzopentacene

In general, our data outline that excitons in single crystalline acenes can move coherently through the crystal giving rise to a well defined dispersion. For momentum transfers parallel to  $b^*$ , the lower Davydov component behaves analogous to the other directions, whereas the upper component seems to have a mirror-like dispersion relation. The latter is expected within a picture that relies on local excitons and their predominant nearest neighbor interaction, since the hopping matrix elements between the two different molecules in the unit cell, which thereby are mainly responsible for the exciton movement, are the same as for the Davydov splitting but enter the exciton dispersion with opposite sign. In conclusion, we emphasize that it is impossible to describe the exciton dispersion using a tight-binding approach based upon nearest neighbor interactions only, which based essentially on the description of local excitons [178, 215]. As discussed above even the dispersion of the singlet excitons and the observed Davydov splitting can only be understood when an admixture of charge transfer excitations to the lowest Frenkel-type excitons is taken into account [203]. On the basis of vibrational effects only the observed changes upon momentum variation would imply an extremely strong momentum dependence of the electron-vibration coupling, which seems rather unlikely in view of the local (intra-molecular) nature of the relevant vibrations.

At the end of the discussion in this section one can summarize that despite the fact that the molecular structure is relatively similar between acenes and phenacenes, and further, the spatial arrangement in a herringbone structure is the same in all four systems, the differences in the low energy structure are remarkable. Besides the different gap sizes as well as the evolution of the gap with increasing length of the molecule, totally different excitonic structures in both structures can be observed. These fundamental varieties in the electronic properties might be a first evidence for the differences in the physical properties observed upon alkali-metal doping. Notice that until now no superconductivity upon intercalation was observed in chrysene, but the electronic structure both of undoped and of K doped (as discussed later) is very similar to the one of picene and we can speculate that chrysene is a promising candidate for another aromatic hydrocarbon superconductor with a transition temperature between phenanthrene and picene. Furthermore, the discussion suggests that there is a kind of universal molecular length dependence of the importance of CT states in the excitation spectra for both the acenes as well as the phenacenes, since only for the longer representatives, picene and pentacene, the CT excitations modify the spectra visibly.

### 4.5. Electronic Properties Of Pristine 1,2:8,9-dibenzopentacene

1,2:8,9-dibenzopentacene represents the candidate of the “new” organic superconductors with the highest  $T_c$  of 33 K when doped with potassium. Interestingly, the molecular structure is very similar to that of pentacene. Both are characterized by a linear arrangement of five benzene rings, which share their edges, whereas in case of 1,2:8,9-dibenzopentacene two additional benzene rings are attached in a kinked manner. Nevertheless, the observation of superconductivity in case of dibenzopentacene is in contrast to the report of

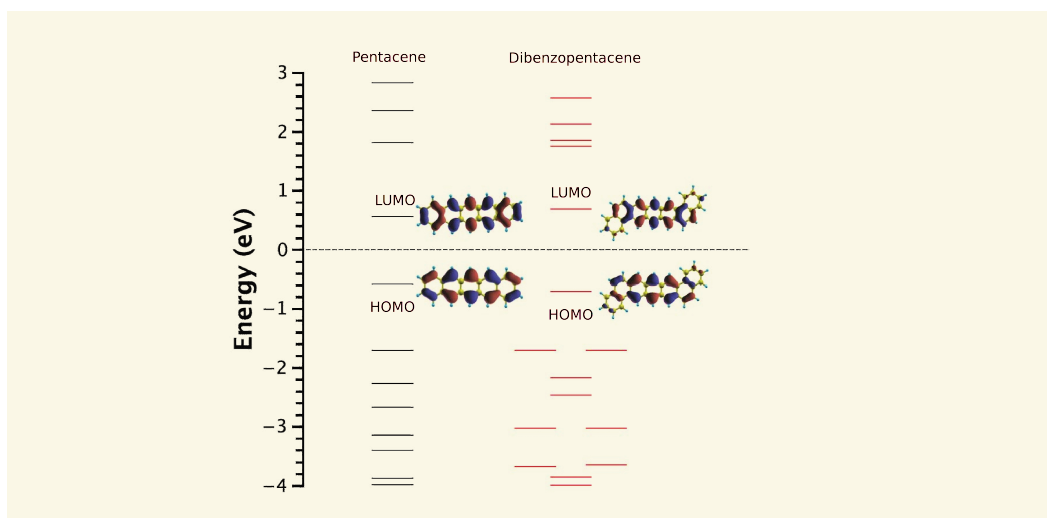


**Figure 4.17.** | Valence band photoemission profiles referenced to the vacuum level (left panel) and loss function spectra measured with EELS (right panel) of 1,2;8,9-dibenzopentacene and pentacene. The inset depicts the relevant energy parameters in such a measurement, and the given energy scale represents the ionization potentials of the respective features. In the right panel the data are normalized to the same peak height to ease comparison. The inset shows the data in a wide energy range whereby the two spectra are normalized in the high energy region between 9.5–10 eV.

a Mott insulating state for pentacene upon potassium doping [49]. Therefore the investigation of the physical properties in the undoped state is a precondition to develop a thorough understanding of the underlying electronic degrees of freedom and those states that upon doping receive the charge carriers that form the Cooper pairs responsible for superconductivity.

We start the presentation of the results with a comparison of the valence band photoemission spectra of the two investigated materials in Fig. 4.17, whereas the data of pentacene agree well with previously published results [176, 216–218]. Notice that in Fig. 4.17, the photoemission data are referenced to the vacuum level, i. e., the energy scale in Fig. 4.17 represents the ionization potential of the corresponding excitations. From the left panel of Fig. 4.17 it becomes clear that the low lying occupied electronic states of the two hydrocarbons pentacene and dibenzopentacene are very similar. Both spectra are characterized by a single feature centered at about 5.65 eV, which in both cases is well separated from the other states following at higher energies. The onset of both curves represents the ionization potential of the respective material, and we find values of 5.25 and 5.3 eV for dibenzopentacene and pentacene, respectively. The virtually identical ionization energies are qualitatively reproduced by our calculations (on individual molecules), which give values for the ionization potentials of dibenzopentacene and pentacene of 6.18 eV and 6.21 eV. The somewhat larger values from the calculation of single molecules compared to the measured ones of thin films can be rationalized taking into account screening effects by neighboring molecules in the condensed phase [91]. Moreover, the calculated electron

## 4.5. Electronic Properties Of Pristine 1,2;8,9-dibenzopentacene



**Figure 4.18.** | Calculated orbital energies as well as graphical representation of the HOMO and LUMO orbital layouts of pentacene and 1,2;8,9-dibenzopentacene.

affinities for the two molecules also are almost the same, 1.67 eV for dibenzopentacene and 1.64 eV for pentacene. Going to the higher energy features in Fig. 4.17 (left panel), we observe a difference in the energy position of the photoemission maxima, i. e., at these energies the different molecular structures have consequences for the electronic states. For pentacene, further maxima are observed at about 7.35, 8.2, and 8.7 eV, while they appear at 6.9, 7.9, and 8.7 eV for dibenzopentacene.

To get a deeper insight into the electronic structure also DFT calculations on individual, free molecules were performed by T. Hahn<sup>‡</sup> by using the NRLMOL (Naval Research Laboratory Molecular Orbital Library) program [219–223]. The electronic and optical properties for geometry optimized molecules has been calculated. The symmetry of initial and final state is of decisive character for the calculation of the possible spectral transitions. The corresponding dipole matrix element is obtained for any possible transition and the intensity of every transition is weighted with the value of this dipole matrix element. This offers a direct mapping of the spectral signals to the electronic structure of the molecule. In order to reach qualitative understanding of our experimental data a Gaussian broadening of about 0.25 meV to the theoretical spectra was applied.

Interestingly, the calculations reproduce the trend that in dibenzopentacene the higher occupied electronic levels lie closer in energy to the HOMO. This is depicted in Fig. 4.18, where the energies of the molecular orbitals as obtained in our calculations are presented. Note that there are more occupied states in dibenzopentacene than in pentacene in the energy range up to 4 eV, i. e., the relative intensity of the HOMO is smaller, as also seen in the photoemission data. The close similarity of the electronic states in the vicinity of the Fermi level as indicated by the data discussed above is further demonstrated in Fig. 4.18, where we additionally present the real space view of the HOMO and the LUMO

<sup>‡</sup>TU Bergakademie Freiberg, Department of Theoretical Physics, Leipziger Str. 23, D-09596 Freiberg, Germany

of the two molecules. In dibenzopentacene, both orbitals have a very small density on the outer two benzene rings, and moreover, their distribution otherwise is hard to distinguish from that of the corresponding orbital of pentacene. In other words, the character of the HOMO and LUMO is maintained going from pentacene to 1,2;8,9-dibenzopentacene and the interaction within the  $\pi$  states in dibenzopentacene is such that the two outer rings do hardly support the delocalization of the molecule's HOMO and LUMO orbital. This is in good agreement to the evolution of the wave function in other hydrocarbons [202] (see also discussion in previous chapter).

The close electronic similarity of dibenzopentacene and pentacene concerning the states around the energy gap is further substantiated considering the electronic excitation spectra. In the right panel of Fig. 4.17 we show a comparison of the measured loss functions of the two materials at low energies. Dibenzopentacene is characterized by an optical gap of about 2 eV which is followed by three rather weak electronic excitations at about 2.28, 2.43, and 2.62 eV. The main features of our spectrum are in good agreement with previous optical absorption measurements in solution [224–226]. However, both spectra show a very similar spectral shape at low excitation energies with a first, dominant feature that is followed by satellites. For pentacene and other acenes, such spectra have been interpreted in terms of a low lying singlet exciton of a mixed Frenkel-CT character, which is followed by a progression of vibrational satellites as well as contributions from further mixed excitons [178, 203, 227].

Due to the close similarity of the excitation spectra, we assume that qualitatively the same is true for dibenzopentacene. This is supported by previous optical absorption data of thin films of dibenzopentacene, which indicate a Davydov splitting of about 100 meV, very close to that of 115 meV for pentacene [226]. Unfortunately, the crystal structure of dibenzopentacene is unknown, which renders it impossible to consider the distance and mutual orientation of different molecules in the unit cell in more detail, in order to quantitatively describe the excitation spectra.

Furthermore, the onset of the excitation spectra differs by about 0.3 eV, which also is in good agreement to previous optical data of thin films as well as measurements in solution [226]. At first glance, this could signal a somewhat larger energy gap for dibenzopentacene. From our calculations of individual molecules we would infer an energy gap that is slightly smaller for dibenzopentacene (by about 0.06 eV). On the other hand, electronic excitations in molecular crystals are excitons with a significant binding energy, which could also be somewhat different for the two materials due to different crystal arrangements or distances that control the screening of Coulomb interactions in the material. Consequently, the spectral onset in the electronic excitation data as shown in Fig. 4.17 (right panel) represents a lower limit for the energy gap of dibenzopentacene and pentacene but further investigations are necessary, in particular an accurate experimental determination of the energy gap of dibenzopentacene. The close similarity of the low energy excitation spectra of the two materials is a direct consequence of the fact that both the HOMO and LUMO wave functions are very similar (see Fig. 4.18). This is corroborated by our theoretical analysis of the excitation spectra, which yield an assignment of the



## 4.5. Electronic Properties Of Pristine 1,2:8,9-dibenzopentacene

---

lowest singlet excitation to an almost pure HOMO-LUMO transition with negligible contributions from other, higher energy transitions.

At higher energies (above 3 eV) the excitations of dibenzopentacene and pentacene are different as also shown in Fig. 4.17, as one would expect since the two additional benzene rings in dibenzopentacene must have consequences for the electronic excitations in general. The presence of more  $\pi$  states also explains the generally larger intensity of the electronic excitations in dibenzopentacene at energies between 3 and 7 eV. Interestingly, the energy distance between the lowest excitation and the following one in energy is about 0.4 eV smaller for dibenzopentacene, which is in good correspondence to the results from our photoemission studies and calculations, which signal a smaller distance of the electronic states in dibenzopentacene. This—in turn—also results in a downshift of the respective excitations.

Finally, we are left with the surprising contrast that although dibenzopentacene and pentacene are characterized by very similar electronic degrees of freedom, their behaviour upon doping with potassium seems to be radically different as mentioned at the beginning of this section [49, 144]. This indicates that also in the new potassium doped hydrocarbon superconductors electronic correlations are not negligible and have to be considered to fully understand their electronic behaviour. Molecular crystals in general are materials with rather narrow energy bands, which is a direct result of the relatively weak interaction between the individual molecules in the crystal. The band width in many cases is comparable to the repulsion of two charge carriers brought onto a molecule, i. e., molecular crystals can be regarded to be correlated materials [51, 171, 228]. Metallic and insulating phases are indeed known from the alkali-metal-intercalated  $C_{60}$  materials, where small changes in the crystal structure induce a metal insulator transition to a Mott ground state [229–232]. For aromatic hydrocarbons such as picene and coronene crystals, it was also been discussed that electronic correlation effects play an important role and that these crystals when doped with three potassium atoms per molecule are close to a metal-insulator transition into a Mott insulating phase [134, 149, 233]. It remains to be seen, what the exact role of these electronic correlations is for hydrocarbon crystals, and further work is necessary to gain deeper insight into their importance in different crystals.





*“Research is to see what others have seen and to think what no else has thought.”*

Albert Szent-Gyorgi\*

# 5

## Results Part II: EELS On Potassium Doped Aromatic Hydrocarbon Systems

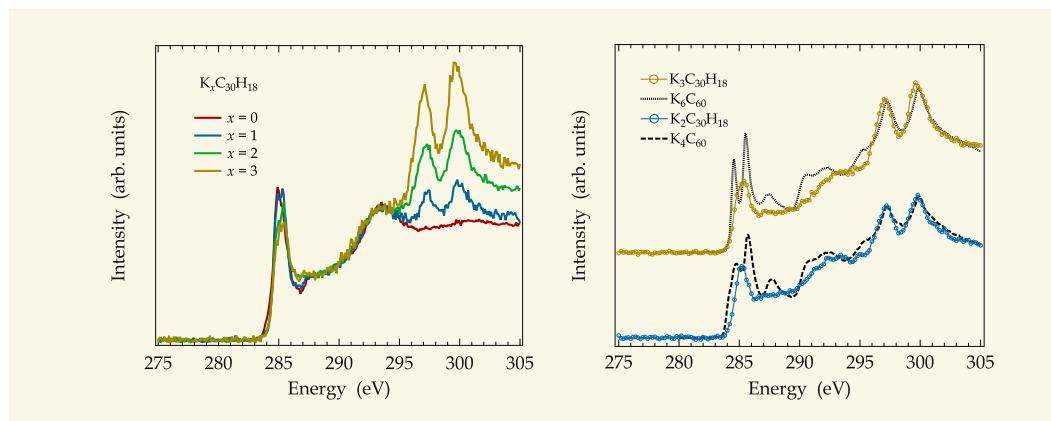
**A**FTER the detailed description of the ground state of several selected aromatic hydrocarbon systems in the previous chapter, further investigations are required in order to develop a deeper understanding of the superconducting state, especially superconductivity only occurs when alkali metals (e. g., potassium) are intercalated in the systems. Therefore, it is necessary to study the doping introduced changes in the electronic structure. Apart from the introduction of charge carriers, the addition of potassium can also lead to stable phases with particular stoichiometries. A very important prerequisite for detailed studies as well as the understanding of physical properties is the knowledge about such phases and their existence and stability regions. For instance, the physical properties and the conclusive analysis of experimental data of alkali metal doped fullerenes have demonstrated to be strongly dependent on the existing phases and their characterization [10, 234–238].

### 5.1. Evidence For Phase Formation In K Intercalated 1,2;8,9-dibenzopentacene

The amount of potassium in our doped dibenzopentacene films was determined using core level excitation spectra. In Fig. 5.1 (left panel) we show C 1s and K 2p core level excitations of undoped and potassium doped dibenzopentacene. These data can be used to analyze the doping induced changes of the potassium doped films. All spectra were normalized at the step-like structure in the region between 291 eV and 293 eV, i. e., to the  $\sigma^*$  derived intensity, which is proportional to the number of carbon atoms. For the undoped case,

---

\*Albert Szent-Gyorgi (1893-1986). Hungarian physiologist who won the Nobel Prize in Physiology or Medicine in 1937.



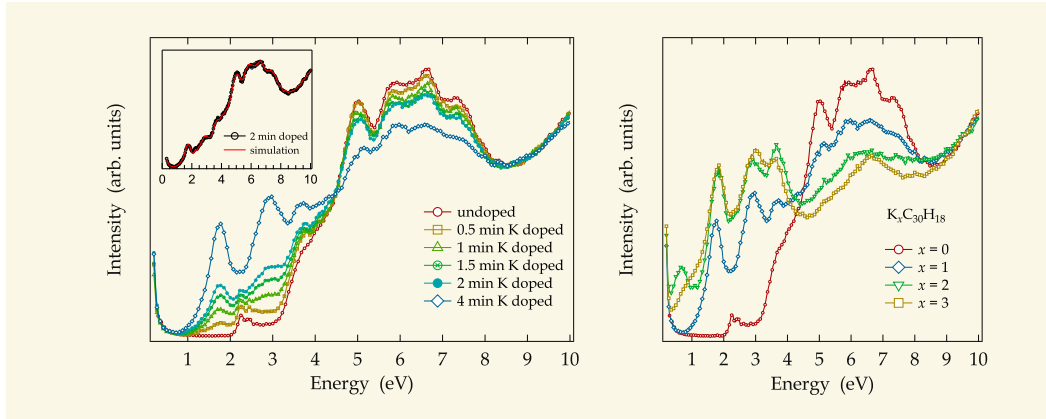
**Figure 5.1.** | Left panel: C 1s and K 2p core level excitations of  $K_x(1,2;8,9\text{-dibenzopentacene})$  for  $x=0, 1, 2, 3$ . Right panel: Comparison between the K 2p core level excitations of 1,2;8,9-dibenzopentacene and  $C_{60}$  for different doping stages.

we can clearly identify a sharp and strong feature in the range between 283 and 286 eV, which can be assigned to transitions into  $\pi^*$  states representing the unoccupied electronic states. The step-like structure above 291 eV corresponds to the onset of transitions into  $\sigma^*$ -derived unoccupied levels. By doping the sample with potassium, the spectrum is still dominated by a sharp excitation feature right after the excitation onset at 283 eV and, in addition, by K 2p core excitations, which can be observed at 297.2 and 299.8 eV, and which can be seen as a first evidence of the successful doping of the sample. Importantly, a reduction of the spectral weight of the first C 1s excitation feature is observed in the left panel of Fig. 5.1 upon doping, which can be seen as a further signal of successfully doping because it represents the filling of the conduction band. The stoichiometry analysis can be substantiated by comparing the K 2p and C 1s core excitation intensities in comparison to other doped molecular films with well known stoichiometry, such as  $K_4C_{60}$  or  $K_6C_{60}$ <sup>‡‡</sup>(cf. right panel of Fig. 5.1) [46]. The results shown in the Fig. 5.1 indicate three different doping levels with  $K_1C_{30}H_{18}$ ,  $K_2C_{30}H_{18}$  and  $K_3C_{30}H_{18}$  composition, which are discussed in more detail in the following.

Initial potassium addition to dibenzopentacene causes major changes in the electronic excitation spectrum as revealed in Fig. 5.2 (left panel), where we show a comparison of the spectra in an energy range of 0-10 eV for different doping steps. These data are taken with a small momentum transfer  $q$  of  $0.1 \text{ \AA}^{-1}$ . During potassium addition, the dibenzopentacene films have been kept at room temperature.

For undoped dibenzopentacene, we can clearly identify maxima at about 5, 5.9, 6.6, and 7.3 eV as well as a broad shoulder at about 3.75 eV, which are due to excitations between the occupied and unoccupied electronic levels (see Sec. 4.5). Upon initial doping, the

<sup>‡‡</sup>In case of potassium doped  $C_{60}$  the knowledge of the phase diagram displays the precondition for the production of phase-pure fullerides [239], which can be afterwards characterised by, e. g., elastic scattering and represent therefore a very good reference for the determination of the stoichiometry of new intercalated samples.



**Figure 5.2.** | Left panel: Evolution of the loss function of dibenzopentacene in the range of 0 - 10 eV upon potassium doping measured with a momentum transfer of  $q=0.1 \text{ \AA}^{-1}$ . All spectra were normalized in the high energy region between 9 - 10 eV. (K content increases from bottom to top). The inset shows a simulation of the 2 min doped spectra as a superposition of 55% of the undoped spectra and 45% of the 4 min doped spectra. Right panel: Comparison of the loss function for different achieved doped phases.

spectral features become broader. The low energy structures representative of undoped dibenzopentacene decrease in intensity while three new peaks become visible at 1.76, 2.93, and 3.7 eV. The latter steadily increase with doping until a particular doping level (labelled with 4 min K doped in Fig. 5.2) is reached. Most importantly, all spectra in the series as shown in the left panel of Fig. 5.2 can be simulated by a corresponding superposition of the spectra of undoped and 4 minutes doped dibenzopentacene. This is demonstrated in the inset in Fig. 5.2, where we show a comparison of the spectrum of a 2 min doped film and a superposition of the two spectra of undoped and 4 min doped dibenzopentacene weighted by 0.55 and 0.45, respectively. In addition, further potassium addition causes qualitative changes of the spectral shape, in particular the appearance of a new feature at 0.65 eV (see right panel of Fig. 5.2). Consequently, these two facts strongly indicate the formation of a potassium doped dibenzopentacene phase, and our core level measurements signal that we reached a doping level of  $x = 1$ . Interestingly, this  $K_1$  dibenzopentacene is stable up to  $100^\circ\text{C}$ , i. e., heating up the sample to this temperature did not induce visible changes in the valence band as well as in the core level spectra. Increasing to  $150^\circ\text{C}$  however resulted in a loss of potassium from the films indicated by a reduction of the excitation feature at 1.76 eV. In regard of the electronic ground state of the phase with  $K_1$  dibenzopentacene composition, the data in Fig. 5.2 indicate an energy gap of about 0.9 eV, i. e., this  $K_1$ -phase is insulating.

Starting from the above discussed phase ( $K_1$  dibenzopentacene) and adding further potassium while the films are kept at room temperature leads to a second doped phase, which is characterized by the additional peak in the electronic excitation spectrum at 0.65 eV, and which, according to our core level analysis, has a stoichiometry of  $K_2$  dibenzopentacene. Moreover, adding more potassium at this stage leads to the formation

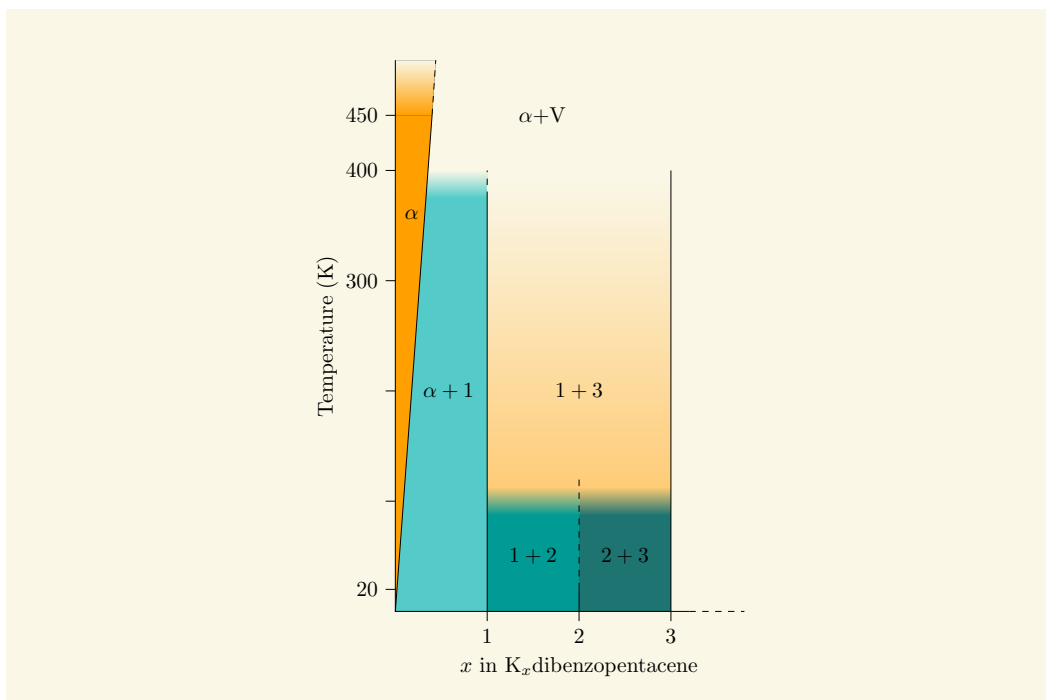
of a potassium overlayer on our films as signalled by the appearance of the charge carrier plasmon excitation of metallic potassium at 3.75 eV. This indicates that there is no further diffusion of potassium into a film with  $K_2$ dibenzopentacene composition at room temperature. Intriguingly, keeping the films at room temperature in our ultra high vacuum chamber results in a loss of potassium after several minutes as signalled by a loss of the spectral weight around 0.65 eV, i. e., potassium diffuses out of the film. Cooling a  $K_2$ dibenzopentacene film down to 20 K, however, allows to keep the composition stable for at least 15 hours. Again spectra with intermediate composition can be well simulated by the superposition of the spectra of  $K_1$ dibenzopentacene +  $K_2$ dibenzopentacene.

To summarize at this point, we prepared two potassium doped phases of dibenzopentacene,  $K_1$ dibenzopentacene and  $K_2$ dibenzopentacene, which can be obtained by potassium addition at room temperature under UHV conditions and which are well distinguished by corresponding features in the electronic excitation spectra. The temperature stability of these two phases is rather different since the former can be heated to about 100 °C without noticeable changes while the latter is only stable at very low temperatures (20 K).

However, the observation of superconductivity was reported for samples with even higher doping levels, between  $x = 3$  and 3.5. In order to realize such high doping levels, we had to change our doping procedure. In detail, we heated up the films during potassium addition (which lasted 15 minutes) to temperatures of 60 - 80 °C, and we annealed the films after each doping step at 80 °C for about 15 minutes. Finally, at least three doping and annealing cycles were necessary to identify clear changes in the electronic excitation spectra as revealed in Fig. 5.2 (right panel). The feature typical for  $K_2$ dibenzopentacene at 0.65 eV disappears and instead a shoulder centered at 0.85 eV shows up. Furthermore, there are slight changes in the double peak structure at 2.93 and 3.7 eV. Our measurements of the C 1s and K 2p core level excitations display a doping level of  $x \approx 3$  (cf. Fig. 5.1). The necessary annealing during and after potassium addition clearly signals, that potassium diffusion into the dibenzopentacene films requires much higher activation energies at higher doping levels. Interestingly, the observation of superconductivity in samples with about three potassium atoms per dibenzopentacene molecule [144] was made after long time annealing of the doped samples which also indicates hindered potassium diffusion at room temperature.

Similar to what we observed for the  $K_1$ dibenzopentacene phase, our films with a  $K_3$ dibenzopentacene composition also are stable at 100 °C for more than 15 hours. Further, higher temperatures (150 °C) again result in a loss of potassium from the films, and we observe spectral changes towards the spectral shape of  $K_1$ dibenzopentacene. Consequently, this implies a potassium binding energy that is rather similar for these two potassium doped dibenzopentacene phases.

Finally, the excitation spectra for the  $K_2$ - and the  $K_3$ -phase do not show clear evidence for an energy gap in contrast to what is observed for  $K_1$ dibenzopentacene. Also, measurements with higher momentum transfer do not show the opening of a band gap. This could be taken as evidence for a metallic ground state of these phases, in agreement with the observation of a superconducting phase at higher doping levels [144]. However, the



**Figure 5.3.** | Provisional phase diagram of  $K_x(1,2;8,9\text{-dibenzopentacene})$  for  $x$  up to 3. In mixed phase regions, the corresponding phases are denoted by their  $x$  value, V stands for potassium vapour.

presence of the elastic line in our spectra does not allow the determination of the true ground state, whether metallic or insulating. In general, the doping induced excitation at about 1.76 eV could be interpreted as a transition from the now filled LUMO of dibenzopentacene to the LUMO+1 level. The lowest energy feature around 0.65 eV then could be interpreted as a charge carrier plasmon of the metallic phases. On the other hand, recent photoemission investigations of potassium doped picene and coronene, two other recently reported superconductors, were not able to identify any metallic doped phase, which might be related to the importance of electron-electron correlation effects [240]. Given these facts, further work is required in order to unambiguously demonstrate well defined and well characterized metallic phases of doped hydrocarbon molecular solids. As a consequence we can summarize the doping induced changes in valence band as well as core level excitations, and the temperature dependence of the measured spectra in a provisional phase diagram as depicted in Fig. 5.3. This schematic diagram also includes a solid solution of potassium in the dibenzopentacene films denoted  $\alpha$ , which would form first upon doping. We note that all our experiments have been carried out at a pressure of about  $10^{-10}$  mbar, and that the temperatures as given in Fig. 5.3 do not represent the atmospheric pressure behavior. Furthermore, film growth and doping by deposition from the vapour phase is characterized by the interplay between thermodynamics and kinetics,

which can be nicely seen by the annealing steps that are necessary to achieve a doping level of  $K_3$ dibenzopentacene.

Hence, the previous discussions signal that the phase stability in dibenzopentacene is rather complicated, it is obvious that informations on phases and electronic structure of such compounds are strongly needed. Unfortunately, we were not able to perform similar experiments for the other hydrocarbons investigated in this thesis, e. g., picene or coronene. The reason for this is the different sublimation temperature of such systems under UHV conditions. For shorter molecules, such as picene, annealing results directly in a loss of material, which influences the findings especially the stoichiometry and therefore the core level excitations. In case of picene, coronene etc. we doped the system until no significant changes were observed in the spectra and a saturated and fully intercalated phase was attained. Furthermore, superconductivity was only observed in all four compounds (phenanthrene, picene, coronene, and 1,2;8,9-dibenzopentacene) after a doping level of about 3 was reached. The following discussion describes the main difference between the undoped and the  $K_3$ -phase, which provides evident arguments to elucidate the nature of the superconducting state.

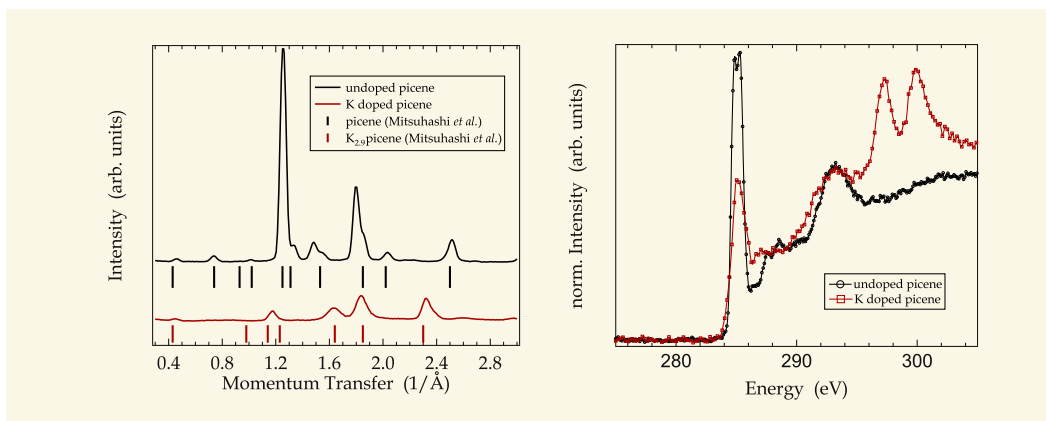
## 5.2. Electronic Structure Of Potassium Doped Picene

We start our discussion of the changes, which occur upon potassium addition, with an analysis of the elastic scattering spectra. In the left panel of Fig. 5.4 we show representative electron diffraction profiles of undoped and potassium doped picene films. An analysis of the diffraction peaks of undoped picene with calculated positions based on the known crystal parameters reveals that our films consist mostly of crystallites with their  $a^*, b^*$ -plane parallel to the film surface (see also Sec. 4.2). The diffraction profile can be well reproduced with the x-ray diffraction pattern of pristine picene from Ref. 129 indicated by black ticks below the curve (note that the x-ray diffraction pattern represents all three directions in contrast to our  $a^*, b^*$ -textured films). Upon potassium doping the diffraction profile drastically changes. The diffraction peaks at about 1.25, 1.48, 2.05, and  $2.52 \text{ \AA}^{-1}$  disappear, instead some new peaks around 1.18, 1.63, and  $2.31 \text{ \AA}^{-1}$  are observed. This observation is in very good agreement with the published x-ray diffraction pattern for  $K_{2.9}$ picene. In our studies, further doping does not change the elastic scattering profile substantially, which indicates that our preparation procedure a doped phase with a stoichiometry close to  $K_3$ picene. The addition of more potassium results in the formation of a metallic K overlayer on our films.

To be able to further analyze the doping induced changes, we additionally measured the C 1s and K 2p core excitation edges. These data, as mentioned in the previous section, can be used to determine the stoichiometry of the potassium doped picene films. Figure 5.4 (right panel) shows the C 1s and K 2p core excitations for potassium doped picene in comparison to those of pure picene. Both spectra were normalized in the region between 291 and 293 eV. For the undoped case, we can clearly identify a sharp and strong feature in the range between 284–286 eV, and some additional broad features at 289 and 293 eV. Again



## 5.2. Electronic Structure Of Potassium Doped Picene

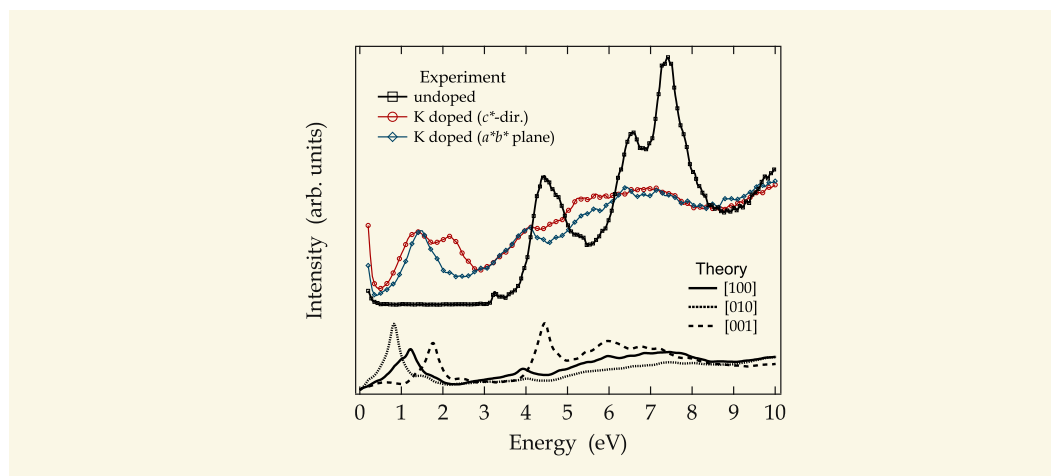


**Figure 5.4.** | Left panel: Comparison of the elastic diffraction profiles of solid picene for the undoped (black/upper curve) and potassium doped (red/lower curve) case. The ticks below the curves indicate the positions of the x-ray diffraction peaks as reported in Ref. 129. Right panel: C 1s and K 2p core level excitations of undoped and potassium doped picene.

below  $\sim 290$  eV the structures can be assigned to transitions into  $\pi^*$  states representing the unoccupied electronic states. The fine structure of the low lying, predominant feature was discussed in Sec. 4.2. Above 290 eV the spectral weight is dominated by C 1s- $\sigma^*$  transitions. Also in the case of potassium doped picene the data still reveal some fine structure, which demonstrates the molecular derived nature of the electronic states. Again, the spectrum is dominated by a sharp excitation feature right after the excitation onset at 284 eV and, in addition, by K 2p core excitations, which can be observed at 297.2 and 299.8 eV. The step-like structure at about 287 eV, which can be clearly seen in the undoped case, is not observed. Importantly, a clear reduction of the spectral weight of the first C 1s excitation feature by a factor of about 0.62 is observed in Fig. 5.4 upon doping. Taking into account the four conduction bands that contribute to this intensity in the undoped case, this reduction is a clear signal for the successful doping and it can be used to analyze the doping (filling) level of the conduction bands. We thus arrive at a filling of these four levels by three electrons, which is in a very good agreement to our stoichiometry analysis of  $\text{K}_3\text{picene}$  (cf. below) and the fact that each potassium provides its outer s-electron for the doping process.

A similar stoichiometry analysis by comparing the K 2p and C 1s core excitation intensities with other doped molecular films with known stoichiometry, as described in Sec. 5.1, indicates a doping level of  $\text{K}_{2.8}\text{picene}$ , which again is in very good agreement to the other results discussed above.

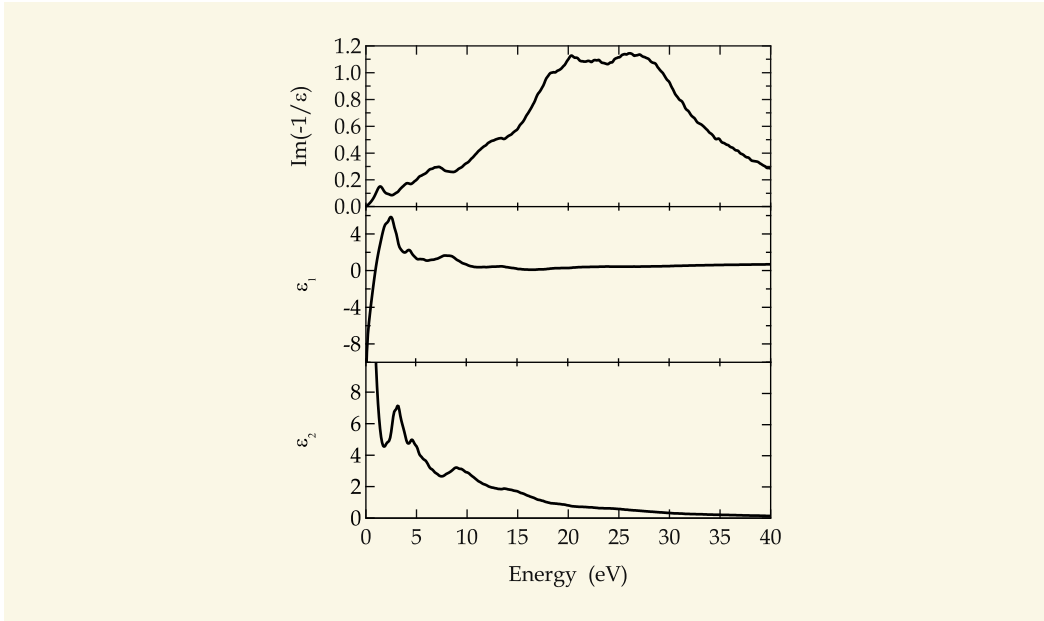
Doping of picene also causes major changes in the electronic excitation spectrum as revealed in Fig. 5.5 (upper part), where we show a comparison of the loss functions in an energy range of 0-10 eV taken with a small momentum transfer  $q$  of  $0.1 \text{\AA}^{-1}$ . For undoped picene, as discussed in the previous chapter, we can clearly identify maxima at about 3.3, 4.6, 6.4, and 7.3 eV, which are due to excitations between the occupied and unoccupied



**Figure 5.5.** | Comparison of the loss function in the range of 0-10 eV for undoped (black squares) and K intercalated picene (blue diamonds for the sample with predominant  $a^*b^*$  orientation and red circles for the film with a high amount of molecules oriented along the  $c^*$  axis). Furthermore, a comparison with the theoretical loss function, calculated within the RPA, for the three fundamental directions [100], [010] and [001] is shown in the lower part [151].

electronic levels. Upon doping, the spectral features become broader, and a downshift of the major excitations can be observed. We assign this downshift to a relaxation of the molecular structure of picene as a consequence of the filling of antibonding  $\pi^*$  levels. The reason for the spectral broadening is unclear at present. We can only speculate that it might be connected to a reduced life time of the electronic excitation in the metallic state and/or to the formation of a doped sample with very small grain sizes. In addition, for the doped films a new structure at about 1.5 eV is observed in the former gap of picene in case of samples with predominantly  $a^*, b^*$  orientation, whereas in case of films with a considerable number of crystallites having their  $c^*$ -axis on the film surface, a well separated two peak structure with maxima at 1.5 and 2.15 eV can be identified. Furthermore, A. Rubio and coworkers calculated the loss function for doped picene based on DFT in the local-density approximation. A precondition for the calculation is the knowledge of the accurate positions of the intercalated atoms. Unfortunately, the crystal structure of potassium-intercalated picene is not fully known experimentally until now. Therefore, they used the crystal structure calculated previously, in which potassium atoms are in intralayer positions [145]. Surprisingly, the calculated effects of potassium doping on the EELS spectra of picene are in a very good agreement with our measured spectra. Apart from the broadening of all the sharp spectral features and the downshift due to the reduction of the gap between bands deriving from HOMO and LUMO states of picene, in all polarization directions appears a new peak at low energy. This peak, which is linked to metallicity in  $K_3$ picene, is a signature of a plasmon excitation, as it can be inferred from a zero crossing of the real part of the dielectric function at the energy of the peak. With the

## 5.2. Electronic Structure Of Potassium Doped Picene



**Figure 5.6.** | Loss function ( $\text{Im}(-1/\epsilon)$ ), real part ( $\epsilon_1$ ) and imaginary part ( $\epsilon_2$ ) of the dielectric function of K doped picene. The momentum transfer is  $q=0.1 \text{ \AA}^{-1}$ . Note that in contrast to Fig. 5.5, the loss function is corrected for the contribution of the direct beam.

knowledge of the calculations we can determine that the admixture of crystallites with their  $a^*$ - as well as  $b^*$ -axes parallel to the sample surface to films with predominant  $c^*$  orientation is not negligible, as seen as an excitation feature at the same energy for both samples. Hence, the following discussion focusses only on predominantly excitations with a polarization in the  $a^*, b^*$  crystal plane.

To obtain deeper insight into these variations, we have analyzed the measured loss function,  $\text{Im}(-1/\epsilon)$ , of doped picene using a KKA, similar to the procedure described in Sec. 4.2.1. In contrast to the analysis of the spectra of undoped picene the elimination of contributions of the direct beam have been done by fitting the plasmon peak with a model function [241]. The results of this analysis are shown in a wide energy range in Fig. 5.6. The loss function (upper panel) is dominated by a broad maximum in the range between 20-25 eV which can be assigned to the  $\pi + \sigma$  plasmon, a collective excitation of all valence electrons in the system. Moreover, the maxima between 25-30 eV correspond to the K3s absorption edge. Various interband excitations at 2-20 eV can be observed as maxima in the imaginary part of the dielectric function,  $\epsilon_2$  (lower panel). Most interestingly, the new low energy excitation at about 1.5 eV in the loss function is not represented by a maximum in  $\epsilon_2$ , but by a zero crossing near 1.4 eV in the real part of the dielectric function,  $\epsilon_1$ . Therefore, this spectral feature represents a collective excitation (density oscillation), and we assign it to the charge carrier plasmon of doped picene.

As mentioned above the consistency of our KKA can be tested by an evaluation of the sum rules for the loss function and the dielectric function after our KKA (see Eq. 2.28),

which results in a very good agreement of the two values with an error of less than 1.5%. Furthermore, these values are also in good correspondence to what is expected from a calculation of the electron density of doped picene, whereby we find a deviation of 7% only (with  $N = 258$  electrons per unit cell is the electron density in the case of  $K_3$ picene). For metallic systems a further sum rule, independent of the plasma frequency, can be employed (cf. Eq. 2.29), which allows an additional check of our analysis. Here, after our KKA we arrive at a value of 1.55, very close to the expectation of  $\pi/2$ .

To elucidate all the observations further, we show in Fig. 5.7 the optical conductivity  $\sigma$  of doped picene. The optical conductivity is directly proportional to the matrix element weighted joint density of states of the corresponding excitation. As revealed by Fig. 5.7,  $\sigma$  consists of a free electron contribution at low energies due to intraband transitions in the conduction bands and some additional interband contributions. To obtain a more detailed picture and to separate intraband and interband contributions, we have fitted the optical conductivity in the range between 0-30 eV using a simple Drude-Lorentz model introduced in Sec. 2.3.1

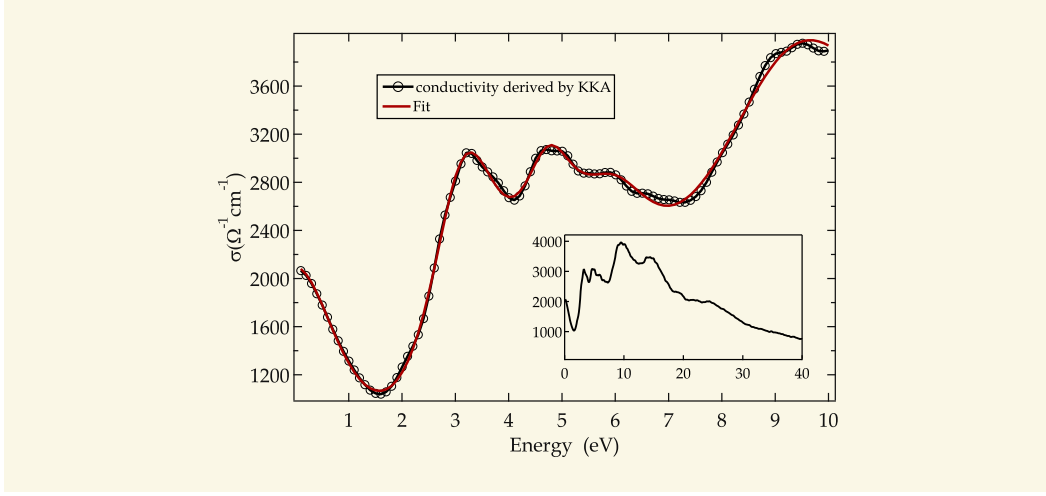
$$\epsilon(\omega) = 1 - \frac{\omega_D^2}{\omega^2 + i\gamma_D\omega} + \sum_j \frac{f_j}{\omega_{j_0}^2 - \omega^2 - i\gamma_j\omega}. \quad (5.1)$$

The Drude (charge carrier) part ( $\omega_D, \gamma_D$ ) describes the free electron contribution and the Lorentz oscillators ( $f_j, \gamma_j$  and  $\omega_{j_0}$ ) represent the interband transitions. The resulting fit parameters are given in Table 5.1 and the fit is shown in Fig. 5.7. This Figure demonstrates that our model description of the data is very good. We note, that the result of our fit also describes the real part of the dielectric function very well, which demonstrates the consistency of our description.

**Table 5.1.** | Parameters derived from a Drude-Lorentz fit of the optical conductivity of K doped picene (as shown in Fig. 5.7) using Formula 5.1 for  $K_3$ picene. The Drude part is given by the plasma energy  $\omega_D$  and the width of the plasma (damping)  $\gamma_D$ , while  $f_j$ ,  $\gamma_j$  and  $\omega_{j_0}$  are the oscillator strength, the width and the energy position of the Lorentz oscillators.

i	$\omega_{j_0}$ (eV)	$\gamma_j$ (eV)	$f_j$ (eV)	$\gamma_D$ (eV)	$\omega_D$ (eV)
1	2.05	0.15	0.31	1.14	4.22
2	3.22	1.83	5.74		
3	4.77	1.44	3.79		
4	6.01	2.16	4.34		
5	9.53	4.94	10.62		
6	14.75	6.85	10.49		
7	24.53	16.39	13.09		

## 5.2. Electronic Structure Of Potassium Doped Picene



**Figure 5.7.** | Optical conductivity  $\sigma = \omega\epsilon_0\epsilon_2$  of K doped picene for a momentum transfer of  $q = 0.1 \text{ \AA}^{-1}$  (black circles) derived by a KKA of the loss function. Additionally, the result of a Drude-Lorentz fit is shown (red line). The inset shows the optical conductivity in a larger range up to 40 eV.

We arrive at an unscreened plasma frequency  $\omega_D$  of about 4.2 eV, which now can be compared to the expectation value for this plasma frequency taking into account the six conduction electrons per unit cell (2 picene molecules per unit cell) in  $K_3$ picene:

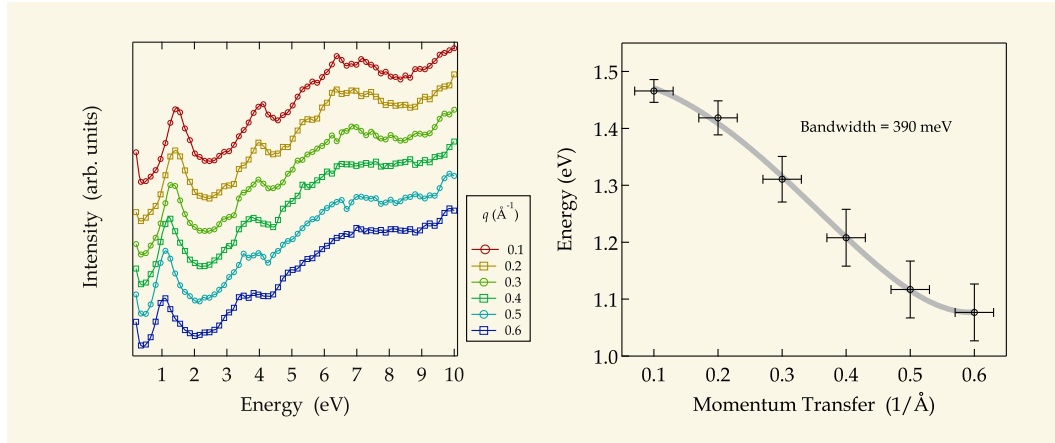
$$\hbar\omega_D = \sqrt{\frac{ne^2}{\epsilon_0 m_0}} = 3.52 \text{ eV.}$$

This value is somewhat lower than what we have derived using our fit procedure. This might be related to an effective mass of the charge carriers in doped picene, which is reduced as compared to the free electron value,  $m_0$ . For related (undoped) organic crystals such as rubrene [242], PTCDA [243, 244] or pentacene [245] an effective mass also lower than  $m_0$  has been deduced.

Finally, the difference between the (unscreened) plasma frequency as obtained in our fit and the observed (screened) value that can be read off the loss function (about 1.5 eV) or the zero crossing of the real part of the dielectric function (about 1.4 eV), can be described by a background dielectric constant  $\epsilon_\infty$ , which effectively describes the screening of the plasma oscillations due to all higher lying electronic excitation of the system. This results in:

$$\epsilon_\infty \sim \left(\frac{4.22}{1.45}\right)^2 \sim 8.5$$

Surprisingly, this value is significantly larger than the static dielectric constant of undoped picene, where we derived a value of 3-3.5 (see Sec. 4.2.1). In other words, the screening



**Figure 5.8.** | Left panel: The momentum dependence of the EELS spectra of K intercalated picene ( $q$  is increasing from top to bottom spectra). Right panel: Plasmon dispersion in K doped picene with a bandwidth of  $\approx 390$  meV in the considered momentum range. The gray curve represents the fit with a polynomial function.

ability of doped picene seems to be much larger than that of the parent compound, whereas such a dramatic change in the background dielectric constant is for instance not observed going from undoped to doped  $C_{60}$  [246–248]. It is tempting to relate this increased screening ability to the appearance of superconductivity, since the pairing of charge carriers has to overcome their mutual Coulomb repulsion, but this issue certainly needs further investigations from both, experiment and theory to be settled.

In order to obtain a more detailed picture of the charge transfer plasmon in K doped picene we measured the loss function with increasing momentum transfer  $q$ . As one can see in Fig. 5.8 (left panel) the doping introduced charge carrier plasmon clearly disperses to lower energies with increasing  $q$ . For the purpose of further quantifying the behavior of the 1.5 eV plasmon we present in Fig. 5.8 (right panel) the evolution of the peak position in the range between 0.1–0.6  $\text{\AA}^{-1}$ . Due to the strong beam damage effects in these organic solids (cf. Sec. 4.1) and the low cross section for higher momentum transfers, data for a momentum transfer above 0.6  $\text{\AA}^{-1}$  are not included in Fig. 5.8. It can be seen that the plasmon dispersion in  $K_3$ picene is obviously negative with a bandwidth of at least 390 meV. This is in contrast to what one would expect for an “ordinary” metallic plasmon, where the dispersion should be positive and quadratic [18, 249, 250]. In order to investigate the long-wavelength limit of the plasmon dispersion in potassium intercalated picene in more detail, we fitted the dispersion curve using a polynomial function

$$\omega(q) = \omega_p + Aq^2 + Bq^4.$$

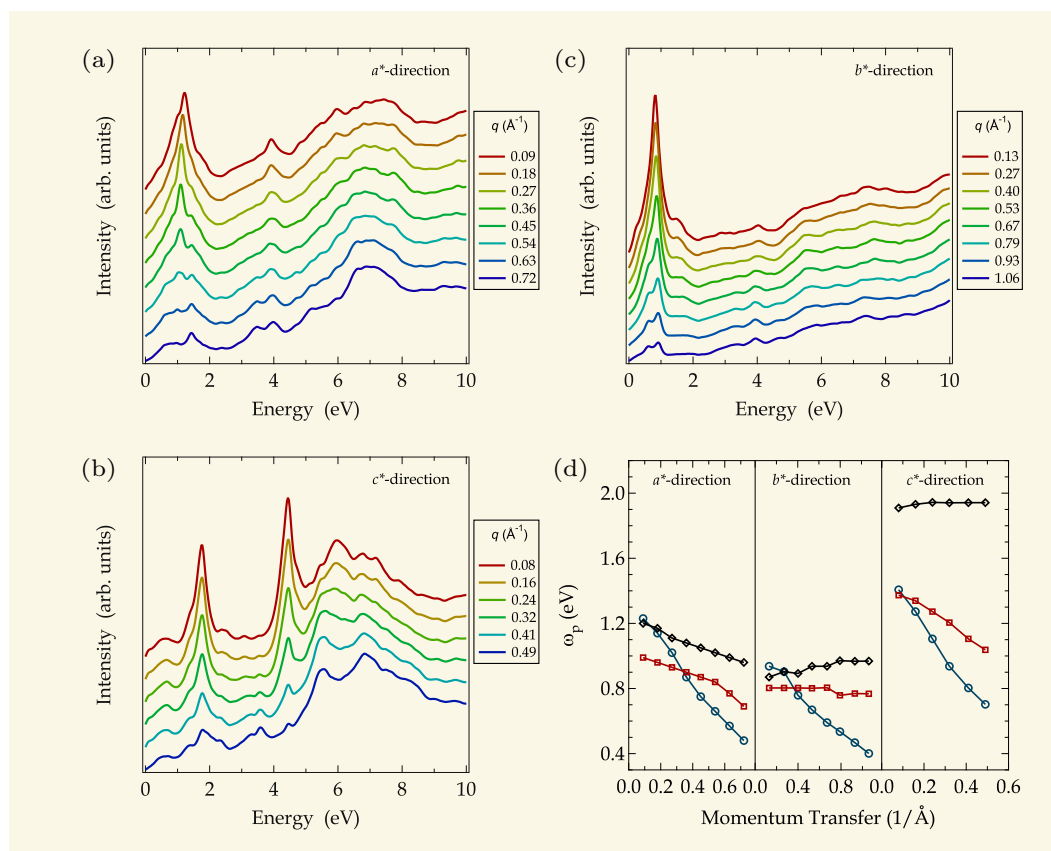
The parameter  $A$  then represents the plasmon behavior for small momenta, i. e., long wavelengths. This fit provides us with the following results (see also Fig. 5.8 left panel):  $\hbar\omega_p = (1.495 \pm 0.006)$  eV,  $A = (-2.296 \pm 0.093)$  eV $\text{\AA}^2$  and  $B = (3.146 \pm 0.247)$  eV $\text{\AA}^4$ . This result is

## 5.2. Electronic Structure Of Potassium Doped Picene

in a very good agreement with the value estimated from the Drude-Lorentz fit of  $\sigma$  and further only less than 15% higher than the value provided by the calculation of the plasma frequency based on the six conduction electrons. In conclusion, the long-wavelength limit of the plasmon dispersion can be well rationalized within an RPA-like description of simple metals. However, the negative slope of the dispersion cannot be justified within the framework of a simple metal. Deviations from the expectation of a quadratic plasmon dispersion have already been reported in the past. Already the heavier alkali metals show vanishing or even negative plasmon dispersions, which has initiated a lot of theoretical work [251]. Over the years different reasons for these observations have been discussed including local field effects, interband transitions and the anisotropy of the effective mass. This emphasizes that the dispersion of the charge-carrier plasmon can be a very complex parameter. Previously, the plasmon dispersion in quasi-one-dimensional metallic systems has been investigated theoretically and experimentally for a few compounds. Within RPA it has been predicted that the plasmon dispersion in one-dimensional metals can be substantially modified by local field effects, i. e., the inhomogeneous character of the electron gas. The influence of local field effects can even cause a negative plasmon dispersion based on a tight-binding description of the electronic bands [252].

At the end of this section we want to present the results of DFT based calculations on potassium intercalated picene for different values of the momentum transfer [151]. In Fig. 5.9 we show the evolution of the loss spectra upon increasing  $q$  for the three main crystallographic directions as received from the calculations. In all spectra a broadening of the plasmon peak with increasing  $q$  can be observed, whereas only for  $q$  along the  $a^*$ - and  $b^*$ -direction a small negative dispersion can be identified. In order to better understand the nature of the low-energy plasmon and to get further insight into the peculiar plasmon dispersion, the spectra were evaluated separating three different contributions (cf. Fig. 5.9 (d)): (i) only electronic transitions involving the three metallic  $\pi^*$  bands are taken into account (blue lines), (ii) taking into account also interband transitions (red lines), and (iii) including local field effects (black lines). Comparing the results calculated with and without interband contributions one can find, that for  $q$  in the  $a^*b^*$ -plane, the prominent peak is related only to transitions among occupied  $\pi^*$  bands, so that the plasmon peak in the loss spectra is due to collective oscillations of the conduction electrons. On the contrary, for  $q$  along the  $c^*$  axis, interband transitions give a remarkable contribution as well.

The free-electron contribution due to intraband transitions of the six conduction electrons would give rise to a "bare plasmon", which have been simulated by considering only transitions between metallic bands. The bare plasmon frequency has a strong negative dispersion along each direction, which is in contrast to the positive dispersion of a plasmon in the homogeneous electron gas. Such a behavior has been discussed also in literature on the basis of a tight-binding model [253]. This effect is contrasted by interband transitions through screening effects. Including the contribution of interband transitions at frequencies higher than  $\omega_p$  reduces the negative dispersion of the bare plasmon (can be seen by comparing the blue and red lines in Fig. 5.9 (d)). Finally, local field effects are



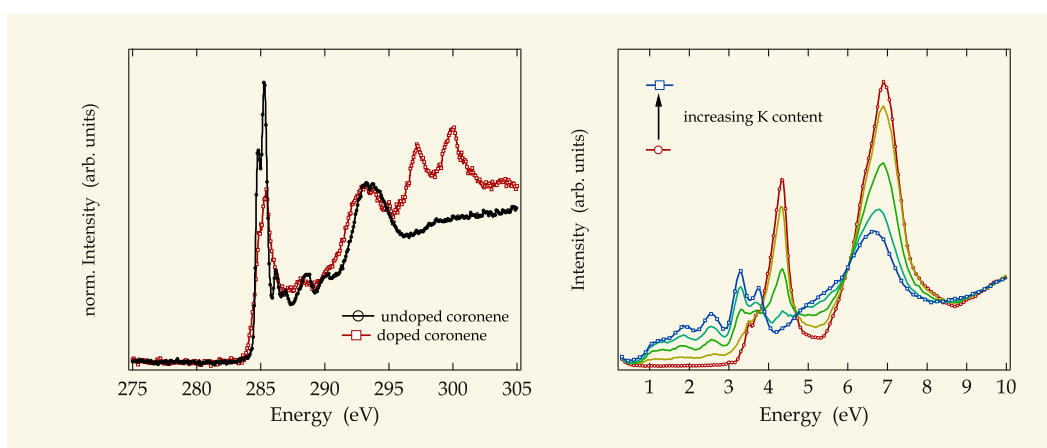
**Figure 5.9.** | Calculated loss function of K<sub>3</sub>picene for a momentum transfer  $q$  along the  $a^*$ ,  $b^*$ , and  $c^*$  axes, respectively [151].

responsible for mixing among intraband and higher energy interband  $\pi \rightarrow \pi^*$  transitions. LFE become more important as the momentum transfer increases, since in real space this implies probing induced charge densities on a shorter scale, where charge inhomogeneities become more relevant. Therefore, LFE further reduce the negative plasmon dispersion, inferred by comparing the blue and black lines in Fig. 5.9 (d). On a quantitative level, the effect of interband transitions and crystal local fields on the plasmon dispersion depend on the polarization properties of the molecules. For  $q$  along  $c^*$ , the molecules are highly polarizable, so that the corrections to the bare plasmon are large and the negative dispersion is completely suppressed. On the contrary, for  $q$  along the  $a^*$ -axis, the effect is weaker (the molecules are less polarizable) and the negative dispersion of the bare plasmon is only reduced, but still visible, as we can see also in the experimental spectra in Fig. 5.8.



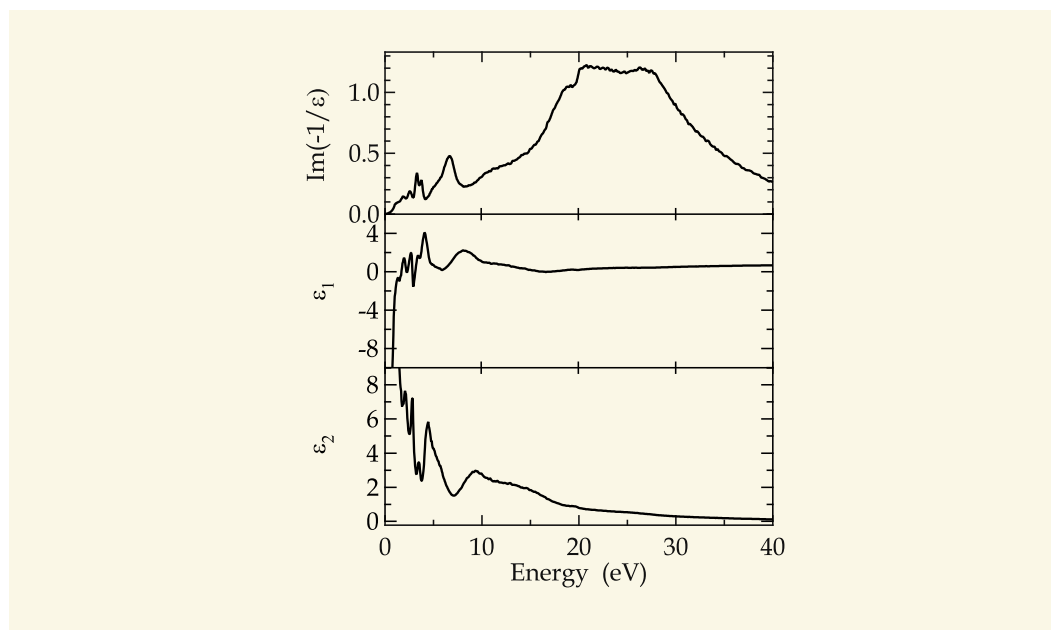
### 5.3. Electronic Structure Of Potassium Doped Coronene

In this section we discuss the effect of potassium doping on the electronic structure of coronene. In the left panel of Fig. 5.10 we show a comparison of the C 1s and K 2p core-level excitations of undoped and potassium-doped coronene. The observed influences due to potassium doping are very similar to what was observed for K intercalated picene discussed in Sec. 5.2. Both spectra are dominated by a well pronounced feature in the range between 284 and 286 eV, whereby the spectral weight is reduced upon doping. Additionally, in case of potassium-doped coronene also the K 2p core excitations are observable at 297.2 and 300 eV. In particular, the spectral shape of the K 2p core excitations is clearly different from the much broader and less structured K 2p core excitation spectrum of a pure potassium multilayer [254]. Both facts, the reduction of the C 1s excitation feature as well as the observation of the K 2p core excitations, signal a successful doping of the sample. Furthermore, we observe a clear broadening of the first C 1s feature which might arise from a change of the binding energy of the C 1s core levels because of the introduced potassium atoms as well as lifetime effects in the metallic doped coronene. Moreover, upon charging the coronene molecules will most likely undergo a Jahn-Teller distortion [255], which leads to a splitting of the electronic molecular levels and thus to a spectral broadening in our data. Also, band structure calculations of  $K_3$ coronene (cf. Ref. 139) predict shifts of the conduction bands as compared to pristine coronene which would result in a broadening as seen in Fig. 5.10. Additionally, also a mixing of different phases, which we cannot exclude, can result in a broadening of the C 1s signal. The results shown in the left panel of Fig. 5.10 indicate a doping level of  $K_{2.8}$ coronene.



**Figure 5.10.** | Left panel: C 1s and K 2p core-level excitations of undoped (black circles) and potassium-doped (red open squares) coronene. Right panel: Evolution of the loss function of coronene in the range of 0 - 10 eV upon potassium doping. All spectra were normalized in the high-energy region between 9 and 10 eV.

Moreover, intercalation of coronene thin films with potassium also influences the electronic structure as one can see in Fig. 5.10 (right panel), where we present a comparison of

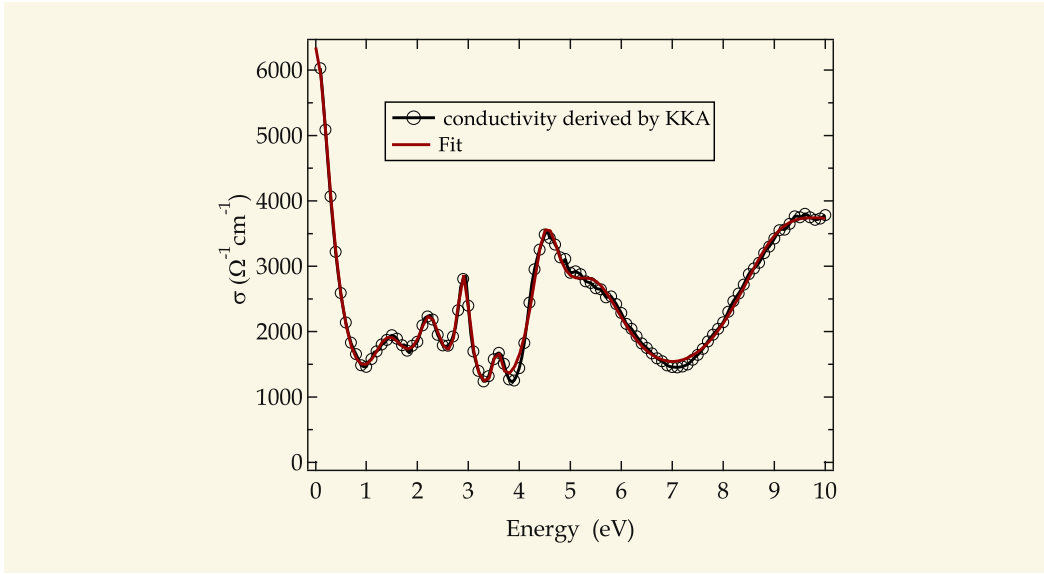


**Figure 5.11.** | Loss function ( $\text{Im}(-1/\epsilon)$ ), real part ( $\epsilon_1$ ) and imaginary part ( $\epsilon_2$ ) of the dielectric function of K doped coronene. The momentum transfer is  $q = 0.1 \text{ \AA}^{-1}$ .

the loss functions for different doping steps measured with a momentum transfer of  $q = 0.1 \text{ \AA}^{-1}$ . Again for undoped coronene we can clearly identify two main maxima at about 4.3 eV and 6.9 eV, and some additional features right after the excitation onset as discussed in Ch. 4. Upon doping, the spectral features become broader, and a downshift of the second, major excitation can be observed. We assign this downshift to a relaxation of the molecular structure of coronene as a consequence of the filling of antibonding  $\pi^*$  levels. Furthermore, a decrease of intensity of the feature at 4.3 eV upon potassium intercalation is visible. In addition, for the doped films new structures at 1.15, 1.9, 2.55, 3.3, and 3.75 eV are observed in the former gap of coronene. Taking into account the structural relaxation upon doping and the fact that the doped molecules are susceptible to a Jahn-Teller distortion [255], one would expect additional excitations in this energy region similar to what has been observed previously for other doped  $\pi$ -conjugated material [256, 257]. These then arise from excitations between the split former HOMO and LUMO of coronene and excitations from the former LUMO to LUMO+1, which become possible as soon as the LUMO is occupied. A direct assignment of the observed features however requires further investigations.

In order to obtain deeper insight into potassium-introduced variations, we have analyzed the measured loss function of doped coronene using a KKA. This analysis has been carried out for a metallic ground state since the observation of superconductivity as well as band structure calculations signal such a ground state for the stoichiometry of  $\text{K}_3\text{coronene}$ . Furthermore, the evolution of the loss function in Fig. 5.10 (right panel) indicates a filling of the former energy gap. In Fig. 5.11 we present the results of this analysis in an energy

### 5.3. Electronic Structure Of Potassium Doped Coronene



**Figure 5.12.** | Optical conductivity  $\sigma = \omega\epsilon_0\epsilon_2$  of K doped coronene for a momentum transfer of  $q = 0.1 \text{ \AA}^{-1}$  (black circles) derived by a KKA of the loss function. Additionally, the result of a Drude-Lorentz fit is shown (red line).

range between 0 and 40 eV. The loss function (see Fig. 5.11 upper panel) is dominated by a broad maximum in the range between 20 and 27 eV which can be assigned to the  $\pi + \sigma$  plasmon. Various interband excitations at 2–20 eV can be observed as maxima in the imaginary part of the dielectric function,  $\epsilon_2$  (lower panel). Most interestingly,  $\epsilon_2$  shows in the energy range between 0 and 6 eV only four maxima in contrast to the five features in the loss function. The zero crossing near 1.8 eV in the real part of the dielectric function (middle panel), as well as the absence of a peak at the same energy in the imaginary part of the dielectric function and accordingly the optical conductivity  $\sigma$  (see Fig. 5.12), leads to the conclusion that the second spectral feature at 1.9 eV represents a collective excitation, and we assign it to the charge carrier plasmon of doped coronene. For the test of the consistency of our KKA we checked again the sum rules which resulted in a very good agreement of the two values for the loss function and for the dielectric function and further agree with the value that is expected from a calculation of the electron density of doped coronene. Moreover, a further sum rule which is only valid for metallic systems and independent of the plasma frequency (cf. Eq. 2.29) can be employed. In case of doped coronene we arrive at a value of 1.562, which is even very close to the expectation of  $\pi/2$ .

In order to obtain access to further information we show in Fig. 5.12 the optical conductivity of potassium-doped coronene, whereas we can derive the dc conductivity of  $\text{K}_{2.8}$  coronene of about  $6300 \text{ \Omega}^{-1}\text{cm}^{-1}$  from the value of  $\sigma$  at  $\omega = 0$ . Additionally, we fitted the optical conductivity using a simple Drude-Lorentz model and the resulting fit parameters are given in Tab. 5.2 and are also shown in Fig. 5.12 as a red line. We note that the result of our fit also describes  $\epsilon_1$  very well, which demonstrates the consistency of our description. We arrive at an unscreened plasma frequency  $\omega_D$  of about 4.35 eV.

**Table 5.2.** | Parameters derived from a Drude-Lorentz fit of the optical conductivity of K doped coronene (as shown in Fig. 5.12) using formula 5.1. The Drude part is given by the plasma energy  $\omega_D$  and the width of the plasma (damping)  $\gamma_D$ , while  $f_j$ ,  $\gamma_j$  and  $\omega_{j_0}$  are the oscillator strength, the width and the energy position of the Lorentz oscillators.

i	$\omega_{j_0}$ (eV)	$\gamma_j$ (eV)	$f_j$ (eV)	$\gamma_D$ (eV)	$\omega_D$ (eV)
1	1.47	1.01	3.12	0.40	4.35
2	2.25	0.65	2.55		
3	2.90	0.34	2.22		
4	3.57	0.22	1.06		
5	4.52	0.77	3.67		
6	5.48	1.83	5.26		
7	9.15	2.75	7.00		
8	10.64	2.84	6.76		

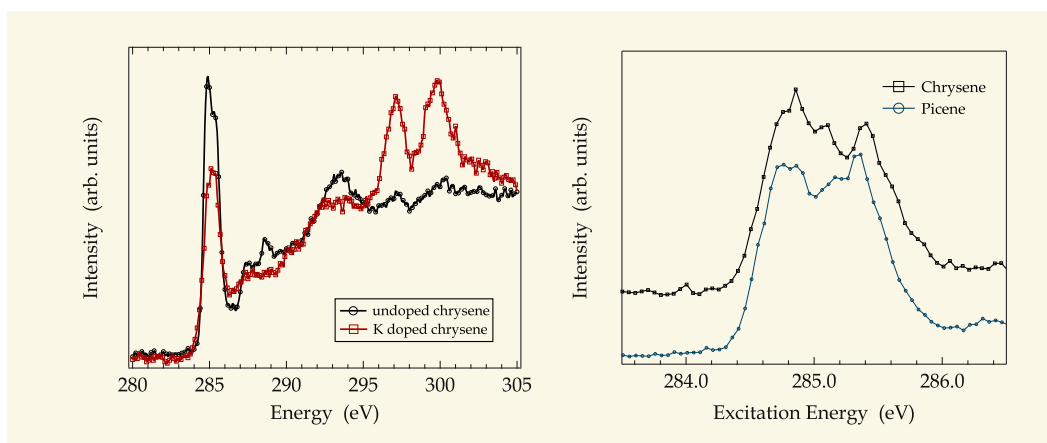
Furthermore, we can compare this value with the plasma frequency which we expect if we take the additional six conduction electrons per unit cell (2 coronene molecules per unit cell) in  $K_3$ coronene into account. We arrive at a value of 3.42 eV which is somewhat lower than what we derived using our fit procedure. This might again be related to an effective mass of the charge carriers in doped coronene. Finally, a comparison of the unscreened and screened plasma frequencies can be used to derive the averaged screening  $\epsilon_\infty$  of the charge carrier plasmon. This gives a value of  $\epsilon_\infty \sim (4.35/1.8)^2 \sim 5.8$ . We note however that this is a very rough approximation for  $K_3$ coronene, since there are close lying interband excitations in the corresponding energy region.

#### 5.4. Further Candidates For Hydrocarbon Superconductors

After the discovery of superconductivity with rather high transition temperatures in different, potassium doped aromatic hydrocarbons the search for further candidates of this “new class” of superconductors is the normal way of the research routine. Chrysene displays a close relative of the two superconductors phenanthrene and picene and is also made of benzene rings which are arranged in a zigzag manner. A comparison with the electronic structure of undoped as well as potassium doped chrysene with the spectra of picene might promote some interesting results which support the prediction of superconductivity in chrysene.

The comparison of the C 1s core level excitation of pristine chrysene with pristine picene show, as depicted in Fig. 5.13, that the principle shape of the dominant and strong excitation in the range between 284 and 286 eV are very similar. The C 1s core-level excitation in chrysene is characterized by a fine structure with four maxima around 284.7, 284.8, 285.1, and 285.4 eV, very similar to picene and coronene (cf. Sec. 4.2 and Sec. 4.3). In

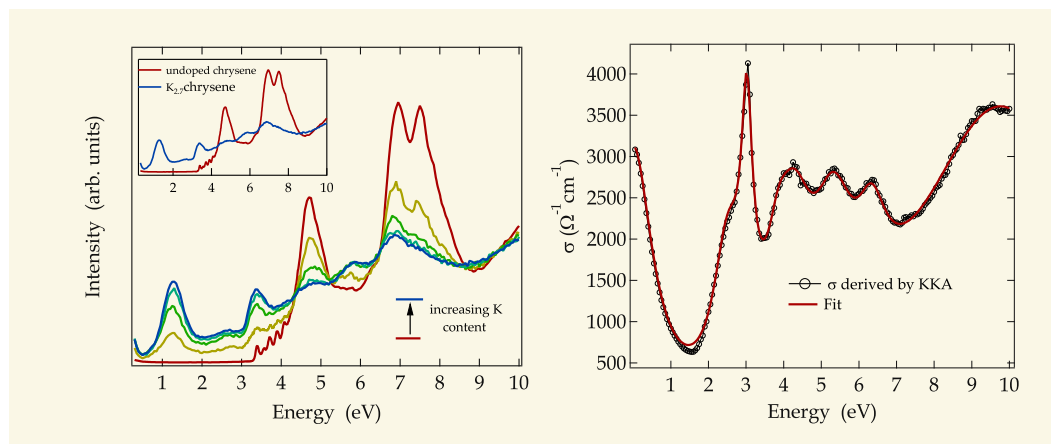
## 5.4. Further Candidates For Hydrocarbon Superconductors



**Figure 5.13.** | Left panel: C 1s and K 2p core level excitations of undoped and potassium doped chrysene. Right panel: C 1s excitation data of solid chrysene and picene.

case of picene and coronene, as mentioned in the previous discussion, this fine structure is in very good agreement with first-principle band structure calculations which find four close-lying conduction bands in this region. Furthermore, similar theoretical calculations have been performed for phenanthrene and resulted in four conduction bands near the Fermi level, which are very close in energy and show a strong molecular character with weak overlap related to the LUMO and LUMO+1 [159]. Unfortunately, similar theoretical investigations are absent for chrysene, but because of the analogy in crystal structure compared to phenanthrene and picene it is reasonable to assume a very similar band structure for chrysene and we assign the structures observed for chrysene in Fig. 5.13 (right panel) also to four unoccupied levels that are very close in energy. Furthermore, in Fig. 5.13 (left panel) we present the comparison of the C 1s and K 2p core excitation edges for pure and K intercalated chrysene with highest archived doping level. A similar interpretation of the spectra as in the previous sections results in an intensity reduction of the first C 1s excitation feature of about 30%, i. e., the doping has resulted in about 2.4 electrons per chrysene molecule. Additionally, the stoichiometry analysis based on a comparison of the K 2p and C 1s core excitation intensities of doped chrysene with that one of  $K_6C_{60}$  signals a doping level of  $K_{2.7}$ chrysene. This value is slightly larger than our estimate via the C 1s intensity variation above. Since the previous approach is quite sensitive to the background due to higher lying excitations, we consider the doping level of  $K_{2.7}$ chrysene as representative.

In common with doped picene also the electronic excitation spectrum of chrysene changes substantially upon potassium doping. In the left panel of Fig. 5.14 we present the evolution of the loss function up to 10 eV excitation energy as a function of potassium addition. These data are taken with a small momentum transfer  $q$  of  $0.1 \text{ \AA}^{-1}$ . In the former gap of chrysene new spectral features gradually show up at about 1.3, 2.8, and 3.4 eV with increasing doping level, while the other structures broaden and lose intensity. Also, a downshift of the major excitations can be observed. We assign this downshift



**Figure 5.14.** | Left panel: Evolution of the loss function of chrysene in the range of 0-10 eV upon potassium doping measured with a momentum transfer of  $q = 0.1 \text{ \AA}^{-1}$ . All spectra were normalized in the high-energy region between 9 and 10 eV. The inset shows a comparison of the spectra of undoped and highest doped chrysene ( $K_{2.7}$ chrysene). Right panel: Optical conductivity of K-doped chrysene derived by a KKA of the measured loss function. Additionally, the result of a Drude-Lorentz fit is shown as red line.

to a relaxation of the molecular structure of chrysene and the concomitant shift of the electronic molecular orbitals as a consequence of the filling of antibonding  $\pi^*$  levels. The spectrum for  $K_{2.7}$ chrysene represents saturation doping under the conditions applied in our experiment, and in the inset of Fig. 5.14 (left panel) we depict a comparison of the spectra for undoped and highest doped chrysene. Moreover, the data in Fig. 5.14 suggest a smooth transition from undoped chrysene to a doped phase without indication of intermediate phases which could have different electronic excitation spectra. This is in contrast to the observations of 1,2;8,9-dibenzopentacene describe in Sec. 5.1 or other doped molecular crystals, where the electronic excitations clearly change in a multi-step manner according to the formation of various doped phases with particular potassium content [258–260]. Consequently, in the following we will concentrate on the potassium doped chrysene sample with highest doping level and analyze its properties in further detail.

To obtain deeper insight into the doping induced variations, we have analyzed the measured loss function of  $K_{2.7}$ chrysene using again a KKA. The results of the KKA provide us the possibility to get additional information about the nature of the observed spectral features. In analogy to the results in the previous chapter, the new low energy excitation at about 1.3 eV in the loss function is not represented by a maximum in  $\epsilon_2$ , but by a zero crossing in the real part of the dielectric function. Therefore, this spectral feature represents a collective charge carrier excitation, and we assign it to the charge carrier plasmon of doped chrysene. To elucidate all the observations further, we show in Fig. 5.14 (right panel) the optical conductivity  $\sigma$  of doped chrysene. Even in case of doped chrysene the optical conductivity consists of a free electron contribution at low energies due to

## 5.4. Further Candidates For Hydrocarbon Superconductors

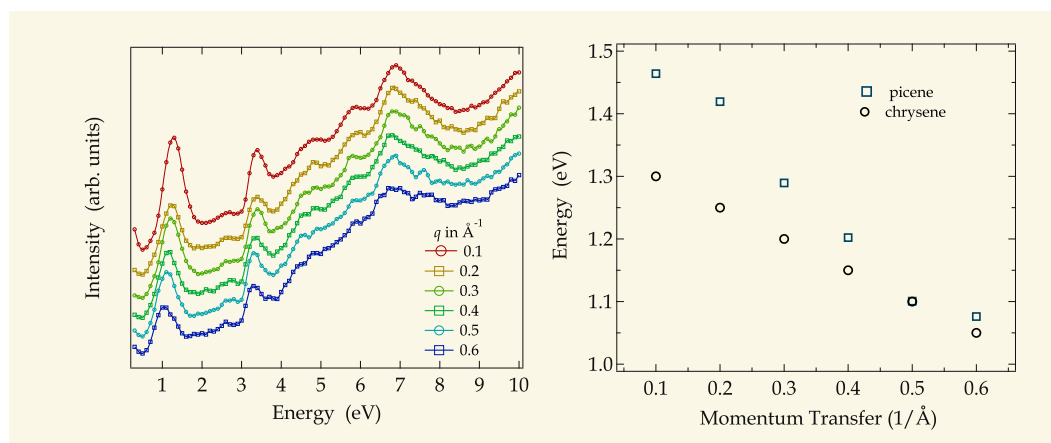
**Table 5.3.** | Parameters derived from a Drude-Lorentz fit of the optical conductivity. The Drude part is given by the plasma energy  $\omega_D$  and the width of the plasma (damping)  $\gamma_D$ , while  $f_j$ ,  $\gamma_j$  and  $\omega_{j_0}$  are the oscillator strength, the width and the energy position of the Lorentz oscillators.

i	$\omega_{j_0}$ (eV)	$\gamma_j$ (eV)	$f_j$ (eV)	$\gamma_D$ (eV)	$\omega_D$ (eV)
1	2.53	0.99	3.52	0.62	3.79
2	3.02	0.35	2.55		
3	3.86	0.74	2.08		
4	4.30	1.18	3.63		
5	5.34	1.30	3.76		
6	6.34	0.93	2.49		
7	9.82	5.69	12.11		

intraband transitions in the conduction bands and some additional interband contributions. Following the evaluation procedure used in case of picene and coronene and further to get the right energy positions of the single oscillators as well as the width and the strength we fitted the optical conductivity using a Drude-Lorentz model. The resulting fit parameters are given in Table 5.3 and are also shown in Fig. 5.14 (right panel) as a red line. We arrive at an unscreened plasma frequency  $\omega_D$  of about 3.79 eV. A comparison of the unscreened and screened (measured) plasma frequencies can be used to derive the averaged screening background dielectric constant and results  $\epsilon_\infty \sim (3.79/1.3)^2 \sim 8.5$ .

This value is significantly larger than the static dielectric constant of undoped chrysene, where we derived a value of 3-3.1, and which is in very good agreement with reported values [261, 262]. In other words, the screening ability of doped chrysene seems to be larger than that of the parent compound. A similar behavior was observed in potassium doped picene and coronene.

At the end of the discussion we show in Fig. 5.15 (left panel) the evolution of the loss function of K doped chrysene with increasing  $q$  in an energy range between 0 and 10 eV. With increasing momentum transfer the spectra somewhat broaden in the entire energy range. While all visible features above 1.5 eV do not show a change in their energy position, we observe a significant downshift for the charge carrier plasmon. In the right panel of Fig. 5.15, we present the evolution of the plasmon dispersion in the range 0.1-0.6  $\text{\AA}^{-1}$ . This dispersion is negative with a bandwidth of at least 250 meV. Our observation is in close analogy with the observed negative plasmon dispersion of the charge carrier plasmon in doped picene (cf. Fig. 5.15 blue squares). However, the bandwidth of the plasmon dispersion in picene in this momentum transfer range is  $\approx 150$  meV larger. Such a negative plasmon dispersion is in contrast to the traditional picture of metals based on the homogeneous electron gas, but the situation in molecular crystals can be considerably different, as e. g., reported for alkali-doped  $C_{60}$  compounds [246]. Furthermore, the calculations presented in Sec. 5.2 show, that this finding is the result



**Figure 5.15.** | Left panel: Momentum dependence of the EELS spectra of doped  $\text{K}_{2.7}$ chrysene. Right panel: Plasmon dispersion for K doped chrysene in comparison to K doped picene up to a momentum transfer  $q$  of  $0.6 \text{\AA}^{-1}$ ,

of the competition between metallicity and electronic localization on the molecular units. Since the electrons are mainly confined to the individual molecules, conduction electrons alone give rise to the negative dispersion, which is reduced by molecular polarization and crystal local-field effects.

In conclusion, due to the analogy between the observed changes in the electronic structure upon potassium doping between chrysene and picene and further the similarity in the crystal structure, as mentioned at the beginning of this section, one can speculate that chrysene is a promising candidate for another aromatic hydrocarbon superconductor with a transition temperature between that of phenanthrene and that of picene. This issue certainly needs further investigations from both, experiment and theory to be settled.





*"Have a plan and stick to it."*

Heinrich Harrer\*

# 6

## Summary And Outlook

**T**HE main aim of this work was to give insight into the electronic properties of several selected aromatic hydrocarbon system in the condensed phase, in particular for 3 systems, which recently were found to be superconducting, if intercalated with alkali metals. Therefore, the electronic structure, both in the undoped as well as in the potassium doped state, of picene, coronene, and 1,2;8,9-dibenzopentacene have been extensively investigated using electron energy-loss spectroscopy as the main experimental method. Additionally, also photoemission spectroscopy experiments have been performed to investigate the occupied electronic density of states close to the chemical potential. In order to learn more about the electronic structure we compared the results we obtained from EELS and photoemission spectroscopy with theoretical calculations based on DFT using LDA.

In detail, in case of picene our data reveals a high density of unoccupied states close to the Fermi energy. The loss function measured at small momentum transfer values is in a very good agreement with theoretical calculations and we assigned the observed excitations to different interband transitions as well as to plasmons. Furthermore, our EELS studies at low temperatures and as a function of momentum transfer enabled us to elucidate the low-energy singlet excitations in solid picene. The electronic excitation spectrum consists of five excitons below the transport energy gap. While only one of these excitons is seen in the condensed phase, and we attribute it to a charge-transfer excitation involving neighboring molecules in the crystal. Moreover, this solid-state specific exciton is also distinguished by a significant dipole forbidden character, as revealed by our momentum-dependent investigations.

The electronic excitation spectrum changes substantially upon doping. In particular, a new low energy feature is observed at about 1.5 eV in the former optical gap, which is assigned to the charge carrier plasmon of doped picene (whereas electron diffraction

---

\*Heinrich Harrer (1912 – 2006). Austrian mountaineer, geographer, and author best known for being on the four-man climbing team that made the first ascent of the North Face of the Eiger. Quote from a letter Harrer wrote to Reinhold Messner after he reached the summit of his last eight-thousander, Lhotse, and thus became the first person to climb all eight-thousanders.

and core level excitation data signal the formation of a doped phase with a stoichiometry close to  $K_3$ picene, which is reported to become superconductive). Interestingly, this charge carrier plasmon disperses negatively upon increasing momentum transfer, which deviates significantly from the traditional picture of metals based on the homogeneous electron gas. The comparison with calculations of the loss function of potassium intercalated picene shows how this finding is the result of the competition between metallicity and electronic localization on the molecular units.

For a further understanding how potassium influences such hydrocarbon systems, we studied additionally the electronic properties of coronene and chrysene, whereby the latter displays a close relative to phenanthrene and picene. For both systems the doping introduced changes are in a comparable range such as observed for picene. The pristine materials show a fine structure in the C 1s signal, which can be seen as an evidence for four energetically close lying conduction bands near the Fermi level. This observation seems to be uniform in all hydrocarbons built up—in one or another way—in such a zigzag manner. In case of chrysene a doping level of  $x = 2.7$  could be archived, whereas in case of coronene the stoichiometry analysis indicates a doping level of about  $x = 2.8$ . The changes in the excitation spectra can be summarized with the appearance of one prominent low energy excitation at 1.3 eV, in case of chrysene, and several new features, which show up upon potassium intercalation, in case of coronene. Interestingly, carrying out a Kramer-Kronig analysis of the measured loss spectra lead to a significant increase of the background dielectric screening for the doped systems as compared to the parent compound. This might be related to the appearance of superconductivity in doped picene and coronene, and one can argue that chrysene is a promising candidate for another aromatic hydrocarbon superconductor.

In this context, we further investigated the influence of potassium doping on thin films of 1,2;8,9-dibenzopentacene—the hydrocarbon superconductor with the highest  $T_c$ . The doping induced changes in the valence band as well as in core level excitations, and the temperature dependence of the measured spectra clearly indicate the formation of phases with  $K_1$ dibenzopentacene,  $K_2$ dibenzopentacene, and  $K_3$ dibenzopentacene composition. These different phases are characterized by the appearance of several new peaks in the excitation spectra. Our data suggest that  $K_1$ dibenzopentacene has an insulating ground state with an energy gap of about 0.9 eV, while  $K_2$ dibenzopentacene and  $K_3$ dibenzopentacene might well be metallic, because of the absence of an energy gap in the electronic excitation spectra. Interestingly, a comparison of the photoemission as well as EELS spectra of undoped 1,2;8,9-dibenzopentacene with pentacene reveals that the electronic states close to the Fermi level and the electronic excitation spectra of the two materials are extremely similar, which is due to the fact, that the additional two benzene rings in 1,2;8,9-dibenzopentacene virtually do not contribute to the delocalized  $\pi$  molecular orbitals close to the Fermi level. The wave functions of the HOMO and LUMO of 1,2;8,9-dibenzopentacene are essentially restricted to the inner—pentacene-like—part of the molecule and maintain their character compared to pentacene. This results in almost-identical ionization potentials and electron affinities for the two materials. This close

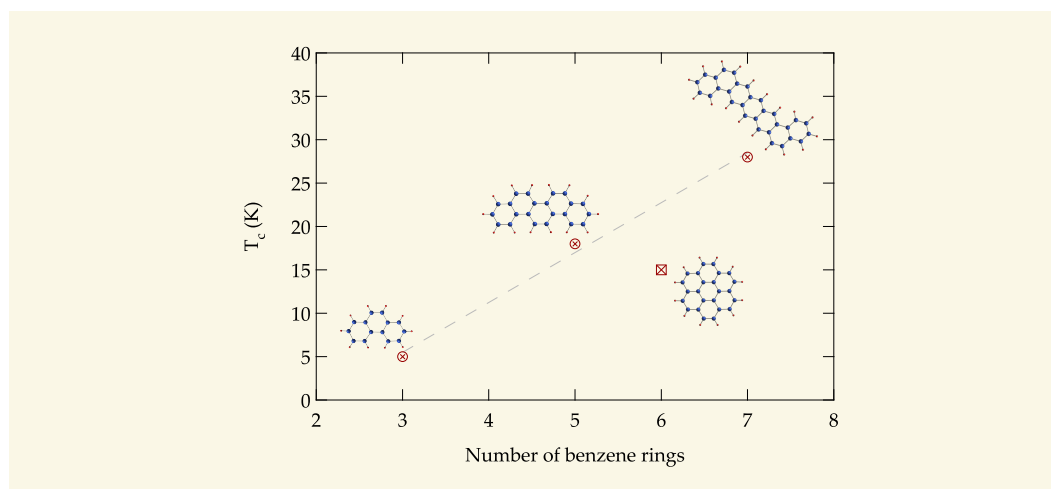
---

electronic similarity is in contrast to the behavior upon potassium doping, where evidence for a Mott state has been reported in the case of pentacene, while 1,2;8,9-dibenzopentacene has been found to become superconducting.

Finally, we compared the low energy excitation spectra of chrysene with picene as well as tetracene with pentacene crystals to gain information about, what makes this zigzag structure compared to the linear arrangement of benzene rings so special. Our data reveal a significant difference between the former and the latter two materials. While for the phenacenes (zigzag arrangement) the excitation onset is characterized by up to five weak excitation features with only small anisotropy and without visible Davydov splitting within the  $a^*, b^*$ -planes, the acene (linear arrangement) spectra are dominated by a large excitation close to the onset and a sizable Davydov splitting. We further show that the spectral shape of the pentacene excitation spectrum provides clear evidence for a large admixture of molecular Frenkel-type excitons with charge-transfer excitations resulting in excited states with a significantly mixed character. This conclusion is in good agreement with recent advanced calculations which predicted a charge-transfer admixture to the lowest singlet excitation which is significantly dependent upon the length of the acene molecules. Moreover, also for picene and chrysene we observe differences which point towards an increased charge-transfer contribution to the singlet excitation spectrum in the former.

As an outlook, we show in Fig. 6.1 the dependence of the superconducting transition temperature on the number of benzene rings for the four hydrocarbon systems, which become superconductors upon alkali doping. It can be seen, that with increasing length of chain,  $T_c$  increases from 5 K for  $K_3$ phenanthrene with three benzene rings to 18 K for  $K_3$ picene with five benzene rings, and up to 33 K for  $K_3$ dibenzopentacene with seven benzene rings. Additionally, also coronene, which is structurally different from the three other hydrocarbon superconductors, with a  $T_c$  of 15 K is shown in the Fig. 6.1. This behavior is in contrast to the theoretical prediction that, assuming a conventional BCS mechanism with electron-phonon interaction, and the same density of states at the Fermi level, forecasts that the doped phenanthrene should have the highest  $T_c$  in all aromatic hydrocarbons. In all molecular crystals it is however known, that the crystal structure, molecular overlaps, and phonon modes are important factors for determining the strength of pairing interaction. Usually, increasing the length of the chain would increase the extent of its interactions with neighboring chains, while the density of states at the Fermi level is mainly dominated by intermolecular interactions. Up to now it is still not clear whether the perfect *W*-shaped configurations of benzene rings (such in picene) are the key role to achieve superconductivity in doped polycyclic aromatic hydrocarbons, even if a kink in the structure seems to be a precondition for the occurrence of superconductivity. Furthermore,  $T_c$  seems to increase with the length of the molecule.

Further detailed studies are needed, both experimental and theoretical, to shine more light on the mechanism of superconductivity in these new hydrocarbon superconductors, which constitute a new class of carbon-based superconductors, and the link to structurally



**Figure 6.1.** | Comparison of  $T_c$  of the “new” hydrocarbon superconductors as a function of the number of benzene rings building the molecule.

properties. A direct extension of this work could be to study on the one hand the doping dependence of the EELS spectra of the investigated hydrocarbons with other alkali metals, e. g., sodium, rubidium, or even calcium, whereas the latter one provides one additional electron compared to potassium. On the other hand the investigation of the electronic structure of other hydrocarbons, which are structurally related to picene or 1,2;8,9-dibenzopentacene, e. g., fulminene (six benzene rings which are arranged in a zigzag manner) can be very instructive. Moreover, characterisation of hydrocarbons, which consist of both cyclopentane (five membered ring) as well as benzene rings, such as corannulene and truxene, can help to understand the influence of localization on the electronic structure and might be a guide to further promising candidates of high  $T_c$  organic superconductors.

The discovery of this “new class” of organic superconductors is an exciting new development in the search for carbon-based superconductors. The strong electron–phonon coupling of the hydrocarbon molecule may produce high  $T_c$ 's, comparable to those of  $C_{60}$  superconductors. Due to the multiband character of the conduction and valence bands, interesting electron correlation effects including electron mechanisms of superconductivity may also be expected. Therefore, studying carbon, with its many allotrops and compounds, is one of the most fascinating problems in science and, in particular, the discovery of superconductivity in metal-doped aromatic molecules opens a new and auspicious field of research.



*“The important thing is not to stop questioning.”*

Albert Einstein

*"The most beautiful experience we  
can have is the mysterious."*

Albert Einstein



## Relativistic Calculation Of The Incoming Wave Vector

To get a better understanding of the kinetics within the EELS experiments and to extend the discussion in Sect. 2.2, the main aim of this appendix is to calculate the absolute values of the wavevector of the incoming electrons in the EELS spectrometer.

The starting point is the relativistic conservation of energy, which is given by

$$m(v)c^2 = m_0c^2 + E_0 = \gamma m_0c^2,$$

where  $E_0 = 172$  keV stands for the energy of the incoming electrons due to the acceleration in the spectrometer,  $m_0$  is the invariant mass of the electrons,  $c$  the speed of light in vacuum, and  $\gamma$  is the Lorentz factor defined by

$$\gamma \equiv \frac{1}{\sqrt{1 - \frac{v^2}{c^2}}} = 1 + \frac{E_0}{m_0c^2}.$$

The previous formula provides a connection between the energy of the electrons and their velocity

$$v^2 = c^2 - \left( \frac{m_0c^2}{m_0c^2 + E_0} \right)^2.$$

On the other hand the 4-vector of the momentum reads

$$p^\mu = \left( \frac{E}{c}, \mathbf{p} \right) = \left( \frac{E}{c}, m\mathbf{v} \right) = \left( \frac{E}{c}, \gamma m_0\mathbf{v} \right) = \left( \frac{\hbar\omega}{c}, \hbar\mathbf{k}_0 \right).$$

So the spatial part of the momentum 4-vector is related to the wave vector  $\mathbf{k}_0$  which is then given by

$$\mathbf{k}_0 = \frac{m_0}{\hbar} \gamma \mathbf{v}.$$

Finally, this leads with the known electron energy to

$$k_0 = \frac{m_0 c}{\hbar} \cdot \left(1 + \frac{E_0}{m_0 c^2}\right) \cdot \sqrt{1 - \left(\frac{m_0 c^2}{m_0 c^2 + E_0}\right)^2}$$

Inserting all the known quantities

$$\begin{aligned} m_0 &= 512 \frac{\text{keV}}{c^2} \\ E_0 &= 172 \text{ keV} \\ c &= 3 \cdot 10^8 \frac{\text{m}}{\text{s}} \\ \hbar &= 1.054 \cdot 10^{-34} \text{ Js} \end{aligned}$$

justifies the relativistic approach, as

$$\frac{v}{c} \approx 0.66 \tag{A.1}$$

and yields an approximate value for the wave vector

$$k_0 \approx 230^{-1}. \tag{A.2}$$

*“By following well laid paths some forgotten flower may be gathered, but nothing essentially new will be found.”*

August Kekulé\*

# B

## Structure And Aromaticity

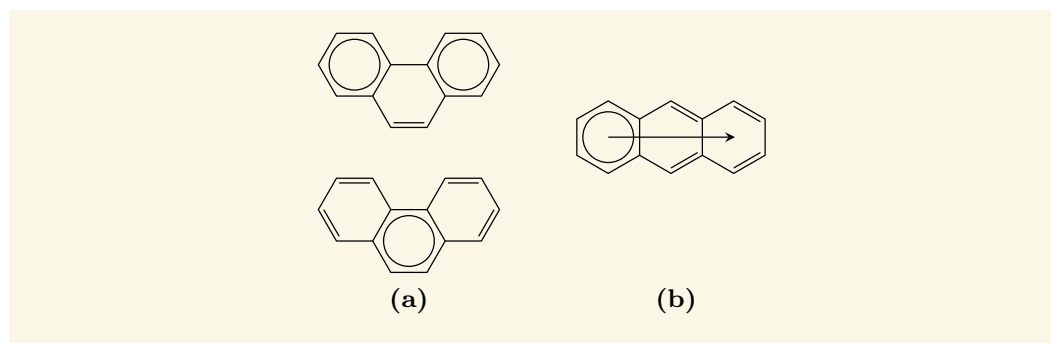
The aim of this appendix is to shine light into the topic of Clar structures and the rules behind and further to understand how aromaticity and the arrangement of benzene rings within the molecule influences physical properties. Aromaticity is one of the most discussed properties in organic chemistry, whose definition and conceptualization remain controversial. The earliest use of the word “aromatic” was in an article by August Wilhelm Hofmann in 1855 [263]. The next major advance was the description of the structure of benzene by August Kekulé in 1865 who further suggested that the number of isomers in substituted benzenes could be accounted for by “oscillation” between two different arrangements of bonds [264]. Over the next few decades, most chemists readily accepted this structure, since it accounted for most of the known isomeric relationships of aromatic chemistry. The cyclic nature of benzene was finally confirmed by the crystallographer Kathleen Lonsdale in 1929 [265, 266].

A important step towards the comprehension of aromatic concepts represents the so-called Hückel ( $4n + 2$ )-rule introduced by physical chemist Erich Hückel in 1931 [267–269]. Interestingly, although Hückel's rule is strictly applicable to single ring systems [270], many polycyclic aromatic hydrocarbon systems follow it likewise. But coronene, for example, displays a famous exception of the rule because it is still aromatic even though it doesn't fulfil the ( $4n+2$ )-rule.

It was Erich Clar who introduced a novel representation of benzenoids in which localized  $\pi$ -sextets are emphasized and within his model the “extra” stability of  $6n$   $\pi$ -systems can be explained [98, 99]. His work followed an earlier suggestion by Armit and Robinson in 1925 to collect  $\pi$ -electrons in benzenoids, when possible, into groups of six, which are located within single nonadjacent benzenoid rings [271]. A Clar structure can be constructed as a valence structure satisfying the following simple rules: (1) Draw as many as possible  $\pi$ -sextets in nonadjacent rings (there may be more than one realisation, which should then be indicated by arrows) and (2) Having as few as possible C=C double bonds (it is required that the carbon atoms not involved in the sextet rings should be coupled to

---

\*Friedrich August Kekulé (1829-1896). Quote from a lecture presented by Kekulé at a celebration of the 25th anniversary of Kekulé's benzene theory held in Berlin City Hall in 1890.



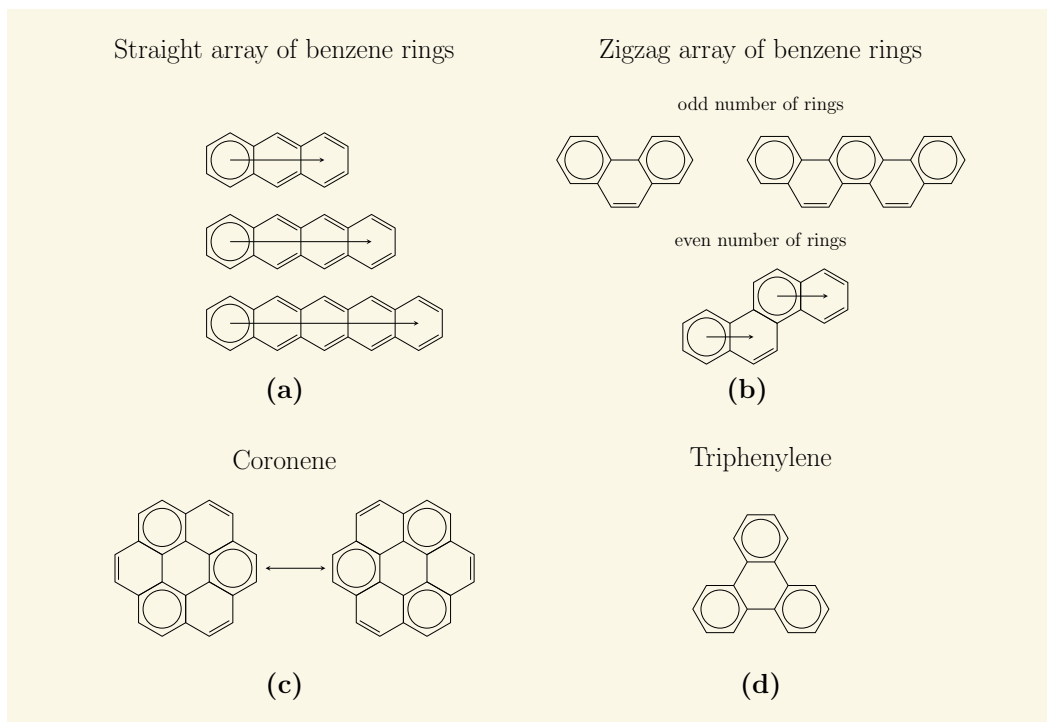
**Figure B.1.** | Comparison between the Clar structure of two isomers: phenanthrene and anthracene. (a) Application of Clar's sextet rule to phenanthrene indicating that the structure with two  $\pi$ -electron sextets in the outer rings is more favourable than the alternative structure with a single  $\pi$ -electron sextet in the central position. (b) Clar structure of anthracene, whereas the arrow indicate that more than one realisation is possible.

form C=C double bonds). In other words, after assigning  $\pi$ -sextets to as many rings as possible one continues to assign C=C double bonds so that all the  $\pi$ -electrons are either included in sextets or C=C double bonds to complete a valence structure. The localized  $\pi$ -sextet is represented formally by a circle inscribed in a benzene ring. For instance, in the case of phenanthrene, two structure may be drawn, one with aromatic sextets in both outer rings and one with a single aromatic sextet in the central ring (cf. B.1 (a)). The latter one did not follow the sextet rule and is therefore energetically not so favourable as the former one. Therefore in this molecule the outer rings are firmly aromatic while its central ring is less aromatic and therefore more reactive. In contrast, in anthracene (B.1 (b)) the number of sextets is just one and aromaticity spreads out. This difference in number of sextets is reflected in the UV absorption spectra of these two isomers. Phenanthrene has its highest wavelength absorbance around 290 nm, while anthracene has highest wavelength bands around 380 nm.

Many experimental confirmations suggest that Clar's model provides a reasonable and accurate representation of the physical reality [272–276]. Thus, it explains the decrease in stability and aromaticity of the acenes with increasing annelation (like mentioned in Sec. 3.2.2). The higher members of the series are increasingly reactive and behaving more like highly conjugated olefins than aromatic hydrocarbons. In conclusion, the considerably greater stability of the phenacenes compared to the acenes can be understood on the basis of the increasing number of aromatic sextets due to an increase of number of benzene rings, whereas the number of sextets doesn't change by increasing the length of the molecule for linearly fused benzene rings (see Fig. B.2). Furthermore, several theoretical studies have offered a justification of Clar's theory [277–279].

However, when the  $\pi$  sextets exhaust all the chemical bonds (which means the system have only two types of rings: rings with  $\pi$ -sextets and "empty" rings), then the structure is called "fully benzenoid", which defines the most aromatic case. For instance, triphenylene





**Figure B.2.** | Clar structures of different hydrocarbons differs in the arrangement of the benzene rings, which display the building block.

( $C_{18}H_{12}$ , consisting of four fused benzene rings as depicted in Fig. B.2 (d)) can be seen as such a fully benzenoid PAH, meaning its structure is composed only of full benzene rings interconnected by C—C single bonds. As a consequence, triphenylene is much more resonance stable than its isomers like chrysene or tetracene, which makes it much more difficult to hydrogenate them to the saturated hydrocarbon.

In this sense, phenanthrene as well as picene are not fully benzenoid, because besides the sextets there exist rings with a single C=C double bond (cf. Fig. B.2). This is different to acenes for which there are as many Clar realisations as number rings exists. Thus, one can summarise that for hydrocarbons fused in a zigzag manner: (I) odd number of rings (phenanthrene, picene etc.) are non-fully benzenoid (with each molecule having a unique Clar structure), while (II) even numbers of benzene rings (chrysene etc.) are also non-fully benzenoid (but with each having multiple Clar structures). Straight arranged benzene rings (tetracene, pentacene etc.) are non-fully benzenoid (each having many Clar structure) (see Fig. B.2). Interestingly, maybe this is another hint for assuming that the kink in the structure and associated with that, the tendency of the wave function to be localized on the sextets are of strong importance. Hence, the relation of these quantum chemical properties with band structures and how these properties affect the electronic structure when these molecules are crystallised is a interesting future problem.

For further reading one may find more informations in Ref. 280 and Ref. 281.



*“What we observe is not nature itself,  
but nature exposed to our method of  
questioning.”*

Werner Heisenberg\*



## **Additional Information About Experimental And Theoretical Methods**

Because of the fact, that photoemission spectroscopy (PES) displays not the main experimental method used in this thesis a detailed introduction in this technique is not presented at the beginning of this dissertation. In consequence, this spectroscopic method is essential to get a deeper insight into the first occupied electronic levels—the so-called density of states (DOS)—near the Fermi energy, and thus PES represents a helpful tool for the development of a thorough understanding of the normal state properties, it is nevertheless useful to offer some informations and experimental parameters we use in our experiments. Therefore, the main aim of this appendix is to support the reader of this thesis with some additional informations about the PES measurements as well as the theoretical calculation presented in Sec. 4.2.

### **C.1. Photoemission**

For our PES studies, picene films with a thickness of about 6 nm were prepared by *in situ* thermal evaporation. A quartz microbalance was used to monitor the thickness of the films, which were grown with typical deposition rates in the order of 0.1 nm/min on a clean, polycrystalline gold substrate under ultra-high vacuum conditions. X-ray photoemission spectroscopy (XPS) and ultraviolet photoemission spectroscopy (UPS) experiments were carried out using a commercial PHI 5600 spectrometer equipped with two light sources. A monochromatized Al K $\alpha$  source provided photons with an energy of 1486.6 eV for XPS. Photons with an energy of 21.21 eV (He discharge lamp) were used for valence band measurements. All UPS measurements were made by applying a sample bias of  $-5$  V to obtain the correct, secondary electron cutoff that is required for determining the work function and the ionization potential. The recorded spectra were corrected for the contributions of He satellite radiation. The total energy resolution was about 350 meV (XPS)

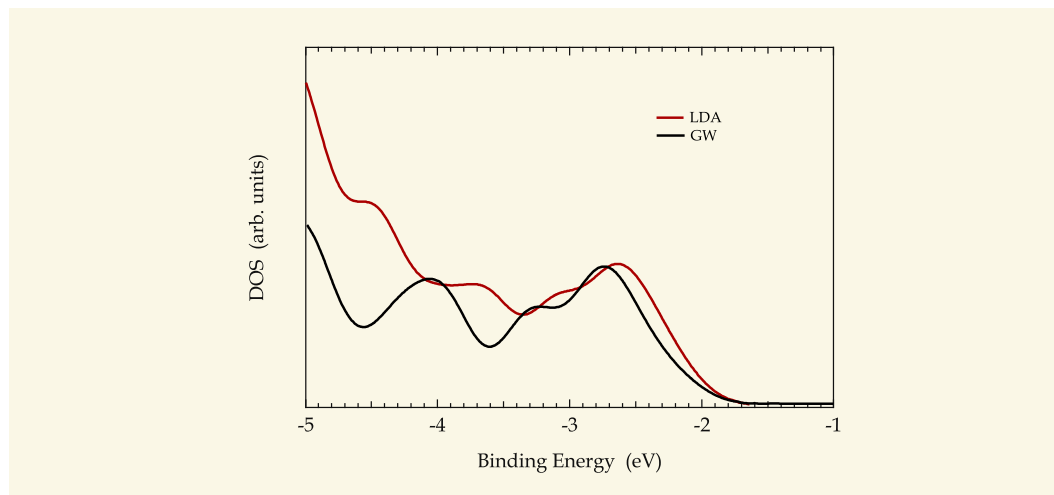
---

\*Werner Heisenberg (1901-1976). German theoretical physicist who was awarded the Nobel Prize for Physics in 1932

and 100 meV (UPS), respectively. The binding energy (BE) scale was aligned by measuring the Fermi edge (0 eV) and the Au 4f 7/2 emission feature (84.0 eV) of the polycrystalline gold substrate. For further details of cleaning the substrate and characterization of films see the literature [282].

## C.2. Theory

Experimental measurements were complemented by first-principles electronic structure calculations. Since density functional theory (DFT) in local density approximation (LDA) is known to underestimate band gaps [283], quasiparticle energies were calculated using the accurate *GW* self-energy approximation [284] of many-body perturbation theory, where the self-energy is given by the product of the Green's function  $G$  and the dynamically screened Coulomb interaction  $W$ . These quasiparticle corrections change the positions and intensities of the main peaks as shown in Fig. C.1 for picene and one can conclude that the *GW* calculations gives much better agreement with experiment. The crystal structure was optimized in LDA starting from experimental positions from [67]. The experimental loss functions were simulated in the random-phase approximation (RPA) [283], using norm-conserving pseudopotentials, including 700 LDA bands in a  $4 \times 4 \times 2$  Monkhorst-Pack grid of  $\mathbf{k}$ -points. Crystal local-field effects [283] are taken into account by inverting a matrix  $\epsilon^{-1}$  of rank 73  $\mathbf{G}$  vectors in the reciprocal space. For self-energy calculations, we have used 7000 plane waves in the expansion of the wavefunctions, 350 empty bands, a  $6 \times 6 \times 4$  Monkhorst-Pack  $\mathbf{k}$ -point grid and a plasmon-pole model approximation in the calculation of  $W$ . Quasiparticle energies are obtained as first-order corrections to LDA eigenvalues. For comparison as shown in Fig. 4.4, the calculated spectra were convoluted with a Gaussian function of half-width 0.2 eV for the PES and 0.075 eV for the EELS.



**Figure C.1.** | Comparison between LDA and *GW* densities of valence states for picene.

# Bibliography

- [1] H. Kamerlingh Onnes. *Proc. Roy. Acad. Amsterdam*. **11**, 168 (1908).
- [2] H. Kamerlingh Onnes. *Comm. Leiden*. **120b**, reprint in *Proc. K. Ned. Akad. Wet.* **13**, 1274 (1911).
- [3] K. A. Bednorz J.G. und Müller. *Zeitschrift f. Phys. B*. **64**, 186 (1986).
- [4] *The Nobel Prize in Physics 2010*. URL: [http://www.nobelprize.org/nobel\\_prizes/physics/laureates/2010/](http://www.nobelprize.org/nobel_prizes/physics/laureates/2010/) (consulted online on 23. July 2012).
- [5] A. Hebard, M. Rosseinsky, R. Haddon, D. Murphy, S. Glarum, T. Palastra, A. Ramirez, and A. Kortan. *Nature*. **350**, 600 (1991).
- [6] A. Y. Ganin, Y. Takabayashi, Y. Z. Khimyak, S. Margadonna, A. Tamai, M. J. Rosseinsky, and K. Prassides. *Nature Mater.* **7**, 367 (2008).
- [7] A. Y. Ganin, Y. Takabayashi, P. Jeglic, D. Arcon, A. Potocnik, P. J. Baker, Y. Ohishi, M. T. McDonald, M. D. Tzirakis, A. McLennan, G. R. Darling, M. Takata, M. J. Rosseinsky, and K. Prassides. *Nature*. **466**, 221 (2010).
- [8] T. E. Weller, M. Ellerby, S. S. Saxena, R. P. Smith, and N. T. Skipper. *Nat. Phys.* **1**, 39 (2005).
- [9] J. S. Kim, L. Boeri, J. R. O'Brien, F. S. Razavi, and R. K. Kremer. *Phys. Rev. Lett.* **99**, 27001 (2007).
- [10] O. Gunnarson. *Alkali Doped Fullerides*. World Scientific, Singapore (2004).
- [11] L. Van Hove. *Phys. Rev.* **95**, 249 (1954).
- [12] G. D. Mahan. *Many Particle Physics (Physics of Solids and Liquids)*. Springer; 3rd edition (2000).
- [13] R. Kubo. *J. Phys. Soc. Jpn.* **12**, 570 (1957).
- [14] W Hanke. *Adv. Phys.* **27**, 287 (1978).
- [15] H. Nyquist. *Phys. Rev.* **32**, 110 (1928).
- [16] H. B. Callen and T. A. Welton. *Phys. Rev.* **83**, 34 (1951).
- [17] W. Nolting. *Grundkurs Theoretische Physik 7: Viel-Teilchen-Theorie*. Springer Berlin Heidelberg, 7th ed. (2009).
- [18] D. Pines. *Elementary Excitations In Solids*. W. A. Benjamin, Inc. N.Y. (1963).
- [19] S Raimes. *Rep. Prog. Phys.* **20**, 1 (1957).
- [20] D. Pines. *Rev. Mod. Phys.* **28**, 184 (1956).
- [21] D. Pines and D. Bohm. *Phys. Rev.* **85**, 338 (1952).
- [22] D. Bohm and D. Pines. *Phys. Rev.* **82**, 625 (1951).

- [23] J Lindhard. *Kgl. Danske Videnskab.Selskab, Mat.-fys. Medd.* **28**, 1–57 (1954).
- [24] H. Raether. *Excitation of plasmons and interband transitions by electrons*. Springer Verlag, Berlin (1980).
- [25] M. Dressel and G. Grüner. *Electrodynamics of Solids: Optical Properties of Electrons in Matter*. Cambridge University Press; 1st edition (2002).
- [26] H. Ehrenreich and M. H. Cohen. *Phys. Rev.* **115**, 786 (1959).
- [27] S. L. Adler. *Phys. Rev.* **126**, 413 (1962).
- [28] N. Wisser. *Phys. Rev.* **129**, 62 (1963).
- [29] J. C. Fetzer. *Polycyclic Aromatic Compounds.* **27**, 143 (2007).
- [30] M. E. Gershenson, V. Podzorov, and A. F. Morpurgo. *Rev. Mod. Phys.* **78**, 973 (2006).
- [31] T. Takahashi, T. Takenobu, J. Takeya, and Y. Iwasa. *Adv. Funct. Mater.* **17**, 1623 (2007).
- [32] D. Braga and G. Horowitz. *Adv. Mater.* **21**, 1473 (2009).
- [33] H. Sirringhaus. *Adv. Mater.* **21**, 3859 (2009).
- [34] Y. Kaji, R. Mitsuhashi, X. Lee, H. Okamoto, T. Kambe, N. Ikeda, A. Fujiwara, M. Yamaji, K. Omote, and Y. Kubozono. *Org. Electron.* **10**, 432 (2009).
- [35] A. Dodabalapur, H. E. Katz, L. Torsi, and R. C. Haddon. *Science.* **269**, 1560 (1995).
- [36] S. Günes, H. Neugebauer, and N. S. Sariciftci. *Chem. Rev.* **107**, 1324 (2007).
- [37] J. J. M. Halls, C. A. Walsh, N. C. Greenham, E. A. Marseglia, R. H. Friend, S. C. Moratti, and A. B. Holmes. *Nature.* **376**, 498 (1995).
- [38] C. W. Schlenker, V. S. Barlier, S. W. Chin, M. T. Whited, R. E. McAnally, S. R. Forrest, and M. E. Thompson. *Chem. Mater.* **23**, 4132 (2011).
- [39] R. H. Friend, R. W. Gymer, A. B. Holmes, J. H. Burroughes, R. N. Marks, C. Taliani, D. D. C. Bradley, D. A. D. Santos, J. L. Bredas, M. Logdlund, and W. R. Salaneck. *Nature.* **397**, 121 (1999).
- [40] C. Adachi, M. A. Baldo, M. E. Thompson, and S. R. Forrest. *J. Appl. Phys.* **90**, 5048 (2001).
- [41] C. Weichsel, S. Reineke, M. Furno, B. Lussem, and K. Leo. *J. Appl. Phys.* **111**, 33102 (2012).
- [42] Z. Vardeny. *Organic spintronics*. CRC Press (2010).
- [43] W. J. M. Naber, S Faez, and W. G. van der Wiel. *J. Phys. D: Appl. Phys.* **40**, R205 (2007).
- [44] V. A. Dediu, L. E. Hueso, I. Bergenti, and C. Taliani. *Nat. Mater.* **8**, 707 (2009).
- [45] O. Gunnarsson. *Rev. Mod. Phys.* **69**, 575 (1997).
- [46] M. Knupfer. *Surf. Sci. Rep.* **42**, 1 (2001).
- [47] M. Craciun, S Rogge, M. den Boer, S Margadonna, K Prassides, Y Iwasa, and A. Morpurgo. *Adv. Mater.* **18**, 320 (2006).

- [48] H. Rauf, T. Pichler, M. Knupfer, J. Fink, and H. Kataura. *Phys. Rev. Lett.* **93**, 96805 (2004).
- [49] M. F. Craciun, G. Giovannetti, S. Rogge, G. Brocks, A. F. Morpurgo, and J. van den Brink. *Phys. Rev. B.* **79**, 125116 (2009).
- [50] F. Roth, A. König, R. Kraus, and M. Knupfer. *J. Chem. Phys.* **128**, 194711 (2008).
- [51] E. Tosatti, M. Fabrizio, J. Tóbiš, and G. E. Santoro. *Phys. Rev. Lett.* **93**, 117002 (2004).
- [52] H. Sponer, G. Nordheim, A. L. Sklar, and E. Teller. *J. Chem. Phys.* **7**, 207 (1939).
- [53] F. B. Mallory, K. E. Butler, A. C. Evans, E. J. Brondyke, C. W. Mallory, C. Yang, and A. Ellenstein. *J. Am. Chem. Soc.* **119**, 2119 (1997).
- [54] C. Tönshoff and H. Bettinger. *Angew. Chem. Int. Ed.* **49**, 4125 (2010).
- [55] G. Portella, J. Poater, J. M. Bofill, P. Alemany, and M. Solà. *J. Org. Chem.* **70**, 2509 (2005).
- [56] *Verordnung (EG) Nr. 1272/2008 des europäischen Parlaments und des Rates über die Einstufung, Kennzeichnung und Verpackung von Stoffen und Gemischen.* URL: <http://eur-lex.europa.eu/LexUriServ/LexUriServ.do?uri=OJ:L:2008:353:0001:1355:DE:PDF> (2008).
- [57] *IARC Monographs on the Evaluation of Carcinogenic Risks to Humans, Volume 92.* URL: <http://monographs.iarc.fr/ENG/Monographs/vol92/mono92-10.pdf> (2010).
- [58] W. Demtröder. *Atoms, Molecules and Photons: An Introduction to Atomic- Molecular- and Quantum Physics.* Springer Berlin Heidelberg; 1st edition (2005).
- [59] J. E. Jones. *Proc. Roy. Soc. of London A.* **106**, 463 (1924).
- [60] R. A. Buckingham and J. Corner. *Proc. Roy. Soc. of London A.* **189**, 118 (1947).
- [61] T. Yamamoto, S. Nakatani, T. Nakamura, K. ichi Mizuno, A. H. Matsui, Y. Akahama, and H. Kawamura. *Chem. Phys.* **184**, 247 (1994).
- [62] R. Totoki, T. Aoki-Matsumoto, and K. Mizuno. *J. Lumin.* **112**, 308 (2005).
- [63] S. Nakatani, T. Nakamura, K. Mizuno, and A. Matsui. *J. Lumin.* **58**, 343 (1994).
- [64] J. M. Robertson and J. G. White. *J. Chem. Soc.* 925 (1956).
- [65] J. Iball, C. H. Morgan, and D. E. Zacharias. *J. Chem. Soc., Perkin Trans. 2.* 1271 (1975).
- [66] D. M. Burns and J. Iball. *Proc. R. Soc. London. Ser. A.* **257**, 491 (1960).
- [67] A. De, R. Ghosh, S. Roychowdhury, and P. Roychowdhury. *Acta Crystallogr. Sec. C.* **41**, 907 (1985).
- [68] T. Echigo, M. Kimata, and T. Maruoka. *Am. Miner.* **92**, 1262 (2007).
- [69] D. Holmes, S. Kumaraswamy, A. J. Matzger, and K. P. C. Vollhardt. *Chem. Eur. J.* **5**, 3399 (1999).
- [70] J. M. Robertson, V. C. Sinclair, and J. Trotter. *Acta Crystall.* **14**, 697 (1961).
- [71] R. B. Campbell, J. M. Robertson, and J. Trotter. *Acta Crystall.* **15**, 289 (1962).

- [72] U. Sondermann, A. Kutoglu, and H. Bassler. *J. Phys. Chem.* **89**, 1735 (1985).
- [73] C. C. Mattheus, A. B. Dros, J. Baas, G. T. Oostergetel, A. Meetsma, J. L. de Boer, and T. T. Palstra. *Synth. Met.* **138**, 475 (2003).
- [74] C. C. Mattheus, A. B. Dros, J. Baas, A. Meetsma, J. L. d. Boer, and T. T. M. Palstra. *Acta Crystallogr., Sec. C.* **57**, 939 (2001).
- [75] A. Kitaigorodskii. *Molecular crystals and molecules*. Academic Press, New York (1973).
- [76] A. S. Myerson. *Molecular Modeling Applications in Crystallization*. Cambridge University Press (2005).
- [77] J. Wright. *Molecular Crystals*. Cambridge University Press, 2nd edition (1994).
- [78] G. R. Desiraju and A. Gavezzotti. *Acta Crystallogr., Sect. B.* **45**, 473 (1989).
- [79] A. C. Hazell, F. K. Larsen, and M. S. Lehmann. *Acta Crystallogr., Sect. B.* **28**, 2977 (1972).
- [80] J. M. Robertson. *Rev. Mod. Phys.* **30**, 155 (1958).
- [81] E. Silinsh. *Organic Molecular Crystals. Their Electronic States*. Springer Verlag, Berlin (1980).
- [82] M. Schwoerer and H. Wolf. *Organische Molekulare Festkörper: Einführung in die Physik von pi-Systemen*. Wiley-VCH Verlag GmbH & Co. KGaA, Weinheim (2005).
- [83] A. J. Lovinger, S. R. Forrest, M. L. Kaplan, P. H. Schmidt, and T. Venkatesan. *J. Appl. Phys.* **55**, 476 (1984).
- [84] R. B. Campbell, J. M. Robertson, and J. Trotter. *Acta Crystallogr.* **14**, 705 (1961).
- [85] T. Siegrist, C. Kloc, J. H. Schön, B. Batlogg, R. C. Haddon, S. Berg, and G. A. Thomas. *Angew. Chemie.* **40**, 1732 (2001).
- [86] T. Siegrist, C. Besnard, S. Haas, M. Schiltz, P. Pattison, D. Chernyshov, B. Batlogg, and C. Kloc. *Adv. Mater.* **19**, 2079 (2007).
- [87] T. Minakata, H. Imai, M. Ozaki, and K. Saco. *J. Appl. Phys.* **72**, 5220 (1992).
- [88] C. D. Dimitrakopoulos, A. R. Brown, and A. Pomp. *J. Appl. Phys.* **80**, 2501 (1996).
- [89] C. Kittel. *Introduction to Solid State Physics*. Wiley John + Sons Inc., New York, 8th Edition (2005).
- [90] J. Frenkel. *Phys. Rev.* **37**, 1276 (1931).
- [91] M. Pope and C. E. Swenberg. *Electronic processes in organic crystals and polymers*. Oxford University Press, Second Edition, New York (1999).
- [92] M. Knupfer. *Appl. Phys. A.* **77**, 623 (2003).
- [93] K. B. Wiberg. *J. Org. Chem.* **62**, 5720 (1997).
- [94] E. Clar. *Aromatische Kohlenwasserstoffe*. Springer Verlag, Berlin, 2nd Edition (1952).
- [95] H. B. Klevens and J. R. Platt. *J. Chem. Phys.* **17**, 470 (1949).



- [96] D. Biermann and W. Schmidt. *J. Am. Chem. Soc.* **102**, 3163 (1980).
- [97] D. Biermann and W. Schmidt. *J. Am. Chem. Soc.* **102**, 3173 (1980).
- [98] E. Clar. *The Aromatic Sextet*. John Wiley & Sons Ltd., London (1972).
- [99] E. Clar. *Polycyclic Hydrocarbons*. Academic Press, London-New York and Springer-Verlag, Berlin-Göttingen-Heidelberg (1964).
- [100] N. B. Hannay, T. H. Geballe, B. T. Matthias, K. Andres, P. Schmidt, and D. MacNair. *Phys. Rev. Lett.* **14**, 225 (1965).
- [101] I. Belash, A. Bronnikov, O. Zharikov, and A. Palnichenko. *Solid State Commun.* **64**, 1445 (1987).
- [102] I. Belash, A. Bronnikov, O. Zharikov, and A. Palnichenko. *Solid State Commun.* **69**, 921 (1989).
- [103] I. Belash, A. Bronnikov, O. Zharikov, and A. Palnichenko. *Synth. Met.* **36**, 283 (1990).
- [104] I. Belash, O. Zharikov, and A. Palnichenko. *Synth. Met.* **34**, 455 (1990).
- [105] N. Emery, C. Hérold, M. d'Astuto, V. Garcia, C. Bellin, J. F. Marêché, P. Lagrange, and G. Loupiau. *Phys. Rev. Lett.* **95**, 87003 (2005).
- [106] D. Jerome, A. Mazaud, M. Ribault, and K. Bechgaard. *J. Phys. Lett.* **41**, L95–L98 (1980).
- [107] D. Jerome. *Physica B+C*. **109–110, Part 3**, 1447 (1982).
- [108] E. Yagubskii, I. Shchegolev, V. Laukhin, P. Kononovich, M. Kartsovnik, A. Zvarykina, and L. Buravov. *JETP Lett.* **39**, 12 (1984).
- [109] M. Tokumoto, K. Murata, H. Bando, H. Anzai, G. Saito, K. Kajimura, and T. Ishiguro. *Solid State Commun.* **54**, 1031 (1985).
- [110] J. S. Kukulski and L. Pauling. *American Mineralogist*. **35**, 125 (1950).
- [111] W. I. F. David, R. M. Ibberson, J. C. Matthewman, K. Prassides, T. J. S. Dennis, J. P. Hare, H. W. Kroto, R. Taylor, and D. R. M. Walton. *Nature*. **353**, 147 (1991).
- [112] J. Fayos. *J. Solid State Chem.* **148**, 278 (1999).
- [113] K. Tanigaki, T. Ebbesen, S. Saito, J. Mizuki, J. Tsai, Y. Kubo, and S. Kuroshima. *Nature*. **352**, 222 (1991).
- [114] T. Palstra, O. Zhou, Y. Iwasa, P. Sulewski, R. Fleming, and B. Zegarski. *Solid State Commun.* **93**, 327 (1995).
- [115] O. Zhou, Q. Zhu, J. E. Fischer, N. Coustel, G. B. M. Vaughan, P. A. Heiney, J. P. McCauley, and A. B. Smith. *Science*. **255**, 833 (1992).
- [116] J. Bardeen, L. N. Cooper, and J. R. Schrieffer. *Phys. Rev.* **108**, 1175 (1957).
- [117] J. Bardeen, L. N. Cooper, and J. R. Schrieffer. *Phys. Rev.* **106**, 162 (1957).
- [118] J. E. Han, O. Gunnarsson, and V. H. Crespi. *Phys. Rev. Lett.* **90**, 167006 (2003).
- [119] M. Tezuka, R. Arita, and H. Aoki. *Phys. Rev. Lett.* **95**, 226401 (2005).

- [120] T. Ishiguro, K. Yamaji, and G. Saito. *Organic Superconductors*. Springer, 2nd ed. (1998).
- [121] M. Baenitz. *Physik in unserer Zeit*. **30**, 167 (1999).
- [122] E. A. Ekimov, V. A. Sidorov, E. D. Bauer, N. N. Mel'nik, N. J. Curro, J. D. Thompson, and S. M. Stishov. *Nature*. **428**, 542 (2004).
- [123] Y. Takano, T. Takenouchi, S. Ishii, S. Ueda, T. Okutsu, I. Sakaguchi, H. Umezawa, H. Kawarada, and M. Tachiki. *Diamond Relat. Mater.* **16**, 911 (2007).
- [124] A. Schilling, M. Cantoni, J. D. Guo, and H. R. Ott. *Nature*. **363**, 56 (1993).
- [125] C. W. Chu, L. Gao, F. Chen, Z. J. Huang, R. L. Meng, and Y. Y. Xue. *Nature*. **365**, 323 (1993).
- [126] Z.-A. Ren, G.-C. Che, X.-L. Dong, J. Yang, W. Lu, W. Yi, X.-L. Shen, Z.-C. Li, L.-L. Sun, F. Zhou, and Z.-X. Zhao. *Europhys. Lett.* **83**, 17002 (2008).
- [127] R. Zhi-An, L. Wei, Y. Jie, Y. Wei, S. Xiao-Li, Zheng-Cai, C. Guang-Can, D. Xiao-Li, S. Li-Ling, Z. Fang, and Z. Zhong-Xian. *Chin. Phys. Lett.* **25**, 2215 (2008).
- [128] J. Nagamatsu, N. Nakagawa, T. Muranaka, Y. Zenitani, and J. Akimitsu. *Nature*. **410**, 63 (2001).
- [129] R. Mitsuhashi, Y. Suzuki, Y. Yamanari, H. Mitamura, T. Kambe, N. Ikeda, H. Okamoto, A. Fujiwara, M. Yamaji, N. Kawasaki, Y. Maniwa, and Y. Kubozono. *Nature*. **464**, 76 (2010).
- [130] F. Roth, M. Gatti, P. Cudazzo, M. Grobosch, B. Mahns, B. Büchner, A. Rubio, and M. Knupfer. *New J. Phys.* **12**, 103036 (2010).
- [131] N. Sato, H. Inokuchi, and E. A. Silinsh. *Chem. Phys.* **115**, 269 (1987).
- [132] T. Kosugi, T. Miyake, S. Ishibashi, R. Arita, and H. Aoki. *Phys. Rev. B*. **84**, 214506 (2011).
- [133] P. L. de Andres, A. Guijarro, and J. A. Vergés. *Phys. Rev. B*. **83**, 245113 (2011).
- [134] M. Kim, B. I. Min, G. Lee, H. J. Kwon, Y. M. Rhee, and J. H. Shim. *Phys. Rev. B*. **83**, 214510 (2011).
- [135] *Photo from Yoshihiro Kubozono taken from an article published by Saswato R. Das in IEEE Spektrum. Inside Technology.* URL: <http://spectrum.ieee.org/energy/the-smarter-grid/hydrocarbon-superconductor-discovered> (2010).
- [136] X. Wang, R. Liu, Z. Gui, Y. Xie, Y. Yan, J. Ying, X. Luo, and X. Chen. *Nat. Commun.* **2**, 507 (2011).
- [137] X. F. Wang, Y. J. Yan, Z. Gui, R. H. Liu, J. J. Ying, X. G. Luo, and X. H. Chen. *Phys. Rev. B*. **84**, 214523 (2011).
- [138] X. F. Wang, X. G. Luo, J. J. Ying, Z. J. Xiang, S. L. Zhang, R. R. Zhang, Y. H. Zhang, Y. J. Yan, A. F. Wang, P. Cheng, G. J. Ye, and X. H. Chen. arXiv:1203.5887 (2012).

- [139] Y. Kubozono, H. Mitamura, X. Lee, X. He, Y. Yamanari, Y. Takahashi, Y. Suzuki, Y. Kaji, R. Eguchi, K. Akaike, T. Kambe, H. Okamoto, A. Fujiwara, T. Kato, T. Kosugi, and H. Aoki. *Phys. Chem. Chem. Phys.* **13**, 16476 (2011).
- [140] J. Dopfer and H. Wynberg. *Tetrahedron Lett.* **13**, 763 (1972).
- [141] R. G. Lawton and W. E. Barth. *J. Am. Chem. Soc.* **93**, 1730 (1971).
- [142] F. Diederich and H. A. Staab. *Angew. Chem. Int. Ed. Engl.* **17**, 372 (1978).
- [143] H. A. Staab and F. Diederich. *Chem. Ber.* **116**, 3487 (1983).
- [144] M. Xue, T. Cao, D. Wang, Y. Wu, H. Yang, X. Dong, J. He, F. Li, and G. F. Chen. *Sci. Rep.* **2**, 1 (2012).
- [145] T. Kosugi, T. Miyake, S. Ishibashi, R. Arita, and H. Aoki. *J. Phys. Soc. Jpn.* **78**, 113704 (2009).
- [146] M. J. Rosseinsky and K. Prassides. *Nature.* **464**, 39 (2010).
- [147] T. Kato, T. Kambe, and Y. Kubozono. *Phys. Rev. Lett.* **107**, 77001 (2011).
- [148] A. Subedi and L. Boeri. *Phys. Rev. B.* **84**, 20508 (2011).
- [149] G. Giovannetti and M. Capone. *Phys. Rev. B.* **83**, 134508 (2011).
- [150] M. Casula, M. Calandra, G. Profeta, and F. Mauri. *Phys. Rev. Lett.* **107**, 137006 (2011).
- [151] P. Cudazzo, M. Gatti, F. Roth, B. Mahns, M. Knupfer, and A. Rubio. *Phys. Rev. B.* **84**, 155118 (2011).
- [152] T. Sato, N. Iwahara, and K. Tanaka. *Phys. Rev. B.* **85**, 161102 (2012).
- [153] M. Krasinkova. *J. Supercond. Nov. Magn.* **24**, 1419 (2011).
- [154] R. Pekoz and S. Erkoç. *Adv. Sci. Lett.* **3**, 43 (2010).
- [155] Y. Nomura, K. Nakamura, and R. Arita. *Phys. Rev. B.* **85**, 155452 (2012).
- [156] A. Girlando, M. Masino, I. Bilotti, A. Brillante, R. G. D. Valle, and E. Venuti. *Phys. Chem. Chem. Phys.* **14**, 1694 (2012).
- [157] Y. Wang, S. D. Motta, F. Negri, and R. Friedlein. *J. Am. Chem. Soc.* **133**, 10054 (2011).
- [158] H. Okazaki, T. Wakita, T. Muro, Y. Kaji, X. Lee, H. Mitamura, N. Kawasaki, Y. Kubozono, Y. Yamanari, T. Kambe, T. Kato, M. Hirai, Y. Muraoka, and T. Yokoya. *Phys. Rev. B.* **82**, 195114 (2010).
- [159] P. L. de Andres, A. Guijarro, and J. A. Vergés. *Phys. Rev. B.* **84**, 144501 (2011).
- [160] J. A. Vergés, P. L. de Andres, E. San-Fabián, G. Chiappe, E. Louis, and A. Guijarro. *Phys. Rev. B.* **85**, 165102 (2012).
- [161] F. Aiga. *J. Phys. Chem. A.* **116**, 663 (2012).
- [162] Y. Kasahara, Y. Takeuchi, and Y. Iwasa. *Phys. Rev. B.* **85**, 214520 (2012).
- [163] J. Ying, X. Wang, Y. Yan, Z. Xiang, X. Luo, Z. Sun, and X. Chen. *Phys. Rev. B.* **85**, 180511 (2012).

- [164] T. Kosugi, T. Miyake, S. Ishibashi, R. Arita, and H. Aoki. *Phys. Rev. B.* **84**, 20507 (2011).
- [165] M. Knupfer. *Carbon.* **37**, 733 (1999).
- [166] E. L. Shirley. *Phys. Rev. Lett.* **80**, 794 (1998).
- [167] J. A. Soininen, A. L. Ankudinov, and J. J. Rehr. *Phys. Rev. B.* **72**, 45136 (2005).
- [168] P. Livins, T. Aton, and S. E. Schnatterly. *Phys. Rev. B.* **38**, 5511 (1988).
- [169] J. B. Gallivan and J. S. Brinen. *J. Chem. Phys.* **50**, 1590 (1969).
- [170] L. Ruzicka and E. Mörgeli. *Helv. Chim. Acta.* **19**, 377 (1936).
- [171] R. W. Lof, M. A. van Veenendaal, B. Koopmans, H. T. Jonkman, and G. A. Sawatzky. *Phys. Rev. Lett.* **68**, 3924 (1992).
- [172] I. Hill, A. Kahn, Z. Soos, R. Pascal, and Jr. *Chem. Phys. Lett.* **327**, 181 (2000).
- [173] M. L. Tiago, J. E. Northrup, and S. G. Louie. *Phys. Rev. B.* **67**, 115212 (2003).
- [174] D. R. Zahn, G. N. Gavril, and M. Gorgoi. *Chem. Phys.* **325**, 99 (2006).
- [175] K. Hummer and C. Ambrosch-Draxl. *Phys. Rev. B.* **71**, 81202 (2005).
- [176] F. Amy, C. Chan, and A. Kahn. *Org. Electron.* **6**, 85 (2005).
- [177] M. Dressel, B. Gompf, D. Faltermeier, A. K. Tripathi, J. Pflaum, and M. Schubert. *Opt. Express.* **16**, 19770 (2008).
- [178] R. Schuster, M. Knupfer, and H. Berger. *Phys. Rev. Lett.* **98**, 37402 (2007).
- [179] M. Hoffmann, K. Schmidt, T. Fritz, T. Hasche, V. M. Agranovich, and K. Leo. *Chemical Physics.* **258**, 73 (2000).
- [180] M. Knupfer, T. Schwieger, H. Peisert, and J. Fink. *Phys. Rev. B.* **69**, 165210 (2004).
- [181] Y Tokura, T Koda, Y Iyechika, and H Kuroda. *Chem. Phys. Lett.* **102**, 174 (1983).
- [182] M. Knupfer, T. Pichler, M. S. Golden, J. Fink, M. Murgia, R. H. Michel, R. Zamboni, and C. Taliani. *Phys. Rev. Lett.* **83**, 1443 (1999).
- [183] M. Knupfer and J. Fink. *Phys. Rev. B.* **60**, 10731 (1999).
- [184] M. Knupfer, J. Fink, E. Zojer, G. Leising, and D. Fichou. *Chem. Phys. Lett.* **318**, 585 (2000).
- [185] M. W. Haverkort, A. Tanaka, L. H. Tjeng, and G. A. Sawatzky. *Phys. Rev. Lett.* **99**, 257401 (2007).
- [186] M Knupfer, J Fink, J. Armbruster, and H. Romberg. *Z. Phys. B.* **98**, 9 (1995).
- [187] C. Chen, L. Tjeng, P Rudolf, G Meigs, J. Rowe, J Chen, J. McCauley, A. Smith, A. McGhie, W. Romanow, and E. Plummer. *Nature.* **352**, 603 (1991).
- [188] B. Wästberg, S. Lunell, C. Enkvist, P. A. Brühwiler, A. J. Maxwell, and N. Mårtensson. *Phys. Rev. B.* **50**, 13031 (1994).
- [189] E. Sohmen, J. Fink, and W. Krätschmer. *Z. Phys. B-Condens. Mat.* **86**, 87 (1992).

- [190] P. G. Schroeder, C. B. France, B. A. Parkinson, and R. Schlaf. *J. Appl. Phys.* **91**, 9095 (2002).
- [191] D. Poirier, T. Ohno, G. Kroll, Y. Chen, P. Benning, J. Weaver, L. Chibante, and R. Smalley. *Science*. **253**, 646 (1991).
- [192] M. A. Khakoo, J. M. Ratliff, and S. Trajmar. *J. Chem. Phys.* **93**, 8616 (1990).
- [193] R. Abouaf and S. Diaz-Tendero. *Phys. Chem. Chem. Phys.* **11**, 5686 (2009).
- [194] N. Nijegorodov, R. Mabbs, and W. Downey. *Spectrochim. Acta Part A*. **57**, 2673 (2001).
- [195] K. Ohno, H. Inokuchi, and T. Kajiwara. *Bull. Chem. Soc. Jpn.* **45**, 996 (1972).
- [196] R. Rieger, M. Kastler, V. Enkelmann, and K. Müllen. *Chem. Eur. J.* **14**, 6322 (2008).
- [197] P. I. Djurovich, E. I. Mayo, S. R. Forrest, and M. E. Thompson. *Org. Electron.* **10**, 515 (2009).
- [198] J. Tanaka. *Bull. Chem. Soc. Japan*. **38**, 86 (1965).
- [199] N. Sato, K. Seki, and H. Inokuchi. *J. Chem. Soc., Faraday Trans. 2*. **77**, 1621 (1981).
- [200] P. K. Nayak and N. Periasamy. *Org. Electron.* **10**, 1396 (2009).
- [201] A. Davydov. *Theory of Molecular Excitons*. Plenum Press, New York (1971).
- [202] K. Hiruta, S. Tokita, and K. Nishimoto. *Dyes Pigments*. **34**, 273 (1997).
- [203] H. Yamagata, J. Norton, E. Hontz, Y. Olivier, D. Beljonne, J. L. Bredas, R. J. Silbey, and F. C. Spano. *J. Chem. Phys.* **134**, 204703 (2011).
- [204] A. Bree and L. E. Lyons. *J. Chem. Soc.* 5206 (1960).
- [205] V. Zanker and J. Preuss. *Z. Angew. Phys.* **27**, 363 (1969).
- [206] S. Tavazzi, L. Raimondo, L. Silvestri, P. Spearman, A. Camposeo, M. Polo, and D. Pisignano. *J. Chem. Phys.* **128**, 154709 (2008).
- [207] L. Carreira, T. Maguire, and T. B. M. Jr.. *Spectrochimica Acta A*. **42**, 343 (1986).
- [208] L. Sebastian, G. Weiser, and H. Bässler. *Chem. Phys.* **61**, 125 (1981).
- [209] E. V. Tsiper and Z. G. Soos. *Phys. Rev. B*. **68**, 85301 (2003).
- [210] M. Hoffmann, K. Schmidt, T. Fritz, T. Hasche, V. M. Agranovich, and K. Leo. *Chem. Phys.* **258**, 73 (2000).
- [211] L. Gisslén and R. Scholz. *Phys. Rev. B*. **83**, 155311 (2011).
- [212] M. Knupfer, T. Schwieger, J. Fink, K. Leo, and M. Hoffmann. *Phys. Rev. B*. **66**, 35208 (2002).
- [213] K. Hummer and C. Ambrosch-Draxl. *Phys. Rev. B*. **72**, 205205 (2005).
- [214] S. Sharifzadeh, A. Biller, L. Kronik, and J. B. Neaton. *Phys. Rev. B*. **85**, 125307 (2012).
- [215] F. Roth, R. Schuster, A. König, M. Knupfer, and H. Berger. *J. Chem. Phys.* **136**, 204708 (2012).

- [216] N. Koch, I. Salzmann, R. Johnson, J. Pflaum, R. Friedlein, and J. Rabe. *Org. Electron.* **7**, 537 (2006).
- [217] A. Vollmer, H. Weiss, S. Rentenberger, I. Salzmann, J. Rabe, and N. Koch. *Surf. Sci.* **600**, 4004 (2006).
- [218] M. Grobosch, C. Schmidt, W. Naber, W. van der Wiel, and M. Knupfer. *Synth. Met.* **160**, 238 (2010).
- [219] A. Briley, M. R. Pederson, K. A. Jackson, D. C. Patton, and D. V. Porezag. *Phys. Rev. B.* **58**, 1786 (1998).
- [220] M. R. Pederson and K. A. Jackson. *Phys. Rev. B.* **41**, 7453 (1990).
- [221] M. Pederson, D. Porezag, J. Kortus, and D. Patton. *Phys. Status Solidi.* **217**, 197 (2000).
- [222] D. Porezag and M. R. Pederson. *Phys. Rev. A.* **60**, 2840 (1999).
- [223] A. A. Quong, M. R. Pederson, and J. L. Feldman. *Solid State Commun.* **87**, 535 (1993).
- [224] E. Clar. *Berichte der deutschen chemischen Gesellschaft (A and B Series).* **76**, 257 (1943).
- [225] E. Clar. *Zeitschrift für Chemie.* **2**, 35 (1962).
- [226] H. H. Perkampus and L. Pohl. *Theo. Chim. Acta.* **1**, 116 (1963).
- [227] D. Faltermeier, B. Gompf, M. Dressel, A. K. Tripathi, and J. Pflaum. *Phys. Rev. B.* **74**, 125416 (2006).
- [228] G. Giovannetti, G. Brocks, and J. van den Brink. *Phys. Rev. B.* **77**, 35133 (2008).
- [229] H. Tou, Y. Maniwa, Y. Iwasa, H. Shimoda, and T. Mitani. *Phys. Rev. B.* **62**, R775–R778 (2000).
- [230] H. Kitano, R. Matsuo, K. Miwa, A. Maeda, T. Takenobu, Y. Iwasa, and T. Mitani. *Phys. Rev. Lett.* **88**, 96401 (2002).
- [231] P. Durand, G. R. Darling, Y. Dubitsky, A. Zaopo, and M. J. Rosseinsky. *Nat. Mater.* **2**, 605 (2003).
- [232] M. Knupfer and J. Fink. *Phys. Rev. Lett.* **79**, 2714 (1997).
- [233] Y. Nomura, K. Nakamura, and R. Arita. *Phys. Rev. B.* **85**, 155452 (2012).
- [234] M. Knupfer, D. M. Poirier, and J. H. Weaver. *Phys. Rev. B.* **49**, 8464 (1994).
- [235] M. J. Rosseinsky. *J. Mater. Chem.* **5**, 1497 (1995).
- [236] T. Pichler, R. Winkler, and H. Kuzmany. *Phys. Rev. B.* **49**, 15879 (1994).
- [237] H. Kuzmany, R. Winkler, and T. Pichler. *J. Phys.: Cond. Mat.* **7**, 6601 (1995).
- [238] P. J. Benning, D. M. Poirier, T. R. Ohno, Y. Chen, M. B. Jost, F. Stepniak, G. H. Kroll, J. H. Weaver, J. Fure, and R. E. Smalley. *Phys. Rev. B.* **45**, 6899 (1992).
- [239] D. M. Poirier, D. W. Owens, and J. H. Weaver. *Phys. Rev. B.* **51**, 1830 (1995).
- [240] B. Mahns, F. Roth, and M. Knupfer. *J. Chem. Phys.* **136**, 134503 (2012).

- [241] M. Sing, V. G. Grigoryan, G. Paasch, M. Knupfer, J. Fink, B. Lommel, and W. Aßmus. *Phys. Rev. B.* **59**, 5414 (1999).
- [242] S.-I. Machida, Y. Nakayama, S. Duhm, Q. Xin, A. Funakoshi, N. Ogawa, S. Kera, N. Ueno, and H. Ishii. *Phys. Rev. Lett.* **104**, 156401 (2010).
- [243] R. Temirov, S. Soubatch, A. Luican, and F. S. Tautz. *Nature.* **444**, 350 (2006).
- [244] N. Ueno and S. Kera. *Prog. Surf. Sci.* **83**, 490 (2008).
- [245] K. Doi, K. Yoshida, H. Nakano, A. Tachibana, T. Tanabe, Y. Kojima, and K. Okazaki. *J. Appl. Phys.* **98**, 113709 (2005).
- [246] O Gunnarsson, V Eyert, M Knupfer, J Fink, and J. Armbruster. *J. Phys.: Condens. Matter.* **8**, 2557 (1996).
- [247] Y. Iwasa, K. Tanaka, T. Yasuda, T. Koda, and S. Koda. *Phys. Rev. Lett.* **69**, 2284 (1992).
- [248] L. Degiorgi, E. J. Nicol, O. Klein, G. Grüner, P. Wachter, S.-M. Huang, J. Wiley, and R. B. Kaner. *Phys. Rev. B.* **49**, 7012 (1994).
- [249] K. Sturm. *Adv. Phys.* **31**, 1 (1982).
- [250] J. Sprösser-Prou, A. vom Felde, and J. Fink. *Phys. Rev. B.* **40**, 5799 (1989).
- [251] A. vom Felde, J. Sprösser-Prou, and J. Fink. *Phys. Rev. B.* **40**, 10181 (1989).
- [252] P. F. Williams and A. N. Bloch. *Phys. Rev. B.* **10**, 1097 (1974).
- [253] V. V. Kresin and V. Z. Kresin. *Phys. Rev. B.* **49**, 2715 (1994).
- [254] Y. Ma, P. Rudolf, C. T. Chen, and F. Sette. *J. Vac. Sci. Technol. A.* **10**, 1965 (1992).
- [255] T Sato, H Tanaka, A Yamamoto, Y Kuzumoto, and K Tokunaga. *Chem. Phys.* **287**, 91 (2003).
- [256] P. A. Lane, X. Wei, and Z. V. Vardeny. *Phys. Rev. Lett.* **77**, 1544 (1996).
- [257] M. Golden, M. Knupfer, J. Fink, J. Armbruster, T. Cummins, H. Romberg, M. Roth, M. Sing, M. Schmidt, and E. Sohmen. *J. Phys.-Condes. Matter.* **7**, 8219 (1995).
- [258] A. König, F. Roth, R. Kraus, and M. Knupfer. *J. Chem. Phys.* **130**, 214503 (2009).
- [259] B. Mahns, F. Roth, M. Grobosch, D. R. T. Zahn, and M. Knupfer. *J. Chem. Phys.* **134**, 194504 (2011).
- [260] G. G. Fuentes and M. Knupfer. *Phys. Rev. B.* **70**, 233202 (2004).
- [261] J. Tsutsumi, H. Yoshida, R. Murdey, S. Kato, and N. Sato. *J. Phys. Chem. A.* **113**, 9207 (2009).
- [262] K. Ishii, M. Kinoshita, and H. Kuroda. *Bull. Chem. Soc. Japan.* **46**, 3385 (1973).
- [263] A. W. Hofmann. *Proc. R. Soc. Lond.* **8**, 1 (1856).
- [264] A. Kekulé. *Justus Liebigs Ann. Chem.* **162**, 77 (1872).
- [265] K. Lonsdale. *Proc. R. Soc. A.* **123**, 494 (1929).
- [266] K. Lonsdale. *Proc. R. Soc. A.* **133**, 536 (1931).

- [267] E. Hückel. *Z. Phys. A.* **70**, 204 (1931).
- [268] E. Hückel. *Z. Phys. A.* **72**, 310 (1931).
- [269] E. Hückel. *Z. Phys. A.* **76**, 628 (1932).
- [270] J. D. Roberts, A. Streitwieser, and C. M. Regan. *J. Am. Chem. Soc.* **74**, 4579 (1952).
- [271] J. W. Armit and R. Robinson. *J. Chem. Soc., Trans.* **127**, 1604 (1925).
- [272] E. Clar. *Tetrahedron.* **5**, 98 (1959).
- [273] E. Clar. *Tetrahedron.* **6**, 355 (1959).
- [274] E. Clar and W. Kelly. *J. Am. Chem. Soc.* **76**, 3502 (1954).
- [275] I. Gutman and S. Cyvin. *Introduction to the Theory of Benzenoid Hydrocarbons*. Springer, Berlin (1989).
- [276] M. D. Watson, A. Fechtenkötter, and K. Müllen. *Chem. Rev.* **101**, 1267 (2001).
- [277] O. E. Polansky and G. Derflinger. *J. Quantum Chem.* **1**, 379 (1967).
- [278] H. Zhu and Y. Jiang. *Chem. Phys. Lett.* **193**, 446 (1992).
- [279] Z. B. Maksić, D. Barić, and T. Müller. *J. Phys. Chem. A.* **110**, 10135 (2006).
- [280] R. G. Harvey. *Polycyclic Aromatic Hydrocarbons*. Wiley John + Sons Inc., New York, 1st Edition (1997).
- [281] M. Randić. *Chem. Rev.* **103**, 3449 (2003).
- [282] H. Peisert, M. Knupfer, T. Schwieger, G. G. Fuentes, D. Olligs, J. Fink, and T. Schmidt. *J. Appl. Phys.* **93**, 9683 (2003).
- [283] G. Onida, L. Reining, and A. Rubio. *Rev. Mod. Phys.* **74**, 601 (2002).
- [284] L. Hedin. *Phys. Rev.* **139**, A796–A823 (1965).



## List Of Publications

- (1) F. Roth, B. Mahns, S. Hampel, M. Nohr, H. Berger, B. Büchner & M. Knupfer "Exciton properties of selected aromatic hydrocarbon systems" *Eur. Phys. J. B*, **86**, 66 (2013).
- (2) S. Lindner, B. Mahns, A. König, F. Roth, M. Knupfer, R. Friedrich, T. Hahn & J. Kortus "Phthalocyanine dimers in a blend: spectroscopic and theoretical studies of  $\text{MnPc}^{\delta+}/\text{F16CoPc}^{\delta-}$ " *J. Chem. Phys.*, **138**, 024707 (2013).
- (3) F. Roth, B. Mahns, R. Schönfelder, S. Hampel, M. Nohr, B. Büchner & M. Knupfer "Comprehensive studies of the electronic structure of pristine and potassium doped chrysene investigated by electron energy-loss spectroscopy" *J. Chem. Phys.*, **137**, 114508 (2012).
- (4) B. Mahns, F. Roth, A. König, M. Grobosch, M. Knupfer & T. Hahn "Electronic properties of 1,2;8,9-dibenzopentacene thin films: a joint experimental and theoretical study" *Phys. Rev. B*, **85**, 035209 (2012).
- (5) F. Roth, A. König, B. Mahns, B. Büchner & M. Knupfer "Evidence for phase formation in potassium intercalated 1,2;8,9-dibenzopentacene" *Eur. Phys. J. B*, **85**, 242 (2012).
- (6) F. Roth, R. Schuster, A. König, M. Knupfer & H. Berger "Momentum dependence of excitons in pentacene" *J. Chem. Phys.*, **136**, 204708 (2012).
- (7) B. Mahns, F. Roth & M. Knupfer "Absence of photoemission from the Fermi level in potassium intercalated picene and coronene films: structure, polaron or correlation physics?" *J. Chem. Phys.*, **136**, 134503 (2012).
- (8) B. Mahns, F. Roth, M. Grobosch, S. Lindner, M. Knupfer, T. Saragi, T. Reichert, J. Salbeck, & T. Hahn "Electronic properties of spiro compounds for organic electronics" *J. Chem. Phys.*, **136**, 124702 (2012).
- (9) C. Kramberger, F. Roth, R. Schuster, R. Kraus, M. Knupfer, E. Einarsson, S. Maruyama, D.J. Mowbray, A. Rubio, & T. Pichler "Channeling of charge carrier plasmons in carbon nanotubes" *Phys. Rev. B*, **85**, 085424 (2012).
- (10) R. Friedrich, T. Hahn, J. Kortus, M. Fronk, F. Haidu, G. Salvan, D.R.T. Zahn, M. Schlesinger, M. Mehring, F. Roth, B. Mahns, & M. Knupfer "Electronic states and the influence of oxygen addition on the optical absorption behaviour of manganese phthalocyanine" *J. Chem. Phys.*, **136**, 064704 (2012).
- (11) F. Roth, J. Bauer, B. Mahns, B. Büchner & M. Knupfer "Electronic structure of undoped and potassium doped coronene investigated by electron energy-loss spectroscopy" *Phys. Rev. B*, **85**, 014513 (2012).

## List of publications

- (12) P. Cudazzo, M. Gatti, F. Roth, B. Mahns, M. Knupfer & A. Rubio “Plasmon dispersion in molecular solids: Picene and potassium-doped picene” *Phys. Rev. B*, **84**, 155118 (2011).
- (13) B. Mahns, F. Roth, M. Grobosch, D.R.T. Zahn & M. Knupfer “Electronic excitations of potassium intercalated manganese phthalocyanine investigated by electron energy-loss spectroscopy” *J. Chem. Phys.*, **134**, 194504 (2011).
- (14) F. Roth, B. Mahns, B. Büchner & M. Knupfer “Exciton character in picene molecular solids” *Phys. Rev. B*, **83**, 165436 (2011).
- (15) F. Roth, B. Mahns, B. Büchner & M. Knupfer “Dynamic response and electronic structure of potassium-doped picene investigated by electron energy-loss spectroscopy” *Phys. Rev. B*, **83**, 144501 (2011).
- (16) F. Roth, C. Hess, B. Büchner, U. Ammerahl, A. Revcolevschi & M. Knupfer “Plasmons and interband transitions of  $\text{Ca}_{11}\text{Sr}_3\text{Cu}_{24}\text{O}_{41}$  investigated by electron energy-loss spectroscopy” *Phys. Rev. B*, **82**, 245110 (2010).
- (17) S.-L. Drechsler, F. Roth, M. Grobosch, R. Schuster, K. Koepernik, H. Rosner, G. Behr, M. Rotter, D. Johrendt, B. Büchner & M. Knupfer “Insight into the physics of Fe-pnictides from optical and  $T = 0$  penetration depth data” *Physica C: Superconductivity*, **470**, S332 (2010).
- (18) F. Roth, M. Gatti, P. Cudazzo, M. Grobosch, B. Mahns, B. Büchner, A. Rubio & M. Knupfer “Electronic properties of molecular solids: the peculiar case of solid picene” *New J. Phys.*, **12**, 103036 (2010).
- (19) F. Roth, A. König, R. Kraus, M. Grobosch, T. Kroll & M. Knupfer “Probing the molecular orbitals of FePc near the chemical potential using electron energy-loss spectroscopy” *Eur. Phys. J. B*, **74**, 339 (2010).
- (20) A. König, F. Roth, R. Kraus & M. Knupfer “Electronic properties of potassium doped FePc from electron energy-loss spectroscopy” *J. Chem. Phys.*, **130**, 214503 (2009).
- (21) T. Kroll, F. Roth, A. Koitzsch, R. Kraus, D.R. Batchelor, J. Werner, G. Behr, B. Büchner & M. Knupfer “Absorption and photoemission spectroscopy of rare-earth oxypnictides” *New J. Phys.*, **11**, 025019 (2009).
- (22) F. Roth, A. König, R. Kraus & M. Knupfer “Potassium induced phase transition of FePc thin films” *J. Chem. Phys.*, **128**, 194711 (2008).

# List Of Talks And Posters

- 07/2012 **EXCON 2012**, "*Differences in the exciton structure and dynamics of aromatic hydrocarbon systems*", Groningen, the Netherlands, poster.
- 03/2012 **DPG spring meeting 2012**, "*Electronic structure of doped hydrocarbon superconductors*", Berlin, Germany, talk.
- 03/2012 **DPG spring meeting 2012**, "*Peculiar temperature and momentum dependence in the spin ladder systems  $Ca_xSr_{14-x}Cu_{24}O_{41}$* ", Berlin, Germany, talk.
- 11/2011 **PhD Seminar**, "*Aromatic hydrocarbon superconductors: Is a kink in the molecular structure a precondition for superconductivity?*", Holzhau, Germany, talk.
- 09/2011 **PhD Seminar IFW**, "*What is 'wrong' with the plasmon in the spin ladder cuprates? -  $Ca_xSr_{14-x}Cu_{24}O_{41}$  investigated by EELS*", Dresden, Germany, talk.
- 03/2011 **DPG spring meeting 2011**, "*Dynamic response and anomalous plasmon dispersion of potassium doped picene*", Dresden, Germany, talk.
- 03/2011 **DPG spring meeting 2011**, "*Electronic properties of molecular Picene*", Dresden, Germany, talk.
- 11/2010 **PhD Seminar**, "*Electronic properties of solid Picene*", Brunów, Poland, talk.
- 04/2010 **PhD Seminar IFW**, "*Plasmons and Interband Transitions of  $Sr_{14-x}Ca_xCu_{24}O_{41}$  investigated by Electron Energy-Loss Spectroscopy*", Dresden, Germany, talk.
- 03/2010 **DPG spring meeting 2010**, "*Plasmons and Interband Transitions of  $Sr_{14-x}Ca_xCu_{24}O_{41}$  investigated by Electron Energy-Loss Spectroscopy*", Regensburg, Germany, talk.
- 03/2010 **DPG spring meeting 2010**, "*Identification of molecular orbitals of FePc near the chemical potential*", Regensburg, Germany, poster.
- 03/2009 **DPG spring meeting 2009**, "*Absorption and photoemission spectroscopy of rare earth oxypnictides*", Dresden, Germany, talk.
- 10/2008 **Int. Workshop "Physics and Chemistry of FeAs-based Superconductors"**, 1st German-Russian workshop on Quantum Ground States, "*Absorption and photoemission spectroscopy of rare earth oxypnictides*", Dresden, Germany, poster.



# Acknowledgements

*“Keine Schuld ist dringender, als die,  
Dank zu sagen.”*

Marcus Tullius Cicero

This work would not have been possible without the help and support from numerous people. For one person the field is way too large and complicated. Sticking with the metaphor—introduced in the first chapter of this thesis—of an expedition to a “new world”, nothing would work in such a way without a perfect team, even in science. Physics is teamwork, the better the team, the better the work.

Foremost, I would like to express my sincere gratitude to Prof. Dr. B. Büchner for giving me the opportunity to do my research at the IFW as well as for his perpetual support during my whole time in Dresden.

I am indebted to my advisor Prof. Dr. Martin Knupfer for his ongoing encouragement, his ideas and suggestions (which are apparently infinite), and the patience in discussions. Especially, I thank him for his virtually always opened office and the will to answer my questions almost whenever I had one. His guidance and critical reading helped me in research and writing scientific papers, respectively. Furthermore, I would like to thank him for his continuous support during my diploma as well as PhD study and research, and for creating a relaxed and friendly working atmosphere.

Special thanks go to Prof. Dr. Angel Rubio (together with Dr. Pierluigi Cudazzo and Dr. Matteo Gatti) for the support of the calculation and answering theoretical questions arise during this work. The theoretical input helped a lot by the interpretation of the experimental spectra and enhanced the quality of the research. Additionally, I would like to thank him for the insightful discussion during our meetings in Berlin. On this also thanks to Dr. Torsten Hahn for the DFT calculation on pentacene and dibenzopentacene.

Furthermore, I would like to thank Dr. Helmuth Berger, Dr. Silke Hampel, Markus Nohr, and Alexander Schubert for the preparation of the high-quality single crystals, that were studied in this thesis and Benjamin Mahns for the thin film preparation.

Also, I want to acknowledge Dr. Roland Hübel, Stefan Leger, and Ronny Schönfelder for technical assistance and help in computational issues.

---

\*†Marcus Tullius Cicero (106 BC – 43 BC). Roman philosopher, lawyer, orator, political theorist, Roman consul and constitutionalist.

## *Acknowledgements*

---

I thank my fellow workers, members of the lunch group, and the people in the room C2E.04 for the good atmosphere and for stimulating discussions regardless of physical or non-physical origin. Special thanks go to Andreas König for constant support and useful advices concerning L<sup>A</sup>T<sub>E</sub>X and Linux and Dr. Stephan Schönecker for proofreading this thesis.

Moreover, I would like to thank the secretariat of the IFF, especially Kerstin Höllerer, Katja Schmiedel, and Manja Maluck, for their support in administrative matters and planning of trips to conferences.

Final thanks go to my family, who supported me in every situation of my life.

Last but not least, I would like to thank Eva for every single minute she spend with me, in particular the joint time in the mountains enjoying the beauty of nature apart from the 'world' of condensed matter physic.

# Eidesstattliche Erklärung

Hiermit versichere ich, daß ich die vorliegende Arbeit ohne unzulässige Hilfe Dritter und ohne Benutzung anderer als der angegebenen Hilfsmittel angefertigt habe; die aus fremden Quellen direkt oder indirekt übernommenen Gedanken sind als solche kenntlich gemacht. Die Arbeit wurde bisher weder im Inland noch im Ausland in gleicher oder ähnlicher Form einer anderen Prüfungsbehörde vorgelegt.

Die vorliegende Dissertation wurde unter der wissenschaftlichen Betreuung von Herrn Prof. Dr. B. Büchner im Institut für Festkörperphysik Forschung am Leibniz-Institut für Festkörper- und Werkstoffforschung in Dresden angefertigt.

Bis zum jetzigen Zeitpunkt habe ich keinerlei erfolglose Promotionsverfahren absolviert.

Ich erkenne die Promotionsordnung der Fakultät für Mathematik und Naturwissenschaften der Technischen Universität Dresden an.

---

Ort, Datum

---

Friedrich Roth